Triboelectric Nanogenerator Production Using Cold Spray

uOttawa

by

Mihai Stefanescu

Thesis submitted to the University of Ottawa in partial fulfillment of the requirements for the degree of

MASTER OF APPLIED SCIENCE IN MECHANICAL ENGINEERING

Faculty of Engineering – Department of Mechanical Engineering

University of Ottawa

Ottawa, Ontario, Canada

May 2026

Abstract

Triboelectric Nanogenerators (TENGs) have been proposed as a method of converting external mechanical energy into electricity. Placing these generators in a position to passively harness enough energy to power small devices could reduce the dependence on batteries and recover energy that otherwise would be lost as heat. When two dielectric materials on opposite sides of the triboelectric series come into contact, charge transfer will occur according to the triboelectric effect: Charge will move between materials to equalize the electromechanical potential, leaving the two dielectrics oppositely charged. When the two charged dielectric layers separate, their opposite surface charges create an electric field that induces a voltage between the top and bottom electrodes, which are connected through a load. If this separation and contact motion repeats periodically, the device produces a continuous alternating current signal. Production of these generators has yet to be streamlined, and there is no current standardized production method for these devices. The Cold Spray (CS) process is proposed in this study as a method of producing a simple and low cost TENG.

CS is a coating technique where solid powder particles are accelerated in a supersonic gas stream to be deposited on a substrate. Once impacting the substrate, particles undergo plastic deformation remaining entirely in their solid state and bond to the substrate. Using CS, triboelectric materials can be deposited directly on electrodes, streamlining and allowing the scaling of the manufacturing process and building a simple and low cost TENG. Aluminum, Copper and Perfluoroalkoxy Alkane polymer powders were deposited on copper substrates acting as electrodes to produce the necessary triboelectric layers. Electrical tests were then performed at varying resistances and frequencies to determine the maximum power output. The overall and theoretical maximum conversion efficiencies were then calculated. It was found that the roughness of materials deposited with the cold spray process added to the efficacy, a promising result for industrial adoption where low frequency alternating current is needed.

Acknowledgments

I would like to extend my gratitude to my thesis supervisor, Professor Bertrand Jodoin, who would regularly help and guide me throughout the duration of my studies. His patience and understanding have been invaluable to me, and it has been a privilege to be a part of a well disciplined and motivated group lead by one of the smartest people I have ever met.

I am also grateful to Professor Patrick Richer, for the clever insights he has brought to this project during our meetings and for the trust he placed in me while being his teaching assistant. His ideas and confidence in me have helped me grow both academically and professionally.

I would like to thank all the members of the Cold Spray Research Laboratory at the University of Ottawa made up of Professor Yandouzi, Aleks, Dan, Parisa, Saeed, Hamid, Krutik, Yeongmin, and Juchan. They've always been available to me for help and guidance, and I am thankful to have them all as friends.

I am grateful to the machinists and technicians at the Department of Mechanical Engineering. Thank you to Paul, Jacques, Stan, and James for regularly helping me out, and a special thanks to Leo for everything electrical related, this project would not have come to life without his wizardry.

Most importantly, I extend my heartfelt gratitude to my parents for their unconditional love and support throughout this journey. They have been a pillar in my achievements and instrumental in bringing me to where I am now.

Table of Contents

List of Figures

List of Tables

Nomenclature

CS	Cold spray
TENG	Triboelectric nanogenerator
VS-TENG	Vertical separation triboelectric nanogenerator
V_{OC}	Open circuit voltage
Q_{SC}	Short circuit charge
I_{SC}	Short circuit current
V	Voltage
Q	Charge
P	Power
E	Electric field
A	Surface area
σ	Surface charge density
C	Capacitance
ε_0	Permittivity of free space
ε_r	Dielectric constant
d	Dielectric thickness
η	Efficiency

1 INTRODUCTION

1.1 Background

In recent years, the development of sustainable, efficient, and portable energy sources has become a primary goal across scientific and engineering fields. The rapid rise in demand for autonomous, wearable, and mobile electronics has spurred researchers to explore various methods of energy harvesting from ambient sources, such as solar, thermal, and mechanical energy [1]. Among these, mechanical energy harvesting is especially appealing due to the vast availability of kinetic energy from human motion, environmental vibrations, and natural mechanical processes. To capture this untapped potential, triboelectric nanogenerators (TENGs) have emerged as a revolutionary technology, providing a versatile and eco-friendly method of converting mechanical energy into electrical energy [2], [3].

TENGs operate based on the triboelectric effect, where charge separation occurs between two materials with differing affinities for electrons. When the materials come into contact in a TENG, electrons transfer between their surfaces based on their positions in the triboelectric series, leaving one surface positively charged and the other negatively charged. When the materials separate, this fixed charge imbalance creates an electric field that drives electrons through the external circuit, producing a current. The performance of TENGs can be optimized by selecting appropriate material combinations and design architectures, making them suitable for a range of applications, from wearable electronics to environmental monitoring [4].

Cold spray (CS) is a solid-state deposition process that has garnered significant attention in material science and manufacturing due to its unique advantages over conventional thermal spraying [5]. In CS, particles are accelerated through a supersonic flow and adhere to a substrate upon impact without reaching melting temperatures, thereby preserving the intrinsic properties of the feedstock materials [6]. This method has found applications in fields that require high-quality coatings, such as in aerospace [7], biomedical devices [8], and in repair and service technologies [7], [9].

The integration of CS with triboelectric nanogenerators is an innovative approach that leverages the mechanical properties and adhesion strength provided by the CS process, potentially enhancing the durability and longevity of TENGs. By enabling a low-temperature deposition of triboelectric materials, CS allows for the preservation of polymeric and metallic properties that would otherwise degrade under high temperature processes, expanding the range of materials that can be incorporated into TENGs.

The performance of a TENG is highly dependent on the selection of triboelectric pairs [4] [11], where one material acts as a tribopositive (electron donating) surface and the other as a tribonegative (electron withdrawing) surface. In this study, polytetrafluoroethylene (PFA) is used as the tribonegative material, known for its high electron affinity [12], [13] and stability, while aluminum is chosen as the tribopositive material due to its favorable mechanical properties, conductivity, and relative ease of deposition by CS [14]. Copper (Cu) is used as the substrate and subsequent electrode material, as it is a common electrical conductor and has served as a durable substrate in CS. Cu overall provides the conductivity and mechanical integrity to support a TENG's operation.

This selection of materials should form a durable and efficient system, allowing the TENG to achieve high performance under a range of mechanical stresses and frequencies. By using a CS method to deposit PFA and aluminum onto copper substrates, the triboelectric layers are expected to exhibit enhanced density, adhesion and mechanical robustness. As CS has not been used as the primary manufacturing process to construct TENGs, an investigation into the electrical performance will be a primary novelty.

The vertical contact-separation triboelectric nanogenerator (VS-TENG) is one of the most studied TENG designs due to its simple architecture and efficient energy harvesting capabilities [4], [15]. In this configuration, the triboelectric materials are positioned so that periodic contact and separation generate electrical output as charges transfer between the surfaces. This configuration is particularly suitable for wearable and environmental sensors [16], where contact-separation motion is readily available, and consistent energy output is required.

For this study, the vertical contact-separation TENG design is chosen due to its mechanical simplicity [15] and proven efficiency in energy conversion. The selection of materials and

the CS deposition process are expected to enhance the TENG's overall performance, providing a potentially scalable and sustainable solution for energy harvesting applications.

1.2 Research Objectives

This work aims to explore the performance of a VS-TENG constructed using the CS process, with a specific focus on the deposition of PFA and Al on Cu substrates. The objectives of this research are to:

1. **Design and Fabrication:** Develop a functional vertical contact-separation TENG using Cold Spray to deposit PFA as the tribonegative material and aluminum or copper as the tribopositive/bonding layers on a copper substrate.
2. **Characterization of Triboelectric Performance**: Quantify the electrical output of the TENG, including open-circuit voltage, short-circuit current, transferred charge, and power, under controlled mechanical contact-separation cycles.
3. **Durability and Material Analysis:** Evaluate the mechanical stability and coating-substrate adhesion of the TENG over repeated cycles and investigate the effects of microstructural features such as cracks and coating integrity on electrical performance.
4. **Efficiency and Theoretical Modeling:** Understand the theoretical model for the vertical contact-separation TENG that describes the electric field evolution during separation, quantify energy conversion efficiency, and analyze each step of the TENG cycle as part of a thermodynamic framework.

1.3 Thesis Outline

The thesis is organized into seven chapters. Chapter 1 consists of an introduction to the research along with a brief overview of the research objectives.

Chapter 2 provides a literature review of TENGs, focusing on developing a foundation by introducing the triboelectric series, the different design configurations along with their uses, advantages and potential drawbacks, material choices, and current fabrication methods with CS being proposed as an alternative. As CS is an incremental development of existing thermal spraying methods, CS along with other thermal spraying methods are also briefly discussed.

Chapter 3 expands the theoretical background to quantify the operation of the VS-TENG through a simple mathematical model along with the typical VS-TENG cycle and efficiencies.

Chapter 4 defines the research objectives of this work, along with the methodology used for each step.

Chapter 5 outlines the experimental setup and methodology used in the CS deposition and coating characterization process, along with the equipment used in the electrical testing and characterization.

Chapter 6 presents the results and discussion of the TENG's performance, including the impact of material properties and deposition techniques.

Finally, Chapter 7 concludes with a summary of findings and recommendations for future work.

2 LITERATURE REVIEW

2.1 The Triboelectric Effect

The triboelectric effect is a fundamental physical phenomenon where certain materials become electrically charged after they come into contact and are subsequently separated [17]. This effect, one of the oldest known to humanity, is necessary to understanding the operation of TENGs, as their ability to convert mechanical energy into electrical energy is governed by this phenomenon. With growing interest in sustainable and self-powered devices, the triboelectric effect has led to applications in energy harvesting and sensing. Understanding this effect's mechanisms and influencing factors is essential for optimizing TENGs and similar technologies.

2.1.1 Origins and Discovery

Historically, the triboelectric effect was first documented by the ancient Greeks [18], who observed that rubbing amber, which is an electron withdrawing material, with fur caused it to attract small objects. The word “triboelectric” itself originates from the Greek word “Tribos” meaning “to rub”. However, only in recent centuries has the effect been studied more systematically. In the 20th century, advancements in material science and physics facilitated a deeper understanding, revealing that contact and separation create a charge imbalance due to material-specific electron affinities. This discovery paved the way for the development of the triboelectric series, which ranks materials according to their tendency to gain or lose electrons.

2.1.2 Mechanisms

While widely observed, the exact mechanism of the triboelectric effect remains a subject of scientific investigation. The dominant theory suggests that contact between materials leads to electron transfer based on differences in electron affinity [17], [19], which creates a potential difference upon separation [20]. This electron-transfer theory claims that materials with higher electron affinities tend to gain electrons, becoming negatively charged, while materials with lower electron affinities lose electrons, becoming positively charged [17], [19], [20]. The most common example is a balloon rubbing on human hair. Human hair has a tendency to lose electrons to the balloon [21]. As a result, the balloon

now gains electrons and an electric field is produced between the hair and the balloon, which is why the hair stands. This is illustrated below in Figure 1.

Figure 1: Hair rising towards a balloon [22]

Alternative theories propose that ions or material particles may transfer during contact, impacting the charge distribution [23], but this is a novel theory and does not have experimental evidence. Some research also indicates that surface characteristics, such as roughness [4], [24], elasticity [25], [26], and hardness [27], can affect the mechanism by creating additional localized points for charge transfer. Despite the dominant electron-transfer hypothesis, these alternative explanations outline the complexity of the triboelectric effect and the need for further research into its mechanisms. As the triboelectric effect is currently best described by the transfer of electrons [4], [17], [19] it will be used as the main description of the phenomenon and subsequent equations of state.

Several material and environmental factors significantly impact the strength and consistency of the triboelectric effect. These include the material composition, surface roughness, environmental conditions, and contact force and separation speed [24], [25], [26], [28], [29].

Materials with higher affinities for electrons are more effective because they tend to attract and hold electrons when in contact with other materials. When paired with materials that readily lose electrons, this difference in electron affinity creates a larger surface charge during contact and separation, resulting in a higher potential difference. [31]. This is why

polymers like Teflon or polyvinyl chloride (PVC), respectively containing fluorine and chlorine [32], highly electronegative halogens known for their strong electron affinity [33], [34] tend to become highly negatively charged.

The surface finish of a material affects the contact area between materials and the amount of charge generated. Rougher surfaces can increase the likelihood of charge retention by creating microscale points of contact, whereas smoother surfaces tend to yield a more uniform charge distribution [35]. Surfaces with artificial indentations or engineered microstructures can further enhance the effective contact area and charge trapping. Other effects such as humidity, temperature and air pressure can influence charge retention and transfer [36]. For example, humidity reduces the effectiveness of the triboelectric effect by increasing conductivity on surfaces, which dissipates charge [36], [37], [38]. Lower humidity environments often favor stronger triboelectric interactions.

Both the force applied during contact and the speed of separation influence the amount of charge generated. Stronger contact forces create larger contact areas, and faster separation speeds can enhance the triboelectric effect by rapidly disrupting the electrical equilibrium and creating higher rates of charge transfer, increasing current [39].

2.2 The Triboelectric Series

The triboelectric series organizes materials based on their tendency to either gain or lose electrons, providing a predictive framework for which materials become positive or negative upon contact. As previously stated, Triboelectricity has been observed since ancient times, but it is only in recent decades, with advancements in nanotechnology and material science, that it has found applications in fields such as energy harvesting, sensing, and advanced material design.

The triboelectric series classifies materials based on their electron affinity [17], [19], [41]. When two materials contact and then separate, one material often tends to gain electrons becoming negatively charged, while the other loses electrons becoming positively charged. The triboelectric series which was first published by Johan Carl Wilcke in 1757 and lists materials in order of the polarity of charge separation when they are touched or slide against another. A material towards the bottom of the series, when touched to a material near the

top of the series, will acquire electrons, thus gain a negative charge. These materials are known as withdrawers or tribonegative materials. Inversely, a material towards the top of the series will lose electrons and acquire a positive charge, being referred to as donors or tribopositive materials. The modern list expands this work to consist of materials like PTFE [42] and PFA known for their electron-accepting properties [43], appearing toward the negative end, while materials like polyurethane [44] and nylon [43], [45], [46] are known for their electron-donating properties, appear on the positive side. This order provides insights into designing material pairings for specific triboelectric effects, such as those used in triboelectric nanogenerators (TENGs) for energy harvesting. An example series is shown below in Figure 2**.**

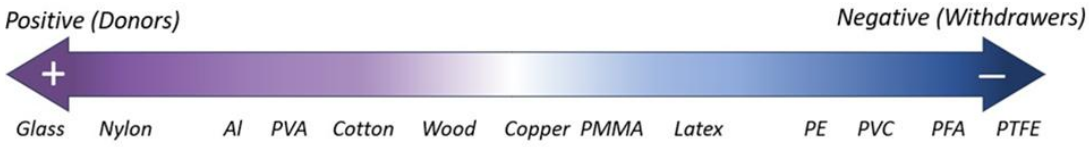

Figure 2: An Example Triboelectric Series

In practical terms, triboelectric interactions are influenced by several factors beyond the properties of the materials, including surface roughness and physical characteristics like hardness and elasticity. The complexity of these influences presents challenges in the universal application of the triboelectric series, as material rankings can vary based on these variables [47]. However, it remains a foundational tool for predicting charge transfer tendencies and guiding material selection.

One of the most promising applications of the triboelectric series is in energy harvesting, particularly through the design, construction, and operation of TENGs [48]. TENGs are a direct application of the triboelectric effect as the materials selected are from opposite ends of the triboelectric series. With the growing need for sustainable energy sources, TENGs have been investigated for powering wearable devices [49], [50] environmental sensors [51], [52], and small electronics [53], among other applications. The triboelectric series guides the choice of materials for maximizing energy output, where materials with a greater difference in electron affinity tend to generate higher voltages.

Additionally, the triboelectric series has driven innovations in self-powered sensors and touch-sensitive surfaces. TENGs have been adapted to create touch interfaces [54], [55], [56], where changes in electric potential provide positional feedback, enabling various applications in robotics and touchscreen interfaces. This adaptability is facilitated by selecting materials that provide optimal triboelectric performance under specific environmental and operational conditions.

While the triboelectric series is useful in designing TENGs and other devices, several challenges limit its effectiveness as a universal tool. The first challenge is the variability in triboelectric rankings, where factors like humidity, temperature, and surface contamination can alter a material's triboelectric properties. Additionally, the triboelectric effect is largely empirical, lacking a comprehensive theoretical model that accounts for all contributing factors, limiting predictive accuracy. One attempt at referencing materials on their ability to donate or withdraw with respect to Mercury [57] was made but has not been adopted or standardized outside of their study. Their triboelectric series is shown below in Figure 3.

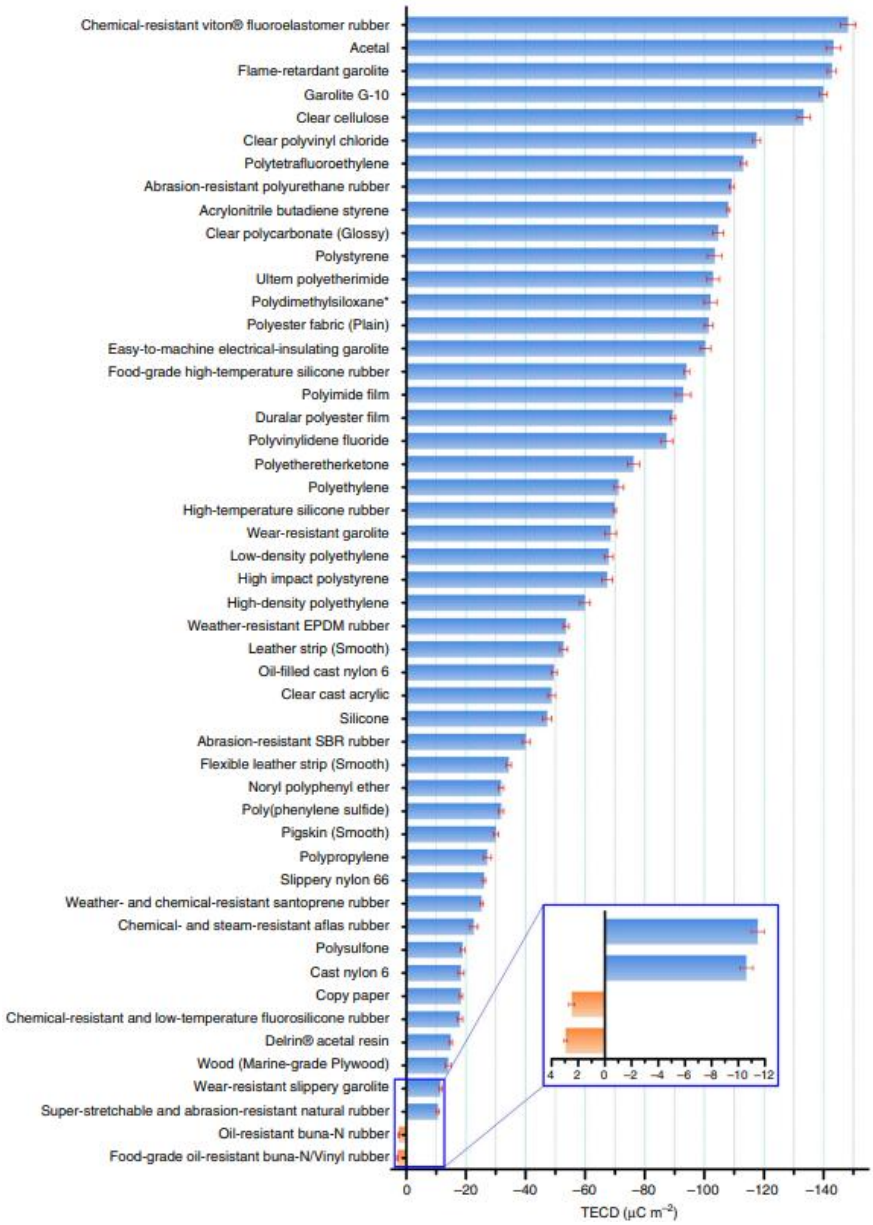

Figure 3: Quantified Triboelectric Series with Mercury as the Reference Material [57]

Further, the limitations of the triboelectric series become apparent when materials with close electron affinities are paired. In such cases, the resulting charge difference may be insufficient for any effective applications. An example is the pairing of wood and copper, which has effectively zero charge interaction, thus no practical purpose. These limitations indicate a need for standardized conditions in triboelectric testing and more advanced theoretical models to improve the consistency and reliability of the triboelectric series.

The triboelectric series provides a foundational and fundamental understanding of material behavior in triboelectric applications, particularly for emerging technologies in energy harvesting and sensing. While its empirical nature introduces variability and guesswork, recent advancements in material science and nanotechnology are gradually addressing these challenges, allowing for more predictable and efficient use of the triboelectric effect. Future research into the mechanisms of charge transfer, as well as standardized testing protocols, will likely enhance the triboelectric series' applicability across an even broader range of materials and environmental conditions. With these improvements, the triboelectric series can potentially support innovations in self-powered devices and sustainable energy solutions.

2.3 Triboelectric Nanogenerators

In today's world, electronics are mainly used to enhance the quality of life in aspects of health, safety, communications, and transportation. An abundant source of energy which is relatively untapped is the mechanical energy resulting from vibrations and oscillations from the ambient [1]. These can include the oscillations of transportation infrastructure such as roads and bridges [58] but also the vibrations from repetitive motions of the human body [49], [59] such as running and jumping. The triboelectric nanogenerator (TENG) was first demonstrated in 2012 by Dr. Zhong Lin Wang and his research group at the Georgia Institute of Technology, forming the foundation for subsequent developments in this technology. [60]. The first TENG produced an output power density of 10.4 mW/cm^3 and periodic voltage readings of 3.3 V. Further development of TENGs since the first breakthrough led to the development of four modes; vertical contact separation, lateral sliding, single electrode, and contact free standing, all of which will be described in the sections below.

2.3.1 Vertical Contact Separation

The vertical contact-separation triboelectric nanogenerator (VS-TENG) is the mode which is most widely explored in TENG design because of its simplicity [17], reliability [62], and compatibility with natural mechanical oscillations [4], [63], [64]. In this mode, two triboelectric materials are typically attached to opposing substrates. They come into contact under an applied force, leading to charge transfer via contact electrification. Upon

separation, an electric potential forms due to the spatial separation of the oppositely charged surfaces. This potential drives a current through an external circuit as the system seeks to balance the electromechanical potential, which generates charge transfer and electrical power. A cycle example is shown below in Figure 4.

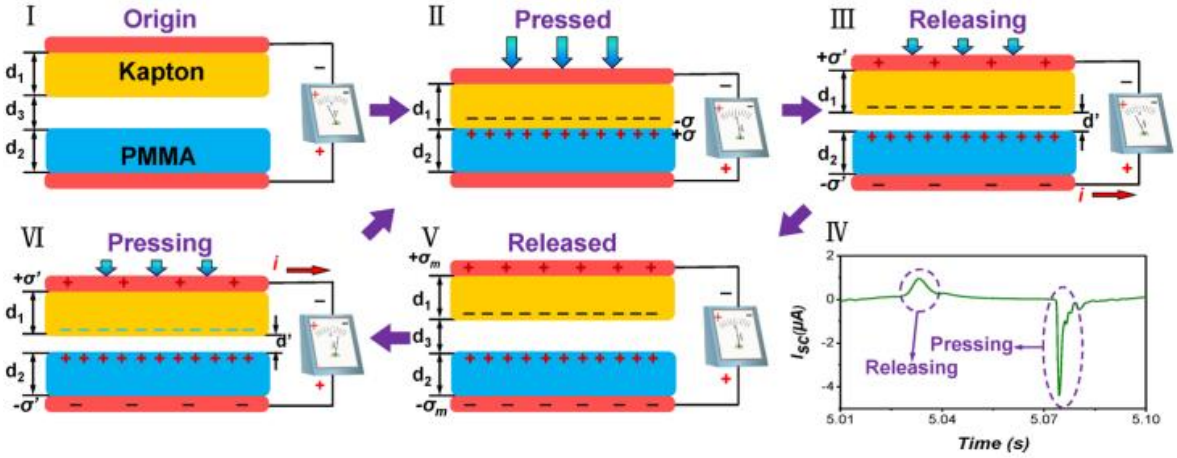

Figure 4: Typical VS-TENG Operation [4]

What makes this mode particularly attractive is its effectiveness in harvesting energy from naturally occurring vertical vibrations such as acoustic waves or machine-induced oscillations. These can come from the contact of a shoe [65] and the sidewalk [66], the vertical oscillations of transportation infrastructure such as roads, bridges, and railroads [67], [68] and the oscillations found in vehicles and machines [69], [70]. Its straightforward vertical displacement mechanism is well-suited to low-frequency motions, and the output performance can be optimized by tuning contact force, surface area, and separation distance [4].

A key advantage of this mode is the minimal lateral movement between layers, which means there is little wear and has the potential for a long operational life. Although it is relatively easy to fabricate and integrate into layered or stacked devices, no standardized manufacturing process exists for TENGs. Repeated contact and separation can still introduce material fatigue over time, particularly if brittle materials are used without cushioning. Evidently, voltage and current production is dampened unless the oscillation is continuous.

Because of its efficiency, structural simplicity, and compatibility with a broad range of mechanical inputs, the vertical contact-separation mode remains a foundational design in both research and practical energy-harvesting applications. It also provides a clear framework for modeling and optimization, often serving as the baseline configuration for theoretical analysis of TENG output mechanisms. A broader understanding of this operating mechanism and theoretical background will be presented in chapter 3.

2.3.2 Lateral Sliding

The lateral sliding mode of operation for TENGs utilize an in-plane shearing motion between two triboelectric layers to induce periodic charge redistribution. In this configuration, the two surfaces are each composed of materials with opposite triboelectric properties which remain in continuous contact while one is mechanically displaced relative to the other in the lateral direction. As sliding occurs, surface-bound charges are spatially separated along the interface, generating an electric potential between the corresponding electrodes. This results in an alternating current in the external circuit as the relative position between the charged regions changes [4], [71], [72]. The schematic showing the operation is shown in Figure 5.

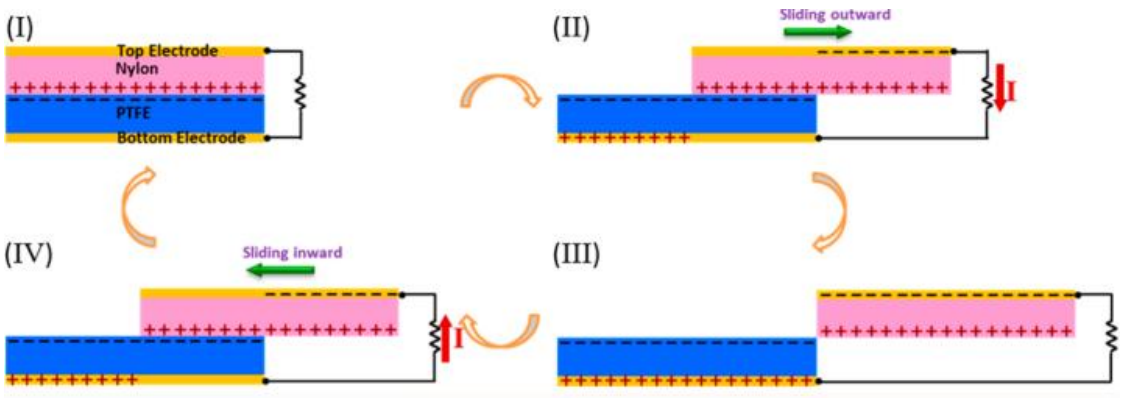

Figure 5: Operation of a TENG in Lateral Sliding [72]

However, the lateral sliding mode also presents challenges, particularly in terms of mechanical durability [72], [73]. The sustained friction between surfaces can lead to material degradation over time, diminishing performance and reducing the device's operational lifetime [74]. Strategies such as surface patterning, lubrication, and the use of

robust polymer layers have been explored to mitigate this wear and maintain high output over repeated cycles [75, [76].

Despite these limitations, the lateral sliding mode remains a valuable configuration, especially for applications involving rotational or linear reciprocating motion, such as gear systems, sliding mechanisms, or moving interfaces in machinery [74], [77]. It has also been used in self-powered interfaces where horizontal motion is naturally present.

2.3.3 Single Electrode

The single-electrode mode offers a simplified triboelectric nanogenerator configuration by requiring only one triboelectric layer to be physically connected to the external circuit. The second triboelectric surface is often an object from the environment or a moving part of the body, which is free-standing and typically referenced to ground. As the free surface encounters or moves relative to the fixed triboelectric layer, charge transfer occurs via contact electrification, as is with the vertical contact separation method. The resulting electrostatic imbalance induces a current in the circuit as the system seeks to re-establish equilibrium [4], [78], [79]. The schematic visualizing this process is shown below in Figure 6.

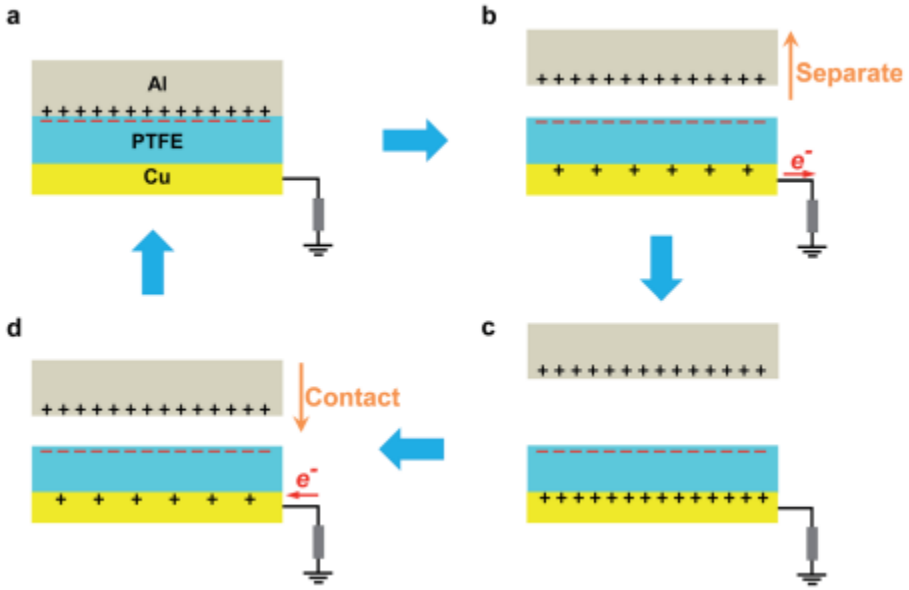

Figure 6: Operation of a Single Electrode TENG [78]

This configuration eliminates a second electrode by having the circuit grounded, making it highly suitable for applications involving irregular or user-driven motion such as human finger motion since human skin is an excellent electron donor. The single-electrode mode has been used primarily wearable devices, touch sensors, and human-machine interfaces [79], where its structural simplicity and adaptability to ambient motion offer significant design flexibility.

However, the mode is inherently limited by its dependence on a global ground reference [4], which can limit output performance and introduce variability depending on the local electrical environment. Since the potential difference is developed between the active electrode and ground rather than between two closely coupled surfaces, the electric field strength and the output current is usually lower than in traditional configurations [79]. To address these challenges, researchers have investigated improvements such as using high-dielectric substrates, optimizing electrode geometry, or incorporating charge amplification mechanisms. Despite its lower output, the single-electrode mode remains a compelling option for energy harvesting in low-power, portable, or user-interactive systems, where mechanical simplicity and integration flexibility take precedence over peak electrical performance.

2.3.4 Contact Free Standing

The freestanding triboelectric-layer mode represents a unique configuration in TENGs, where the triboelectric layer is not fixed in place but instead moves freely relative to the electrodes. In this setup, a single charged triboelectric material, often a polymer film, is positioned to pass over stationary electrodes, generating a potential difference as it induces charge transfer through electrostatic induction. Unlike the contact-separation or sliding modes, where direct mechanical contact is integral to the charge generation, the freestanding mode relies on the relative motion of the triboelectric material and the electrodes to induce current flow in the external circuit [82], [83], [84]. A schematic of the contact free standing mode is shown in Figure 7.

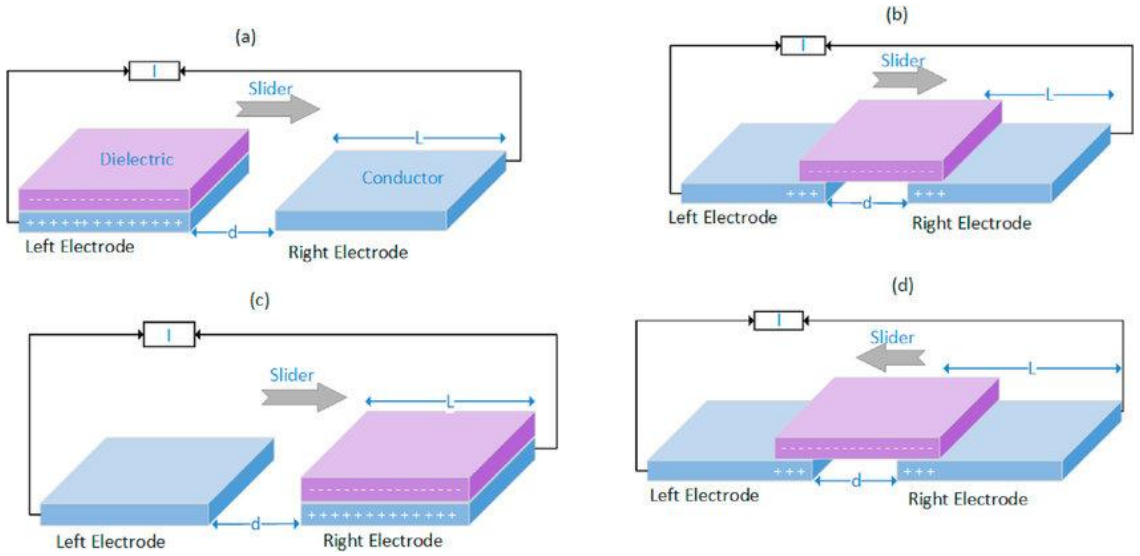

Figure 7: Operation of a Contact Free Standing TENG [84]

However, the freestanding mode also introduces certain limitations, primarily related to the control and optimization of the distance between the moving triboelectric layer and the electrodes [84]. The efficiency of charge generation depends heavily on the relative speed and distance of the moving layer. The motion must be carefully managed to ensure the triboelectric material stays within the effective range of the electrodes, which can complicate design and integration into an environmental system [85].

Despite these challenges, the freestanding triboelectric-layer mode offers significant potential for energy harvesting in dynamic environments. It has been seen used in self-powered sensors, wearable electronics, and systems requiring rotational or oscillatory motion. The ability to decouple the triboelectric layer from the electrodes also allows for greater design flexibility, enabling the development of more robust and durable energy-harvesting devices [85].

2.4 Material Selection in Triboelectric Nanogenerators

2.4.1 Fluoropolymers

Triboelectric nanogenerators (TENGs) rely heavily on the selection of materials with appropriate surface charge affinity to optimize electrical output [11], [86]. Among these, fluoropolymers have emerged as some of the most effective tribonegative materials due to their strong electron-withdrawing capabilities and dielectric properties [87].

Fluoropolymers such as polytetrafluoroethylene (PTFE) [88], [89], polyvinylidene fluoride (PVDF) [90], [91], and perfluoroalkoxy alkane (PFA) [92], [93] consistently rank at the extreme negative end of the triboelectric series, making them ideal for maximizing charge separation in TENGs [4], [87, [88]. PTFE has been widely used due to its high electronegativity, low surface energy, and excellent mechanical properties. PTFE-based TENGs can achieve high surface charge densities exceeding 250 $\mu C/m^2$ under contact-separation operation modes [89]. Copolymers have shown promise in hybrid energy-harvesting applications due to their ability to generate both triboelectric and piezoelectric outputs.

The method by which fluoropolymers are deposited or applied to TENG surfaces significantly affects performance. Electrospinning [94], spin coating [95], soft lithography [96] are the current methods of manufacture, and more recently, etching methods have been used extensively as primary methods of manufacturing. CS also allows for the deposition of polymeric films without thermal degradation, preserving the material's triboelectric performance.

The surface morphology of fluoropolymer layers plays a key role in enhancing the TENG output. Nanostructuring or micro-patterning the surface increases the effective contact area, thereby amplifying charge generation [97]. For instance, PTFE films with etched nanostructures exhibited over twice the output of smooth PTFE films under identical conditions [98]. Additionally, the inherent hydrophobicity of fluoropolymers contributes to environmental stability, particularly in humid conditions [36]. One of the most critical advantages of fluoropolymers in TENGs is their long-term durability. Their resistance to UV radiation, oxidation, and solvents allows TENGs to operate reliably in a variety of environmental conditions.

Current research is moving toward composite fluoropolymer materials, [99], [100] which are excellent for TENGs because they combine the high electron-withdrawing capability of fluorinated polymers with mechanical and dielectric properties through composite reinforcement. Their low surface energy and strong electronegativity maximize tribonegative charge generation, while the composite phase can improve durability, flexibility, and charge retention [99]. Carbon nanotubes have also been explored to improve

TENG performance by increasing the dielectric constant of a polymer matrix. When added in small amounts, they create strong local electric fields that allows a material to store more charge during contact–separation. This higher dielectric constant directly boosts the transferred charge and thus increases the potential difference between materials upon separation. Moreover, eco-friendly and recyclable fluoropolymer alternatives are being explored to address environmental concerns associated with the long-term use of fluorinated compounds.

2.4.2 Aluminum

Aluminum is commonly employed as a tribopositive material in TENGs because of its strong tendency to donate electrons upon contact with more electronegative materials. Positioned high on the triboelectric series, aluminum becomes positively charged when paired with materials such as fluorinated polymers, which readily accept electrons during contact-separation cycles.

In vertical contact-separation mode TENGs, aluminum has been used as the tribopositive material [101] and are often used as the triboelectric surface itself or as an electrode because of its high electrical conductivity. This high conductivity interestingly supports charge redistribution during the separation phase for a VS-TENG, which enhances potential difference generated by the triboelectric effect.

Aluminum's surface morphology from manufacturing techniques has been shown to significantly influence triboelectric performance. Surface roughness, whether introduced mechanically or as a byproduct of deposition techniques, can enhance local contact intimacy, thereby increasing the surface charge density after separation. This makes aluminum particularly effective in designs where maximizing contact area and triboelectric charge density is desired [102].

It has also been successfully implemented onto TENGs using various fabrication methods, including thermal evaporation and sputtering techniques. These methods allow for precise control over thickness and microstructure, both of which play critical roles in device performance and mechanical durability, which has often been overlooked when developing TENGs but is necessary to discuss for long term viability. Initial TENGs constructed from

2012 to 2014 used aluminum foil as part of a proof of concept and it is still used today for its demonstrative ability [103].

2.4.3 Nylon

Nylon has been widely studied as a tribopositive material in triboelectric nanogenerators due to its favorable electron-donating characteristics and widespread availability [104]. It ranks relatively high in the triboelectric series and exhibits consistent charge transfer behavior when brought into contact with strongly electronegative materials such as PTFE [105], [106], FEP, or PFA.

The triboelectric performance of nylon is attributed to the presence of amide groups in its molecular structure, which contribute to a high density of localized electron-donating sites. When nylon is pressed against a tribonegative material, it tends to lose electrons during contact, becoming positively charged upon separation. This surface charge persists and contributes to the electrostatic potential that drives current through an external load during the TENG's separation phase [107].

In addition to its triboelectric properties, nylon exhibits good mechanical flexibility and resilience [107], making it suitable for use in flexible and wearable TENG applications. Its surface can be further modified through techniques such as plasma treatment or micro/nanostructuring [108] to enhance contact efficiency and increase surface charge density. Several studies have shown that surface roughness plays a significant role in the triboelectric output of nylon-based TENGs, with increased roughness generally correlating with improved performance due to enhanced real contact area.

2.5 Thermal Spraying

Coatings have demonstrated to have a wide array of different applications. These include acting as thermal barriers in turbine blades to increase overall operating temperatures, protection against corrosion and erosion for applications in harsh environments and have been used to improve wear resistance. There have also been several repair techniques where the constructed coatings played an instrumental role, such as in restoring the roundness of wheels used in railroad rolling stock. Coating depositions require several careful considerations to obtain the desired thickness, composition, and roughness, but their direct deposition onto a substrate is what makes them appealing in the application of designing

and manufacturing of TENGs. Thermal spraying is a class of different coating deposition methods which all involve accelerated particles towards a substrate [109]. Different processes exist which either raise particle energy by utilizing a high temperature or high velocity gas stream propelling the feedstock towards a substrate [110]. A coating is built when the particles impact and bond to the surface. The categories of thermal spraying are split into four main groups: plasma, electric arc, kinetic, and combustion. Figure 8 below shows the family of thermal spraying as a function of gas temperature and velocity.

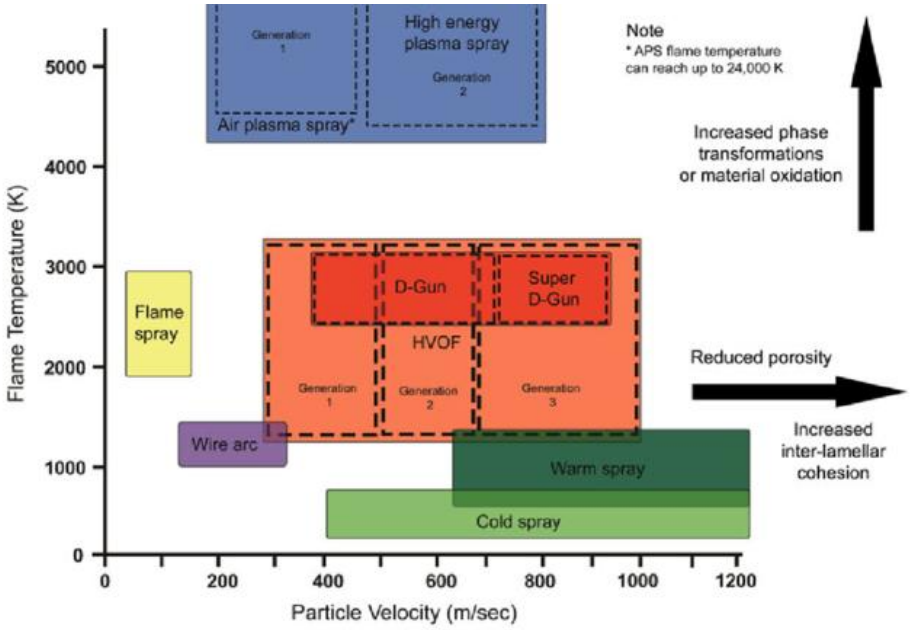

Figure 8: Gas temperature and velocity for different thermal spray processes [110]

2.5.1 Flame Spray

Flame spray is a thermal spray process in which a powder or wire feedstock is introduced into an oxy-fuel combustion flame using a torch, where it is melted or softened and then propelled toward a substrate by the expanding combustion gases. Particle velocities are relatively low (<100 m/s), and the flame environment is oxidative. The process is valued for its simplicity and cost-effectiveness but can be limited by poor control over oxidation and porosity. Aluminum, due to its low melting point and good thermal conductivity, is a common material for flame spray, though the oxidative environment promotes the formation of aluminum oxides [111]. These types of defects can significantly reduce the electrical and mechanical performance of the coating. However, flame-sprayed aluminum

remains viable for anti-corrosion applications and thermal barriers, particularly when post processing treatments such as remelting is used to further enhance the coating quality. A schematic illustrating the flame spray process is shown in Figure 9.

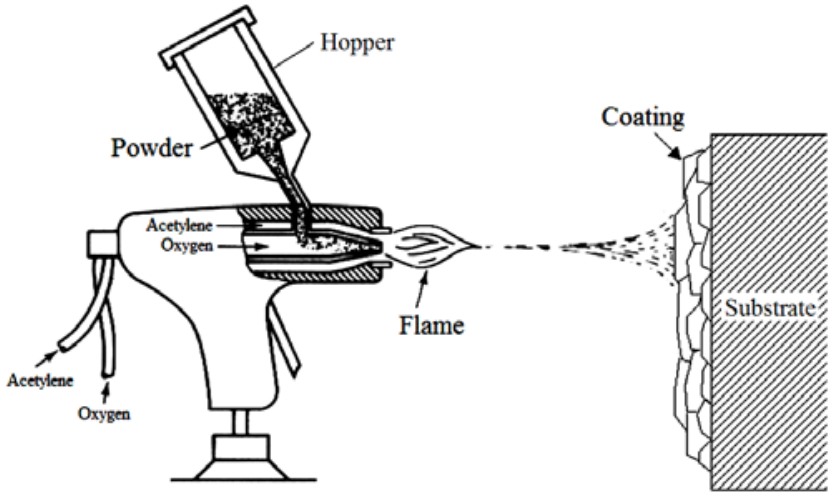

Figure 9: Flame Spray equipment showing the Hopper, Flame, and Coating [111]

Nylon and PFA, both thermoplastics, require even more precise thermal control. Nylon melts around 220 °C and can be sprayed successfully using FS [112], producing flexible and low-friction coatings often used for wear resistance or insulation on industrial components. PFA, with a higher melting point of around 305 °C and decomposition threshold near 400 °C, has a narrow processing window and poor wetting behavior due to its low surface energy. While flame spraying of PFA is challenging, it has been demonstrated with specialized nozzles or as part of composite feedstocks and on its own. In both cases, adhesion is mainly from mechanical interlocking, and the resulting coatings are often porous and rough. Flame spray is not typically the preferred method for high-performance applications involving these polymers, especially where triboelectric activity or maintenance of electrical properties is critical.

2.5.2 Plasma Spray

Plasma spraying uses a high-temperature, non-combustive plasma jet which is generated by ionizing an inert gas such as Argon to melt and accelerate feedstock particles toward a substrate. With flame temperatures exceeding 10,000 °C and particle velocities typically in the 150–300 m/s range, plasma spray provides better thermal and kinetic energy compared to combustion-based methods. While typically used to deposit ceramic feedstock onto

metal substrates, aluminum can be processed effectively using plasma spray [113]. Plasma-sprayed aluminum can achieve better cohesion and density than flame-sprayed coatings [114] and is used in thermal barriers, conductive layers, and corrosion protection mainly with ceramics. For Nylon and PFA, plasma spray is not a valid option as these two materials are both temperature sensitive and would degrade in the extreme temperature environment. A schematic of plasma spraying is shown in Figure 10.

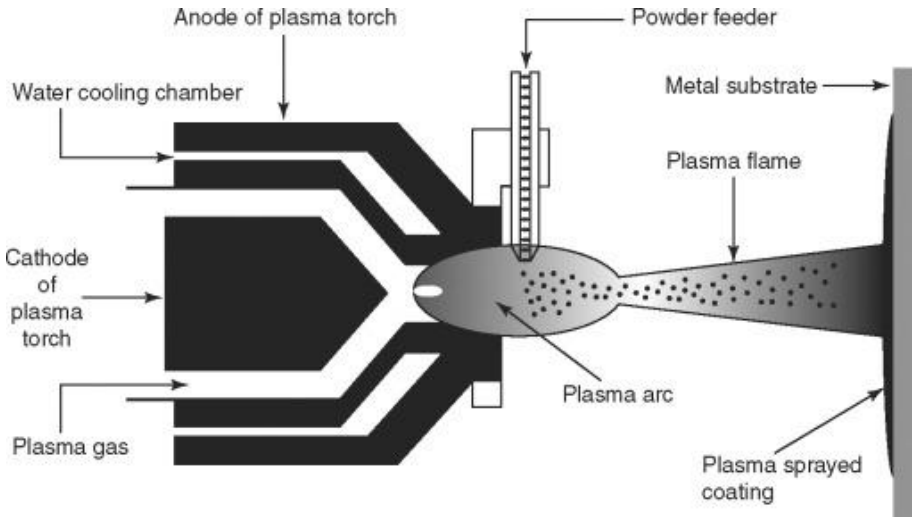

Figure 10: Plasma spray schematic [114]

2.5.3 High Velocity Oxygen Fuel Spray

High Velocity Oxygen Fuel (HVOF) process involves the combustion of oxygen and fuel (typically propane, kerosene, or hydrogen) in a high-pressure chamber to generate a supersonic jet. This jet accelerates molten or semi-molten particles toward the substrate at velocities up to 1000 m/s using a deLaval nozzle, enabling dense, well-adhered coatings with low porosity. HVOF is especially well-suited to metals and cermets. Aluminum, while meltable by HVOF, poses challenges due to its low melting point and tendency to oxidize in the combustion-rich environment. Nevertheless, HVOF has been used to deposit aluminum and aluminum-based alloys for corrosion protection and structural reinforcement, particularly when oxidation is minimized using optimized fuel ratios or controlled atmosphere variants. Thermoplastics like Nylon and PFA are unsuitable for HVOF due to their low decomposition temperatures and inability to withstand the high thermal flux of the process [114]. The intense flame temperatures in the range of 2000 °C - 3500 °C far exceed the thermal limits of these materials, leading to degradation or

complete breakdown before deposition. A schematic illustrating HVOF is shown below in Figure 11.

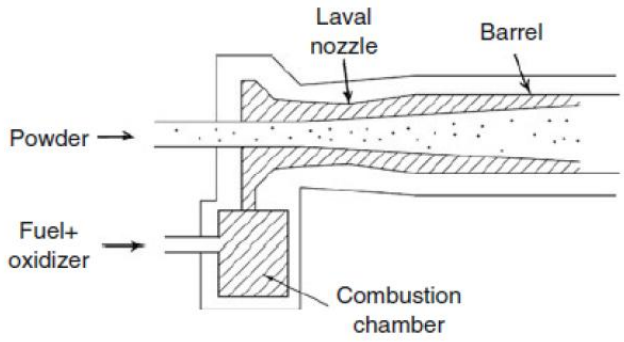

Figure 11:Injection system of an HVOF gun [115]

2.5.4 Cold Spray

Cold spray, simply referred to as CS, is an entirely solid-state deposition process where particles are accelerated to high velocities ranging from 300–1200 m/s using a pressurized gas such as nitrogen or helium and a converging-diverging de Laval nozzle [7], [9]. Unlike thermal spray techniques, CS does not rely on melting the feedstock. Instead, particles plastically deform upon high-speed impact with the substrate, creating a coating. The solid-state deposition prevents the microstructure of the particles from being altered and preserves the material mechanical properties. Aluminum is one of the most widely studied and successfully deposited materials using CS [14], [116], due to its high ductility, low yield strength, and ability to form strong metallurgical bonds upon impact. CS aluminum coatings exhibit excellent electrical conductivity, low porosity, and good adhesion. An illustration of the CS process is shown below in Figure 12.

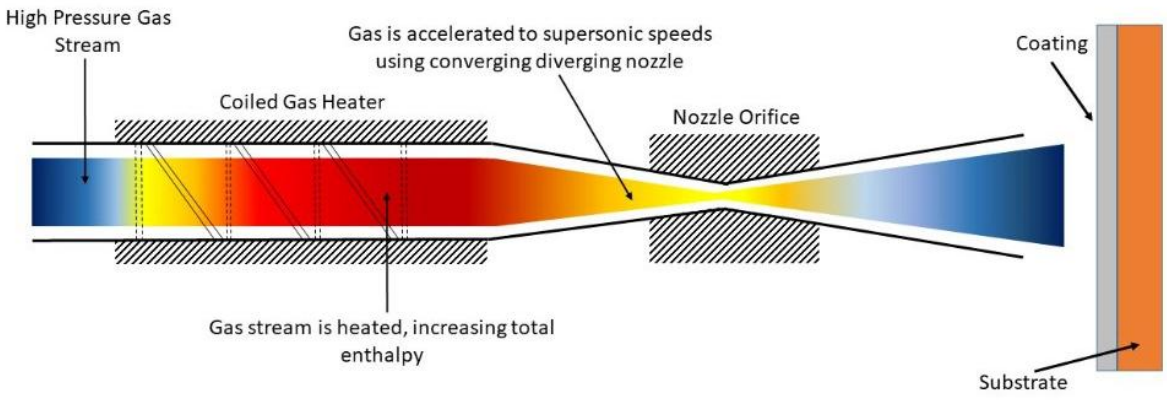

Figure 12: CS Schematic

Nylon and PFA, while not ductile metals, have been investigated for CS due to the solid-state nature of the process, which offers a route to depositing thermally sensitive materials with limiting the chances of degradation. However, polymers do not typically exhibit the same adiabatic shear instability as metals and tend to absorb impact energy elastically rather than plastically deforming [117], [118]. Particles accelerated to supersonic speeds bounce off the substrates rather than deforming and adhering to the substrates. This makes pure polymer bonding via CS more challenging. PFA, with its high molecular weight and low surface energy, is especially difficult to bond through impact alone. Even so, there has been success in depositing PFA powders by optimising the pressure, temperature, and substrate preparation. A straight section nozzle has also shown better deposition. While still a developing area, cold spray offers a promising avenue for applying nylon and PFA in triboelectric applications where the preservation of intrinsic material properties is critical.

2.6 Applications of Triboelectric Nanogenerators

TENGs have gained considerable attention for their ability to convert mechanical energy into electrical signals in a wide variety of environments, particularly where conventional power sources are impractical or undesirable. Their high sensitivity to low-frequency and small-amplitude mechanical disturbances makes them especially well-suited for deployment in wearable electronics, human–machine interfaces, and structural environments subjected to periodic vibrations or transient forces [49], [50], [51].

One of the most widely explored application areas is in wearable sensors, where TENGs harvest biomechanical energy from motion, such as walking, running, or joint flexion [119], [120]. This motion is then converted into either usable electrical energy or a measurable signal for real-time monitoring. For instance, a self-powered TENG-based gait sensor integrated into shoe insoles, capable of tracking step count and foot pressure distribution. These systems not only reduce dependence on external power but also offer the added benefit of being lightweight and conformable to the human body. Similarly, wristbands, knee supports, and smart clothing have all been developed using flexible TENGs to track body motion, respiration, and even subtle muscle contractions [121]. This is shown below in Figure 13.

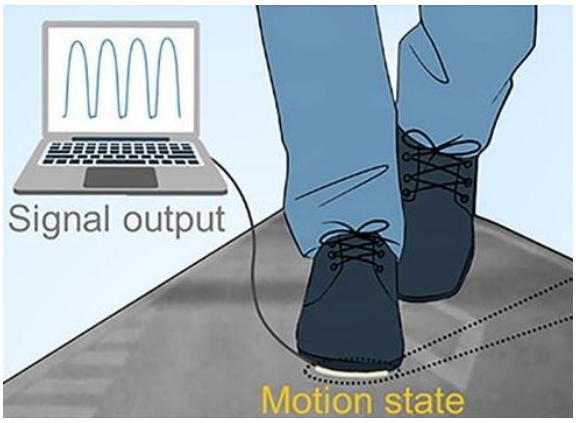

Figure 13: Motion capture mechanism for a TENG

TENGs have also been effectively employed to detect acoustic waves and machine-induced oscillations [122], particularly in environments where oscillatory motion occurs at low frequencies [123]. TENGs have been deployed to exploit the vertical oscillations of transportation systems, such as railway tracks, where passing trains generate rhythmic displacements of the rail relative to the sleeper. TENGs integrated into railroads to harvest energy from rail traffic demonstrated their potential to power wireless sensors embedded in smart systems [124]. One such smart system is shown in Figure 14.

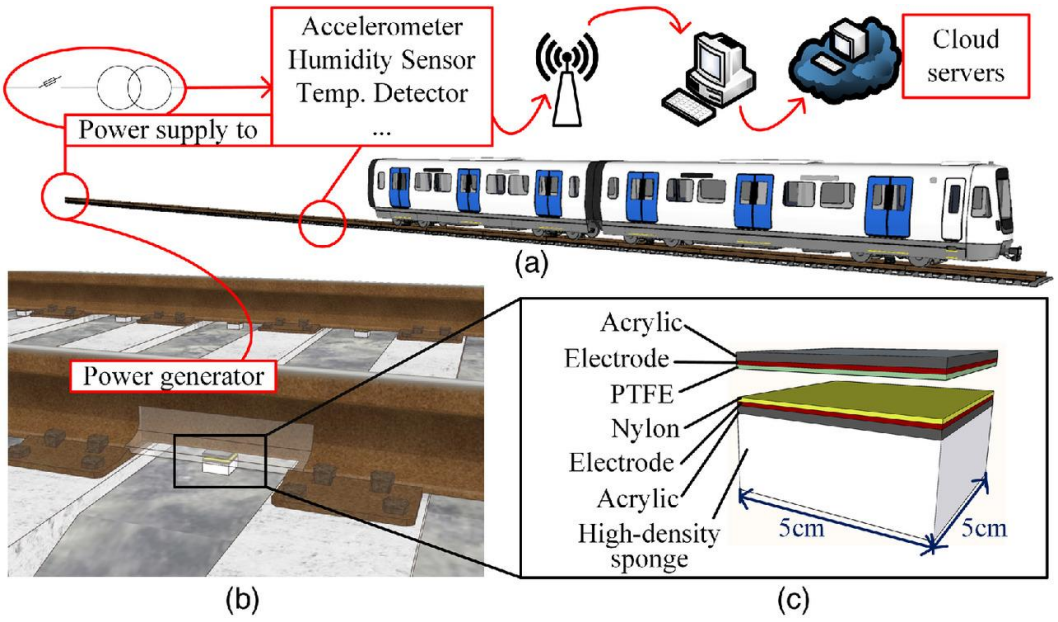

Figure 14: Layout for energy extraction from rails a) Energy Collection b) TENG Placement c) VS-TENG [124]

In vehicles, TENGs can be used to capture energy from suspension systems, where oscillations from road-induced vibrations are abundant and consistent [125]. These systems can power tire pressure monitors or other low-power vehicle health monitoring systems. Meanwhile, in stationary environments, TENGs have found application in touch-sensitive human-machine interfaces, where the contact and separation of a user's finger from a surface generates both energy and a signal. These have been used for smart switches, keyboards, and gesture-controlled interfaces, offering battery-free, responsive control systems. An example for a lateral sliding TENG mounted to the bearings of a train bogie is shown in Figure 15.

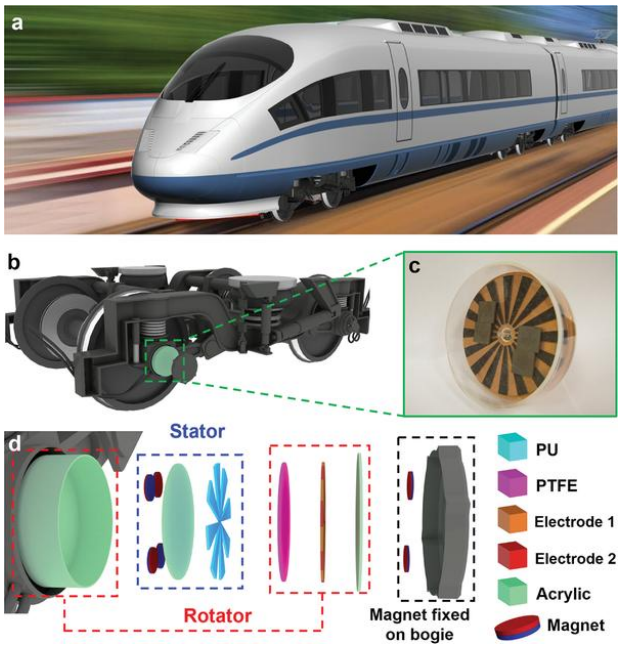

Figure 15: a) Train b) Stator location c) Stator d) Lateral sliding TENG [125]

Overall, the ability of TENGs to operate under ambient conditions and respond to common mechanical excitations whether human, structural, or vehicular make them a potentially flexible and sustainable solution for next-generation sensing and micro-energy harvesting platforms.

2.7 TENG manufacturing techniques

2.7.1 Soft Lithography

TENG manufacturing is mainly conducted inside highly controlled laboratory environments. The most common method is known as soft lithography, which enables the fabrication of microstructured polymer surfaces which increase the contact area and help with charge generation [126], [127]. The process typically involves molding elastomers like Polydimethylsiloxane (PDMS) using patterned templates to create surface textures which increase the effective contact area [128]. The method is shown in Figure 16.

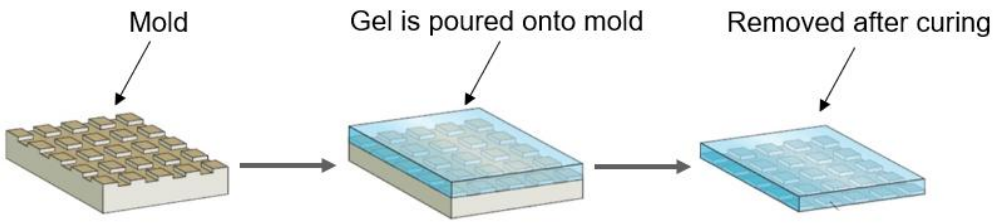

Figure 16: Soft Lithography

While highly effective for laboratory scale fabrication, it is generally time consuming and requires multiple preparation steps including the fabrication of a mold, and then material curing. It is also limited to material selections to elastomers, restricting the range of triboelectric materials that can be incorporated into the device design.

2.7.2 Screen Printing

Screen printing is another widely employed manufacturing technique for TENG fabrication [129], [130]. Conductive inks and/or pastes are deposited layer by layer through a pattern onto a substrate to create triboelectric layers. An example is shown below in Figure 17.

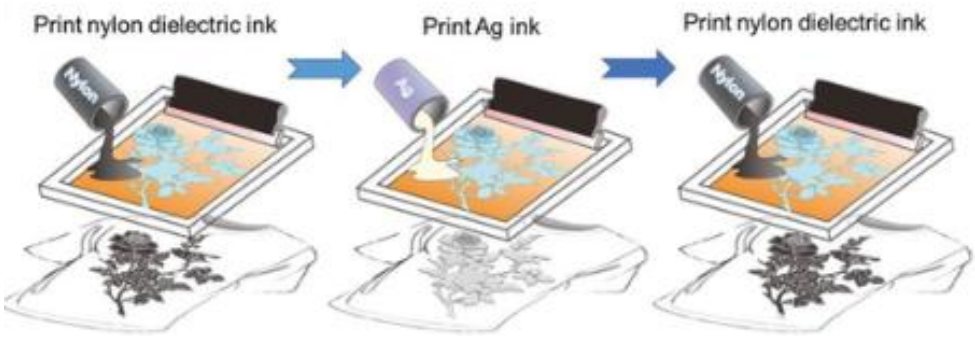

Figure 17: Screen printing [131]

The nature of this manufacturing process relies heavily on inks and slurries, which limits material selection heavily. Although this process can be scaled more easily than soft lithography, it has not been explored in a high level.

2.7.3 Spin Coating

Spin coating is frequently used to produce thin and uniform polymer films for triboelectric layers in TENGs. A liquid polymer solution is dispensed onto a substrate and rotated at a high speed to spread the material into a thin film. The method is highly effective for

producing coatings under controlled laboratory conditions but is restricted to solution processable materials [132], [133]. This process is shown below in Figure 18.

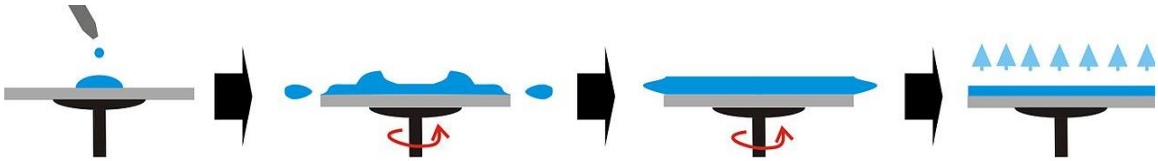

Figure 18: Spin coating [134]

2.7.4 CS as an alternative

Although TENGs have established manufacturing processes which have been demonstrated in research environments, they remain heavily laboratory oriented processes which can be difficult to scale for industrial production. These techniques often required controlled environments, multiple steps, and limited material selection. CS presents itself as a potential solution to these limitations because it enables the direct deposition of solid powders onto conductive substrates such as copper. Additionally, CS offers access to a significantly wider range of materials across the triboelectric series, as several materials already exist in powder form. Future development of coatings for specifically polymer powders could potentially provide a pathway towards a more standardized and scalable manufacturing of TENGs.

2.8 Polymer CS

Polymer coatings have had a variety of applications ranging from surface protection from corrosion, protection from cavitation erosion and mechanical impacts, electronic applications, and lately in hydrophobic coatings.

2.8.1 Perfluoroalkoxy Alkane (PFA)

CS has primarily been investigated for the development of hydrophobic and protective surface coatings using PFA [118], [135]. Due to the low surface energy and strong chemical resistance of PFA, cold sprayed coatings have demonstrated significant water-repellent behavior, making them attractive for anti-corrosion and anti-fouling applications. The CS process enables the deposition of PFA while minimizing thermal degradation, helping preserve the fluoropolymer's intrinsic hydrophobic properties. Additionally, the rough

surface morphology often produced during cold spray deposition can further enhance hydrophobicity by increasing surface texture and promoting water droplet repellency.

2.8.2 Nylon

Nylon has also been investigated as a polymer feedstock for cold spray applications due to its relatively low melting temperature, good impact resistance, and ability to deform upon particle impact. Cold sprayed nylon coatings have been explored for protective and wear-resistant applications, particularly where lightweight polymer coatings are desirable. The deposition process allows nylon particles to adhere to substrates through solid-state deformation and localized softening during high-velocity impact, while avoiding the extensive thermal degradation associated with conventional thermal spray methods. Additionally, nylon cold spray studies have demonstrated the feasibility of depositing polymer coatings onto metallic substrates, highlighting the potential of polymer cold spray as a manufacturing method for functional surface engineering applications [136].

3 THEORETICAL BACKGROUND

This chapter develops the important theoretical framework necessary to understand at a more detailed level the design and operation of VS-TENGs. First, the complete cycle is analyzed for detailed comprehension. From the fundamental principles of electrostatics and charge induction, the governing equations that relates the displacement of the triboelectric layers to the resulting voltages and currents are presented and shown at each step of the cycle. Additionally, an equation that characterizes the VS-TENG's efficiency is derived. The equations provide the basis for analyzing energy conversion efficiency and inform the optimization of TENG geometry and material selection.

3.1 Vertical Contact Separation

The most common working mode for TENGs is known as vertical contact separation, referred to as VS-TENGs. This configuration for TENGs is the most popular as vertical oscillations are both common in nature and in infrastructures, and the devices themselves are simple to configure and test. Dielectric films are deposited onto electrodes and are oriented such that the two dielectric films face each other. A dielectric is formed from a material that does not conduct electricity but can support an electric field. In the case of a VS-TENG, they are ideally also at opposite extremes of the triboelectric series. Physical contact between the dielectrics generates oppositely charged surfaces because of the triboelectric effect. Upon separation, a physical gap between the two surfaces is generated, and the difference in charge between the two surfaces, which remains constant, induces an electric field. A potential difference is also generated, which increases with the separation distance while the electric field remains constant. Continuing to increase the distance between the dielectrics increases the difference in potential between the two surfaces, which increases the voltage. If the electrodes are connected via a load, this potential difference forces electrons to flow between electrodes to balance the potential drop created by the opposite charges on the dielectrics. When equilibrium is reached, the overall potential between the electrodes is zero and electron flow stops. Reducing the gap will cause the electrons to flow back in the opposite direction as the potential between the two dielectric surfaces will drop. If the motion of separating and re-engaging contact becomes periodic, signals of alternating current will be continuously generated [4], [17]. This section

provides the detailed and thorough theory and operating principles which govern the parameters necessary to generate small current pulses from a VS-TENG operating with a vertical contact separation layout. A full cycle is laid out in Figure 19.

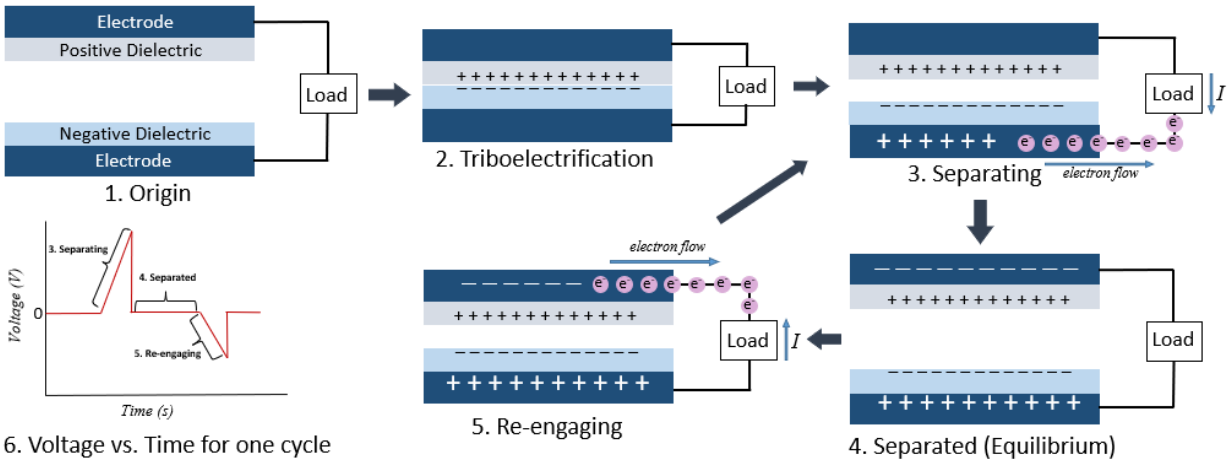

Figure 19: Full Operating Cycle for a VS-TENG with Voltage vs. Time generation

At the origin state 1, the two dielectric layers are not in contact with no external charge transfer occurring, and the terminal voltage is zero due to electrostatic equilibrium between the electrodes. Upon contact at 2, triboelectrification occurs at the dielectric interface, resulting in equal and opposite surface charge densities on the positive and negative dielectric layers while the electrodes remain electrically neutral. As the dielectrics begin to separate at 3, the change in electric potential induces a voltage between the electrodes, driving electron flow through the external load to balance the evolving electrostatic field in the air gap. When maximum separation occurs at 4, charge transfer through the external circuit ceases once electrostatic equilibrium is reached, corresponding to a stable terminal voltage under the imposed electrical boundary condition. When the dielectric layers are brought back into contact at 5, the reduction of the voltage in the air gap forces electrons to flow in the opposite direction through the load until the system returns to its initial electrical state. The voltage vs time response depicts the evolution of the voltage over a complete cycle, showing the voltage increase during separation, a plateau at maximum separation, and a directional reversal associated with re-engagement.

3.1.1 Electric Fields

A uniform electric field is characterized by a constant field magnitude and direction throughout a given region of space, resulting in a linear variation of electric potential with distance. Such fields commonly arise between large, parallel conductive or across dielectric surfaces when edge effects are negligible, as shown in Figure 20.

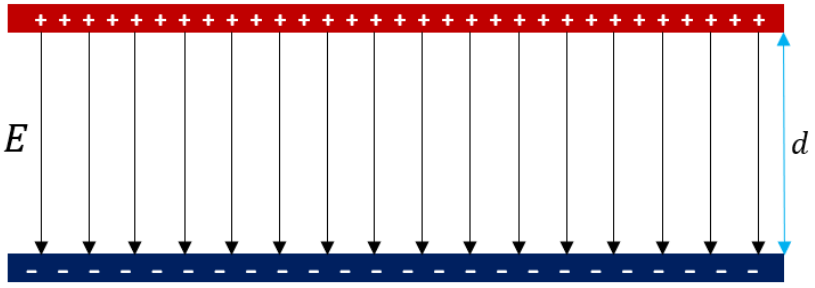

Figure 20: Uniform electric field across two charged plates (similar to the dielectric surfaces after tribo-electrification)

Under these conditions, the electric field (E) can be considered spatially invariant and constant, allowing the potential difference (V) across the region to be expressed as the product of the field strength and separation distance. The voltage across the distance d between the two plates is defined as the product of the electric field E and distance d

$$V = Ed \tag{1}$$

In the case of a VS-TENG, the separation distance $x(t)$ between the two layers is much smaller compared to the width w,

$$x(t) << w$$

This is illustrated in Figure 21.

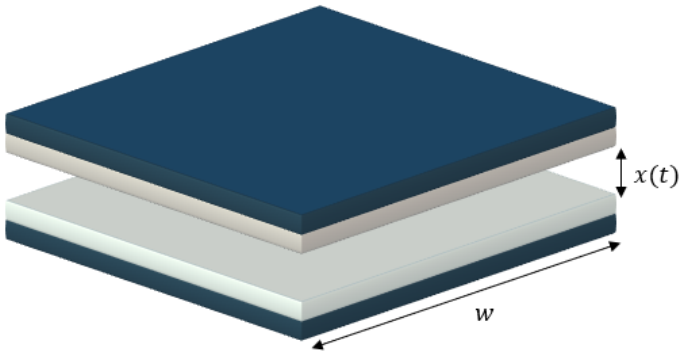

Figure 21: 3D view of a VS-TENG showcasing w and x(t)

Therefore, assuming uniform electric fields is appropriate.

The electric field equations are derived from Gauss's law for electric fields, which states fundamentally that the flux of an electric field out of an arbitrary closed surface is proportional to the electric charge enclosed by that surface, irrespective of how that charge is distributed. In integral form, it is expressed as,

$$\oint E \cdot dA = \frac{Q_{encl}}{\varepsilon_0}$$

Here, the term on the left-hand side of the equation is known as the Electric Flux and is expressed as the path integral through a closed surface of the dot product of an electric field E and an infinitesimal area element dA. On the right, Q_{encl} represents the net total charge encompassed inside a closed surface, known as the Gaussian surface. The permittivity of free space, denoted by ε_0, is a fundamental physical constant that quantifies how much electric field is produced per unit charge in a vacuum. It measures the ability of free space to "permit" electric field lines, relating electric flux to the enclosed charge in Gauss's law and determining the strength of electrostatic interactions in a vacuum. For a dielectric material, Gauss' law can be used to express the electric fields as,

$$E_1 = \frac{Q}{A\varepsilon_0\varepsilon_{r1}} \tag{2}$$

$$E_2 = \frac{Q}{A\varepsilon_0\varepsilon_{r2}} \tag{3}$$

Where ε_0 is the permittivity of free space, ε_r the relative permittivity of the dielectric, A is the surface area, and Q the surface charge. A full derivation of equations 2 and 3 for the general case is shown in Appendix A.

In a VS-TENG, there are four steps completing one full cycle: rest, contact, separation, and re-engaging. Three sections within the VS-TENGs structure will have electric fields present, which are the two dielectrics and the air gap. The three electric fields are shown in Figure 22.

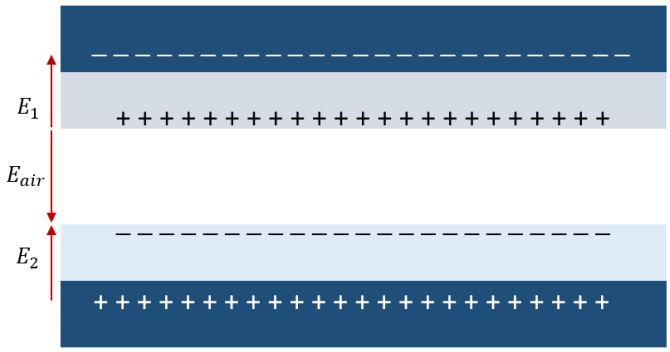

Figure 22: Electric fields in a VS-TENG

While electric fields are present within these three regions, their existence, and relative magnitude depend on the specific stage of the VS-TENG operating cycle. As the device transitions between rest, contact, separation, and re-engagement, the spatial distribution of the electric fields evolves accordingly. The following section examines each stage of the operating cycle in detail and describes when and how these electric fields arise.

3.1.2 Open and short circuit conditions

In a VS-TENG, the electrical behavior can be described using the two limiting conditions of open circuit and short circuit operation. These represent the maximum voltage and maximum charge transfer states of the device, respectively.

Under open-circuit conditions, the external resistance is theoretically infinite, meaning no current can flow between the electrodes. Since there is no charge transfer through the external circuit, the transferred charge is zero, meaning $Q = 0$. However, the separation of the triboelectric layers creates the maximum potential difference between the electrodes, resulting in the highest possible voltage, known as the open circuit voltage, denoted as V_{OC}.

The open circuit operation is therefore characterized by maximum voltage and zero transferred charge (Q=0).

Under short-circuit conditions, the external resistance is zero, allowing charges to flow freely between the electrodes. In this state, the potential difference between the electrodes becomes zero because the charges immediately neutralize through the external connection. As a result, the transferred charge reaches its maximum value, corresponding to the maximum short-circuit charge, Q_{SC}. The short circuit operation is therefore characterized by zero voltage $V = 0$ and maximum charge transfer Q_{SC}.

These two conditions define the operating limits of a TENG and are commonly used to evaluate device performance.

3.1.3 Rest and contact

In the resting state, before any motion or contact has occurred, the two layers of the TENG are separated by the air gap, and the system is electrically neutral. No charges have been transferred between the surfaces, so no electric fields are present. At this stage, the VS-TENG is in its initial equilibrium condition, ready for the first contact of the operating cycle. The triboelectric materials are placed on top of the electrodes and are oriented such that they are facing each other. A VS-TENG at rest is shown below in Figure 23.

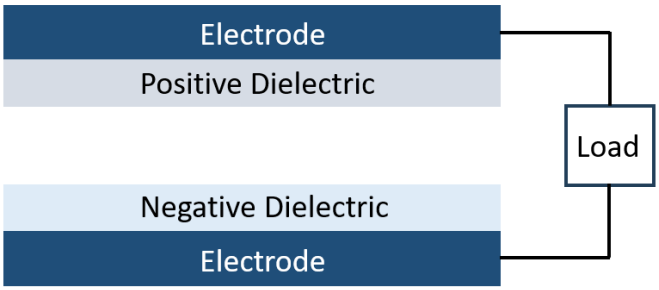

Figure 23: VS-TENG at rest, with electrodes and dielectrics

After an external mechanical input exerts itself to bring the two dielectric layers into contact with one another, surface charge transfer occurs along the area of contact. As per the triboelectric effect, electrons cross over towards the material with the higher electron affinity, also called the negative dielectric, from the material with the tendency to donate its electrons, known as the positive dielectric. This generates equal and opposite charges

on the surfaces of the dissimilar materials. These charge densities are denoted using σ. This is shown in Figure 24.

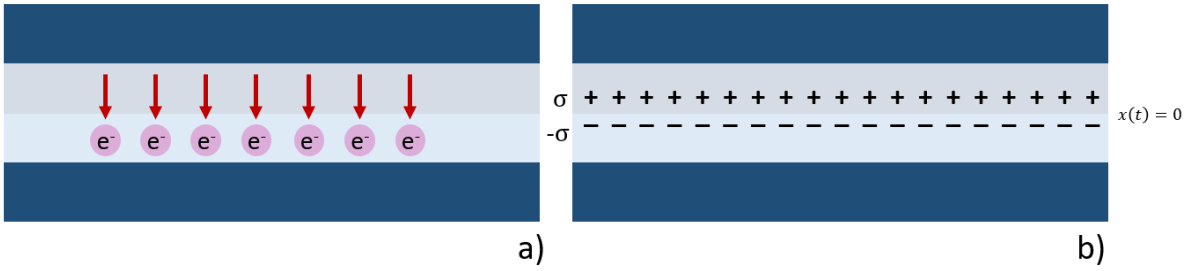

Figure 24: Electrons crossing over to tribonegative material b) Charges on each side after equilibrium

Because of the charge transfer, an electric field is now present between the dielectrics, which is defined as the surface charge density σ over the permittivity of free space, ε_0.

$$E = \frac{\sigma}{\varepsilon_0} \tag{4}$$

however, since there is no separation, $x(t) = 0$. This means that once contact is established, from equation 1,

$$V = Ed = Ex(t) = 0$$

The voltage signal generated during the contact phase is shown below in Figure 25.

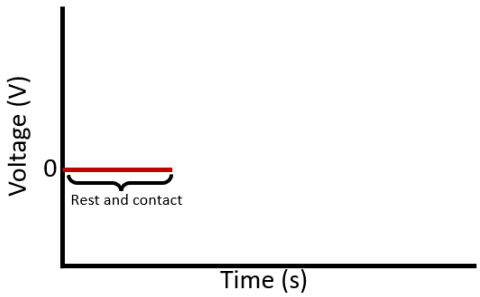

Figure 25: Voltage signal during rest and contact phase

3.1.4 Separation

Separating the two triboelectric layers without connecting the electrodes together such that no path for current exists, will initiate a voltage between the positive and negative

dielectrics from the change in distance. Figure 26 shows a separated TENG not connected to a circuit.

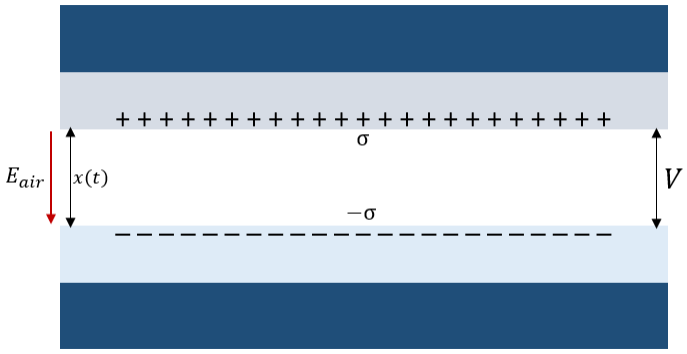

Figure 26: Electric field and voltage between dielectrics of an unconnected TENG

Combining equation 1 with equation 2 to get the voltage at this state gives,

$$V = Ed = \frac{\sigma}{\varepsilon_0} x(t)$$

The voltage at this point is between the surfaces of the dielectrics and is referred to as the open-circuit voltage, V_{oc}. It is the highest achievable voltage for a TENG, as there is no conductive path for charge to flow and equalize the potential difference. In this open-circuit condition, the electric field in the air gap is fully established according to the separation distance, and the surface charges on the dielectrics create the maximum potential difference. It is expressed as,

$$V_{oc} = \frac{\sigma x(t)}{\varepsilon_0} \tag{5}$$

From equation 5, there is a linear relationship between V_{oc} and $x(t)$. This would suggest that V_{oc} would increase indefinitely with separation distance. The primary assumption used to derive equation 5 is that a fixed surface charge density and infinite parallel plate geometries are used. In practice, this is not the case after a certain separation distance. If the separation becomes too large, then the separation distance $x(t)$ is no longer much smaller than the width of the TENG w, meaning that $x(t) \not\prec w$ invalidating this primary assumption. The real effective charge that contributes to the electric field is set by

electrostatic induction, which decreases as separation increases because of weakening capacitance between the triboelectric surfaces.

Once the electrodes are connected through an external circuit, this would cause the system to short. This voltage can now drive current flow, allowing the TENG to perform electrical work. The flow of electrons now generates a charge Q of equal and opposite magnitude on the electrodes, as the electrons one electrode loses are what the other gains. In action, this is shown demonstratively in Figure 27.

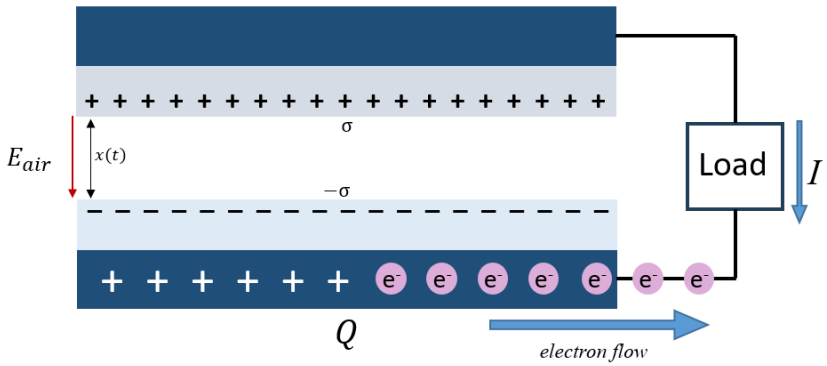

Figure 27: Direction of electron flow with residual charge Q being generated

Electrons move between the electrodes via the external circuit, driven by the voltage across the air gap, until the potential difference is balanced. Once complete, Figure 28 shows all electric fields and charges Q present after separation has completed.

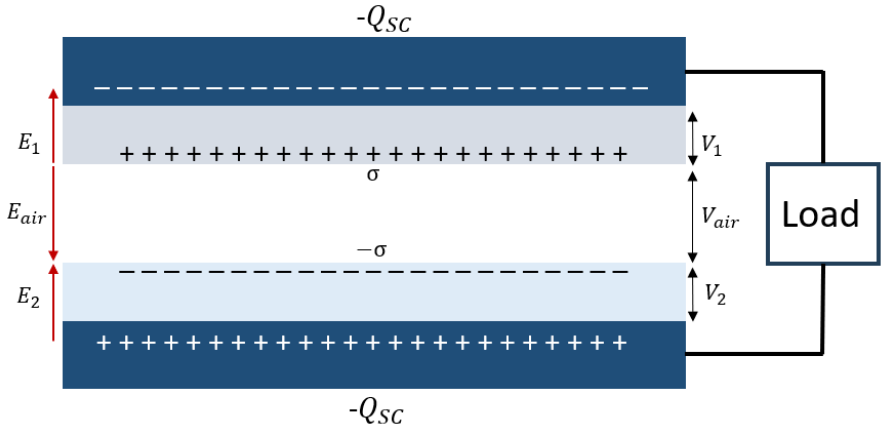

Figure 28: All electric fields and charges present after separation

Additionally, as separation is what drives current, and in this instance, there is no motion, measured voltage will drop to zero as the voltage inside the air gap balances out with the voltages inside the dielectrics. This means that,

$$V_{air} = V_1 + V_2$$

The measured voltage signal will remain at zero, shown in Figure 29.

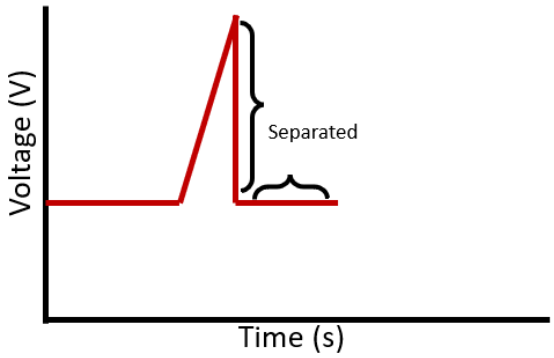

Figure 29: Voltage dropping and maintaining zero while separated

Here, three electric fields are present, which means that the voltage drop across the electrodes will be the sum of the product of each electric field and its distance. The electric fields inside the dielectrics both oppose the electric field in the air gap. Because at this state all electrons have crossed over leaving charges on the electrodes meaning that $Q \neq 0$, the systems voltages are balanced, so the measured voltage $V = 0$.

This means that,

$$0 = -E_1 d_1 + E_{air} x(t) - E_2 d_2 \quad (6)$$

The presence of Q reduces the strength of the electric field (E_{air})in the air gap, because of the pull from the shielding effect caused by E_1 and E_2. The triboelectric surface charges by themselves generate an electric field in the air gap with magnitude σ/ε_0, shown earlier in equation 4, directed from the positively charged dielectric toward the negatively charged dielectric. When the electrodes are connected through an external circuit, electrons transfer between them, resulting in a net charge Q on the electrodes. This induced electrode charge produces an opposing electric field across the air gap, analogous to a parallel-plate capacitor, with magnitude $Q_{SC}/A\varepsilon_0$.

By the principle of superposition, the total electric field in the air gap is equal to the algebraic sum of these two contributions. Because the field generated by the electrode charges opposes the triboelectrically induced field, the resulting air-gap electric field is reduced, yielding

$$E_{air} = \frac{\sigma}{\varepsilon_0} - \frac{Q_{SC}}{A\varepsilon_0} \tag{7}$$

Substituting the expressions for the dielectric electric fields E_1 and E_2, obtained from Gauss's law (equations 2 and 3), together with the modified expression for the air-gap electric field E_{air} (equation 7), along with applying the boundary conditions,

$$0 = \left(\frac{-Q_{SC}}{A\varepsilon_0\varepsilon_{r1}}\right) d_1 + \left(\frac{\sigma}{\varepsilon_0} - \frac{Q_{SC}}{A\varepsilon_0}\right) x(t) + \left(\frac{-Q_{SC}}{A\varepsilon_0\varepsilon_{r2}}\right) d_2$$

Collecting terms and simplifying,

$$\frac{Q_{SC}}{A\varepsilon_0}\left(\frac{d_1}{\varepsilon_{r1}} + \frac{d_2}{\varepsilon_{r2}} + x(t)\right) = \frac{\sigma x(t)}{\varepsilon_0} \tag{8}$$

The term on the right-hand side is identical to equation 5, which is V_{oc} itself. Therefore,

$$V_{oc} = \frac{Q_{SC}}{A\varepsilon_0}\left(\frac{d_1}{\varepsilon_{r1}} + \frac{d_2}{\varepsilon_{r2}} + x(t)\right) \tag{9}$$

The open circuit voltage is balanced out by what is inside the dielectrics and air gap.

The operating mode referred to as the short-circuit condition is the one in which the electrodes are electrically connected, allowing unrestricted charge transfer and enabling the determination of the maximum current that the VS-TENG can deliver.

Isolating equation 7 for Q_{sc} gives,

$$Q_{sc} = \frac{\sigma A x(t)}{\frac{d_1}{\varepsilon_{r1}} + \frac{d_2}{\varepsilon_{r2}} + x(t)} \tag{10}$$

Which is known as the short circuit charge for a VS-TENG with a separation distance $x(t)$. As current is simply the amount of charge transferred over time, taking the derivative of this equation yields the short circuit current, the current at zero voltage, which is the highest possible current which can be supplied by the generator.

$$I_{sc} = \frac{dQ_{sc}}{dt} = \frac{\sigma A\dot{x}(t)\left(\frac{d_1}{\varepsilon_{r1}} + \frac{d_2}{\varepsilon_{r2}}\right)}{\left(\frac{d_1}{\varepsilon_{r1}} + \frac{d_2}{\varepsilon_{r2}} + x(t)\right)^2} \tag{11}$$

For simplification, the terms referring to the thicknesses of the dielectrics and their respective relative permittivity can be denoted as one term, d_0, expressed below as,

$$d_0 = \frac{d_1}{\varepsilon_{r1}} + \frac{d_2}{\varepsilon_{r2}} \tag{12}$$

Substituting in equation 11 simplifies the final equation for both Q_{sc} and I_{sc}, which completes the short circuit equations:

$$Q_{sc} = \frac{\sigma A x(t)}{d_0 + x(t)} \tag{13}$$

$$I_{sc} = \frac{dQ_{sc}}{dt} = \frac{\sigma A\dot{x}(t) d_0}{\left(d_0 + x(t)\right)^2} \tag{14}$$

3.1.5 Re-engaging

Once re-engaged, the voltage in the air gap becomes 0 as $x(t) = 0$. However, the electric fields in the dielectrics E_1 and E_2 remain, and because of the presence of Q_{sc}. The schematic illustrating the re-engaged case is shown in Figure 30.

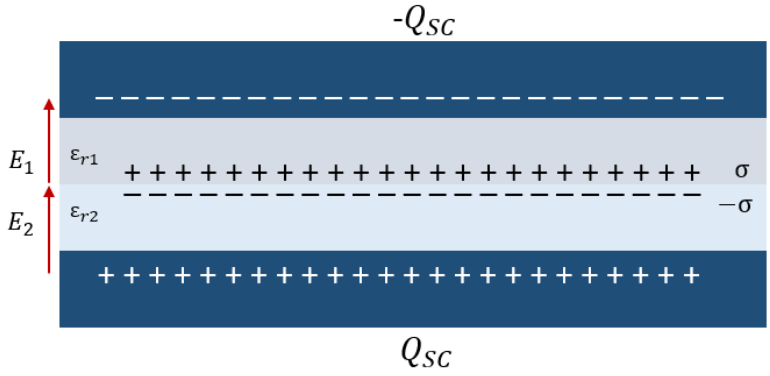

Figure 30: Electric fields and charges present after re-engaging

Since only the dielectric electric fields E_1 and E_2 are present and no voltage exists in the air gap, the overall voltage can be expressed as

$$V = -E_1 d_1 - E_2 d_2$$

The negative signs arise from the chosen directional conventions.

Substituting equations 2 and 3, which are the expressions for the electric fields in the dielectrics gives,

$$V = \left(\frac{-Q_{SC}}{A\varepsilon_0\varepsilon_{r1}}\right)d_1 + \left(\frac{-Q_{SC}}{A\varepsilon_0\varepsilon_{r2}}\right)d_2$$

This simplifies to,

$$V = \frac{-Q_{SC}}{A\varepsilon_0}\left(\frac{d_1}{\varepsilon_{r1}} + \frac{d_2}{\varepsilon_{r2}}\right) \tag{15}$$

As a result of equation 15, the voltage at this stage, referred to as V', does not reach the same magnitude as the open-circuit voltage V_{oc}, and instead assumes a smaller value of opposite polarity. This asymmetry between the separation and re-engagement stages implies an asymmetric voltage output characteristic of the VS-TENG. Since voltage is what drives the current, an asymmetric current output will also be read. The full voltage waveform is shown below for a full cycle in Figure 31.

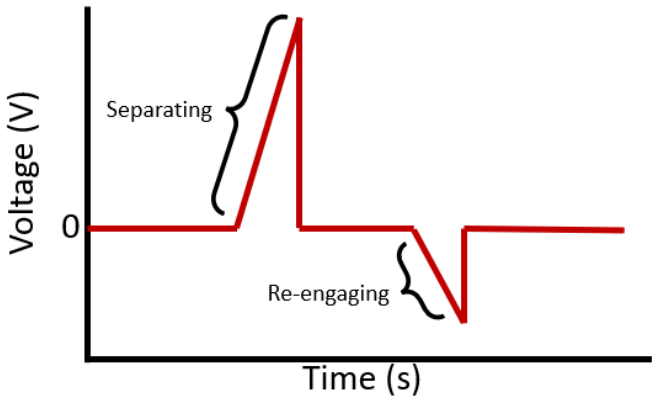

Figure 31: Voltage output for a cycle (note the asymmetry between separating and re-engaging)

When the VS-TENG re-engages, charges between the electrodes begin to move back in the opposite direction, correcting for the change in electric field distribution caused by the decreasing separation distance that reduces $x(t)$ and therefore V_{air}. This action is shown in Figure 32.

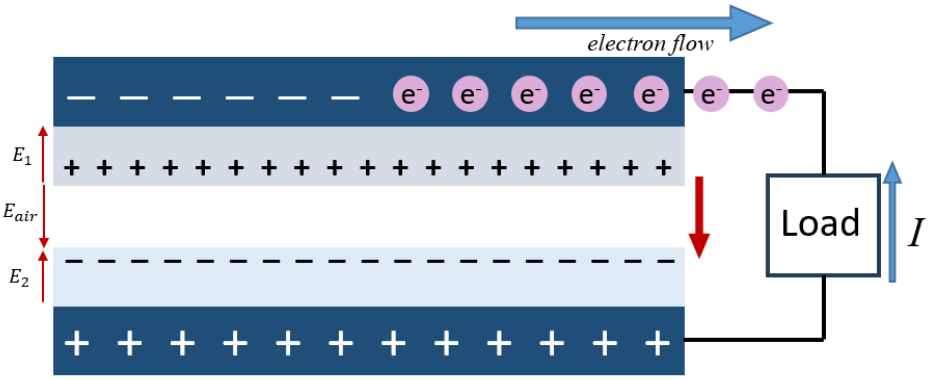

Figure 32: Charge flowing in the opposite direction upon re-engaging

3.1.6 The general governing equation

A VS-TENG that is under general operating conditions, is shown below in Figure 33 with all acting electric fields producing voltages, and all active charges.

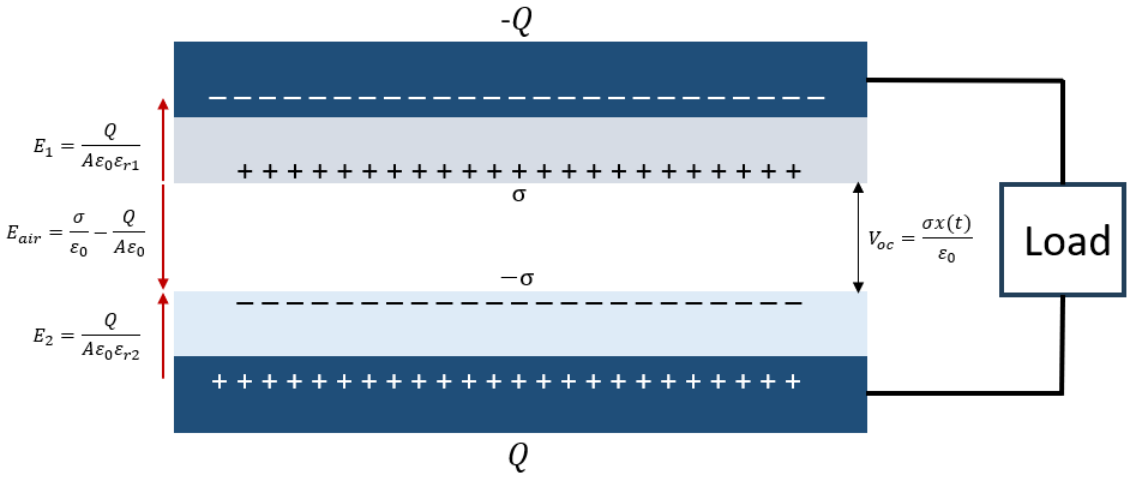

Figure 33: General case for a VS-TENG

The voltage is still expressed as the sum of all the products of electric fields and distances. However, $V \neq 0$, unlike in the short circuit condition.

$$V = -E_1 d_1 + E_{air} x(t) - E_2 d_2$$

Substituting in equations 2, 3, and 7, gives,

$$V = \left(\frac{-Q}{A\varepsilon_0\varepsilon_{r1}}\right) d_1 + \left(\frac{\sigma}{\varepsilon_0} - \frac{Q}{A\varepsilon_0}\right) x(t) + \left(\frac{-Q}{A\varepsilon_0\varepsilon_{r2}}\right) d_2$$

Simplifying this gives,

$$V = \frac{-Q}{A\varepsilon_0}\left(\frac{d_1}{\varepsilon_{r1}} + \frac{d_2}{\varepsilon_{r2}} + x(t)\right) + \frac{\sigma x(t)}{\varepsilon_0} \tag{16}$$

Which is the general form for the governing equation, showing all variables in which a VS-TENG operates [137], [138], [139]. Physically therefore, the voltage can be increased by maximizing the available surface area A and separation distance $x(t)$. The dielectric thicknesses d_1 and d_2 should be minimized to limit the production of negative voltage, while dielectric constants ε_{r1} and ε_{r2} which comes from material selection should be maximized for the same reason. The surface charge density σ should be maximized by ensuring the highest possible charge transfer between dielectrics during triboelectrification. This is done by selecting materials on opposite ends of the triboelectric series.

The governing equation for the total voltage in a VS-TENG combines the principles of capacitive behaviour and triboelectric charge generation. It can be further simplified and said that the total voltage is the difference between the open circuit voltage V_{oc} which arises from the triboelectric charges and the capacitive voltage which depends on the stored charge Q and the capacitance abilities from the selected dielectrics. As the capacitance changes with separation distance, this can be denoted as $C(x)$. Recall that the definition of electrical potential in terms of charge and capacitance is,

$$V = \frac{Q}{C} \tag{17}$$

Where Q is charge and C is the capacitance. Physically what this means, is that a high capacitance system can store more charge for the same voltage. Using these definitions to rewrite the governing equation for the total voltage in terms of fundamental electrical principles gives,

$$V = -\frac{Q}{C(x)} + V_{OC} \tag{18}$$

At the short circuit condition; $V = 0$ and $Q = Q_{SC}$. This means that equation 18 becomes,

$$0 = -\frac{Q_{SC}}{C(x)} + V_{OC}$$

So,

$$\frac{1}{C(x)} = \frac{V_{OC}}{Q_{SC}} \tag{19}$$

Substituting equation 19 into equation 18 gives,

$$V = -Q\left(\frac{V_{OC}}{Q_{SC}}\right) + V_{OC}$$

A linear relationship between V_{OC}, V, Q and Q_{SC} is therefore made as,

$$V = V_{OC} - V_{OC}\left(\frac{Q}{Q_{SC}}\right) \tag{20}$$

A similar relation for V' can also be formed starting from equation 18. When re-engaged, $x = 0$, which means that $V_{OC} = 0$, and $C(x) = C(0)$. Equation 18 then becomes,

$$V = -\frac{Q}{C(0)} \tag{21}$$

From the definition of electrical potential equation 17, at V', $Q = Q_{SC}$, and since $x = 0, C(x) = C(0)$. This means that,

$$V' = \frac{Q_{SC}}{C(0)} \tag{22}$$

Dividing equation 21 by equation 22 gives,

$$\frac{V}{V'} = \frac{-\frac{Q}{C(0)}}{\frac{Q_{SC}}{C(0)}} = \frac{Q}{Q_{SC}}$$

Isolating for V gives,

$$V = -V'\frac{Q}{Q_{SC}} \tag{23}$$

Equations 20 and 23 are the linear equations for the V-Q relationship.

3.1.7 Work and Cycle Efficiency

As all triboelectric nanogenerators operate under a cycle, the mechanical efficiency can be determined as a ratio of the input and output work done on the device. The calculation of

electrical work generated for an electric generator is similar in concept to the generation of mechanical work for a heat engine. Recall, mechanical work is the energy transferred when a system's volume changes under pressure. It is positive if the system expands, and work is done on the surroundings, while negative work occurs when a system is compressed. Mathematically, this can be expressed as,

$$W = \oint P dV \tag{24}$$

Where P is pressure and dV is the element of volume.

Similarly in electricity, work is the energy transferred when a charge moves under the influence of an electrical potential difference, a voltage. Mathematically this can also be expressed as a line integral as,

$$W = \oint V dQ \tag{25}$$

Where V is voltage and dQ represents an element of charge. Both heat engines and electric generators are devices which convert an input of energy to work which can be utilized, a simple diagram in Figure 34 visualizes this below.

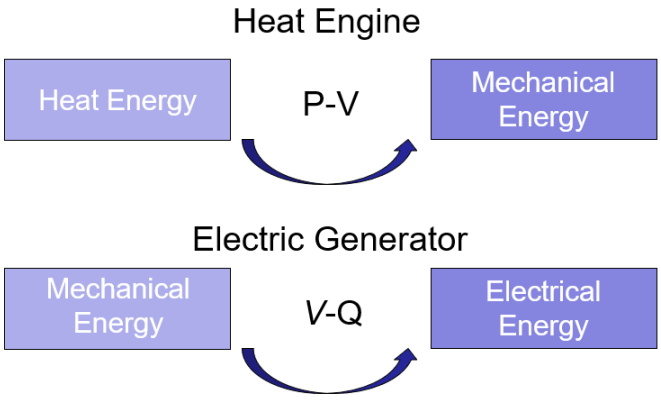

Figure 34: Work generation schematic for heat engines and electric generators

As a Carnot cycle for heat engines composes of two isothermal and two adiabatic processes, the ideal cycle of a VS-TENG can be expressed as two open circuit and two closed circuit processes. Illustration of the operation of this cycle on V-Q diagrams is shown below in Figures 35 and 36.

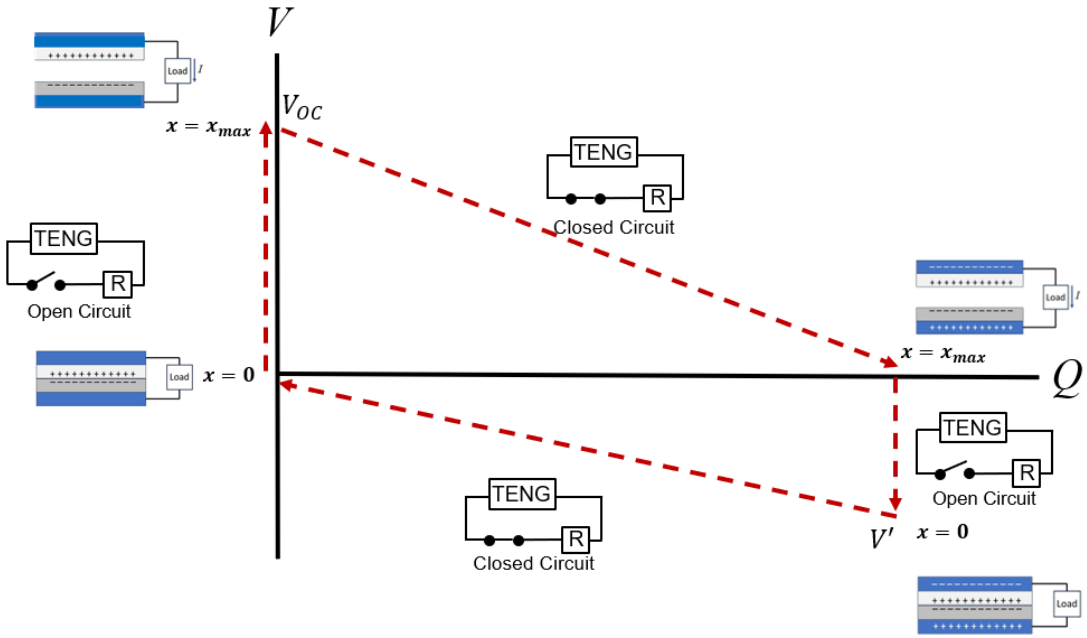

Figure 35: Ideal VS-TENG Cycle

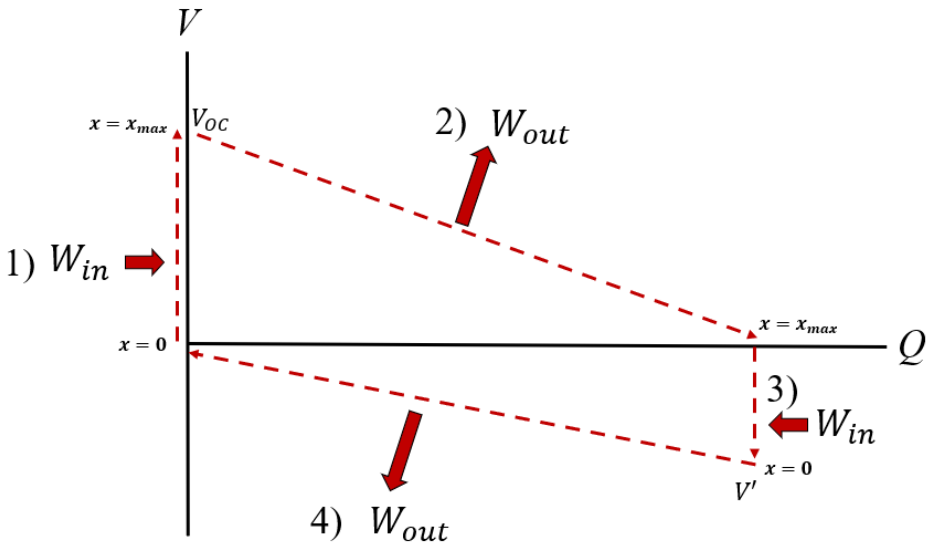

Figure 36: Work input and output for a VS-TENG

Using the linear voltage–charge equations 20 and 23 derived in Section 3.1.5, the corresponding expressions are incorporated into the TENG operating cycle, as illustrated in Figure 37.

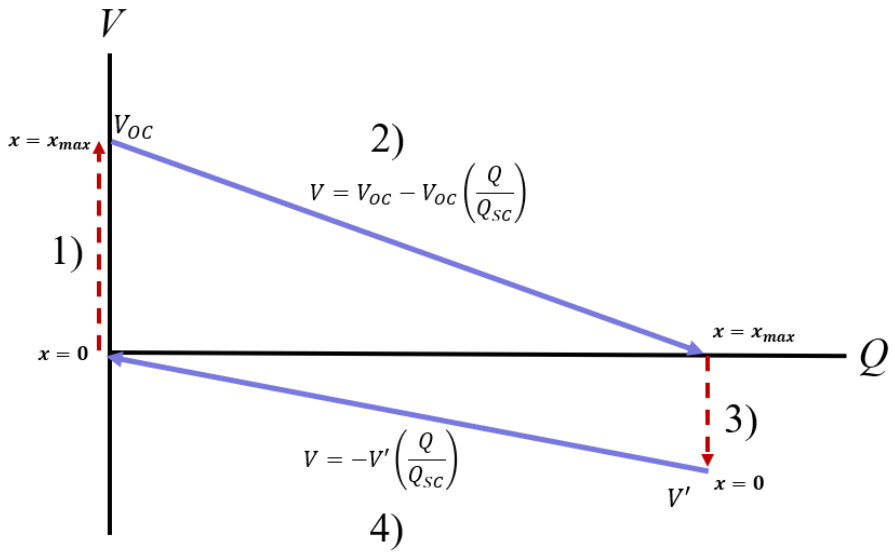

Figure 37: TENG Cycle with Voltage-Charge relationships at processes 2) and 4)

The 1st process in the cycle starts at contact, where the separation distance $x = 0$ and triboelectrification has already occurred between the positive and negative dielectrics leaving both surfaces charged with equal and opposite charges. An external mechanical output which separates the layers in an open circuit condition means that the voltage will increase until $x = x_{max}$ ending the process. The voltage at this point is V_{OC}, and as the condition is open circuit $Q = 0$. The 2nd process closes the circuit, allowing current to flow. Subsequently a charge $+Q$ and $-Q$ appears on the electrodes. The entire process occurs entirely at $x = x_{max}$. Closing the circuit once again for the 3rd step in the cycle and compressing the TENG back into contact maintains the charges on the electrodes, but a residual voltage remains, which is V'. The 4th step occurs entirely at $x = 0$ and as the separation distance $x(t)$ decreases, the capacitance $C(x)$ increases, which means the charges at the electrodes Q must redistribute in the opposite direction, going back to the rest state [139], [140].

To determine the cycle efficiency, first the definition of efficiency $\eta_o$here is,

$$\eta_o = \frac{W_{out}}{W_{in}} \tag{26}$$

First, to determine the output work, it is important to notice that output work only occurs in steps 2) and 4) in the cycle. These processes can be expressed in terms of voltage V and Q using equation 18. Therefore,

$$W_{out} = W_{out2} + W_{out4} = \int V_1 dQ + \int V_2 dQ \tag{27}$$

Recall from previous definitions, the highest possible charge transfer between electrodes is Q_{sc}, and the highest possible voltage is the open circuit voltage V_{OC}. This defines our integral bounds for charge from $0 \leq Q \leq Q_{sc}$. The smallest operating voltage in the cycle is V', which is mathematically defined as the voltage when $Q = Q_{sc}$. The expression for V_1 occurs for process 2), which is bounded by the equation 20. Similarly, V_2 occurs in process 4), and equation 23 provides the lower bound for the cycle. Substituting equations 20 and 23 for V_1 and V_2 respectively gives,

$$W_{out} = \int_0^{Q_{sc}} \left(V_{oc} - V_{oc}\frac{Q}{Q_{sc}}\right) dQ + \int_{Q_{sc}}^0 \left(-V'\frac{Q}{Q_{sc}}\right) dQ$$

Integrating,

$$W_{out} = V_{oc}Q_{sc} - V_{oc}\frac{{Q_{sc}}^2}{2Q_{sc}} + V'\frac{{Q_{sc}}^2}{2Q_{sc}}$$

This simplifies to,

$$W_{out} = \frac{1}{2}Q_{sc}(V_{oc} + V') \tag{29}$$

The input work for a VS-Teng in the ideal case is equal to the variation of electrostatic energy. In an ideal TENG, assumptions must be made. Firstly, quasi static operation is assumed. This means that during mechanical separation and contact the electric field adjusts instantaneously to changes in displacement, and any dynamic electromagnetic effects such as inductance are negligible. This allows electrostatics to be used.

The efficiency in an ideal TENG represents an upper bound, which means the system has no losses. This means there is no internal resistance in the electrodes and connections are neglected and no losses inside the dielectrics. Finally, the triboelectric charges are assumed to be constant and uniform.

The mechanical work, which is expressed as,

$$W_{in} = \oint F dx \tag{30}$$

provides the energy necessary for separation and re-engagement. The variation of electrostatic energy (E_s) with respect to a global or local reference point in an electrical system is expressed as a sum of the products of charges Q and their respective potentials Φ.

$$E_s = \frac{1}{2}\sum Q_i \Phi_i \tag{31}$$

Electric potential is measured as a voltage, however the symbol V is not used in this case as this potential is not the same as the voltage V in the TENG system.

By assuming energy conversion, the variation of electrostatic energy comes from two factors. The first is the input work which overcomes the electrostatic force. The second is electrical output, which decreases electrostatic energy, converting it to current. This means that,

$$\Delta E_s = \oint F dx \; - \oint V dQ$$

However, processes 1) and 3) operate under open circuit conditions, meaning that $dQ = 0$. This means that,

$$W_{in} = \Delta E_s = \oint F dx \tag{32}$$

Therefore, for an ideal system, the minimum required input work is equal to the variation of electrostatic energy.

For the case of the VS-TENG, the surface of bottom dielectric layer is set as the reference point. At the reference, the variation of electrostatic energy is zero as the potential at the reference point is zero. Recall that from the definition of capacitance, electric potential can be written as,

$$\Phi = \frac{Q}{C}$$

The reference point along with the charges present in the VS-TENG is shown in Figure 38.

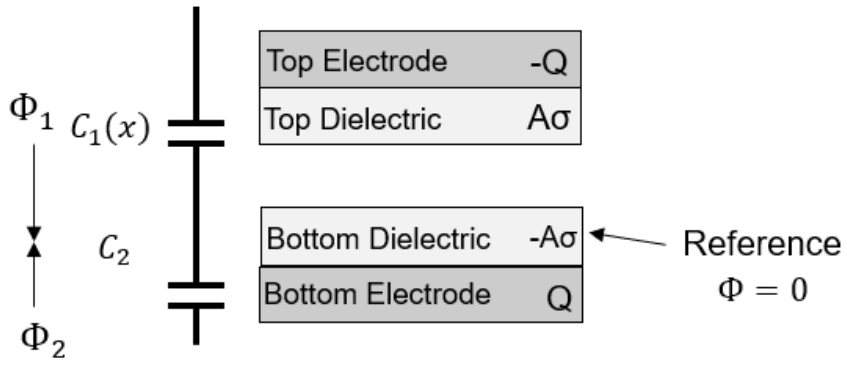

Figure 38: Schematic showing the reference point for a VS-TENG along with charges present

The VS-TENG is then split into two regions of capacitance about the reference point called $C_1(x)$ which varies with separation distance and C_2 which remains constant. Similarly, there are two potentials Φ_1 and Φ_2 from the reference point. The equation for electrostatic energy as a function of distance x and charge Q is therefore,

$$E_s(x, Q) = \frac{1}{2}\sum Q_i \Phi_i = \frac{1}{2}(E_{s1} + E_{s2})$$

Substituting the charges at each potential gives,

$$E_s(x, Q) = \frac{1}{2}(Q\Phi_2 + (A\sigma - Q)\Phi_1) \tag{33}$$

Finally, substituting the definition for potentials with respect to the reference point yields,

$$E_s(x, Q) = \frac{1}{2}\left(Q\frac{Q}{C_2} + (A\sigma - Q)\frac{A\sigma - Q}{C_1(x)}\right) \tag{34}$$

Which is the general expression for electrostatic energy as a function of x and Q.

For the input work W_{in1} at the 1st step, process begins at $x = 0$ and terminates at $x = x_{max}$, with the entire process being at open circuit, meaning that $Q = 0$. The variation of electrostatic energy is just the difference of the potentials at $x = x_{max}$ and $x = 0$, shown below as,

$$W_{in1} = \Delta E_s = E_s(x_{max}, 0) - E_s(0,0) = \frac{1}{2}\left((A\sigma)\frac{A\sigma}{C_1(x_{max})} - (A\sigma)\frac{A\sigma}{C_1(0)}\right)$$

For a capacitance at zero distance $C_1(0)$ the capacitance approaches infinity. The final equation for simplifies to,

$$W_{in1} = \frac{1}{2}\frac{(A\sigma)^2}{C_1(x_{max})} \tag{35}$$

In the first step of the process which involves separation, the external force does positive work and the electrostatic energy of the system increases. During the third step, where the VS-TENG is re-engaged, the external force does negative work on the system, decreasing the electrostatic energy of the system, meaning it is negative. For this reason, only the work input in the first step is considered. The work W_{in3} is shown below using the same steps for W_{in1}, with the only difference being that a charge Q is present.

$$W_{in3} = E_s(0, Q) - E_s(x_{max}, Q)$$
$$= \frac{1}{2}\left(Q\frac{Q}{C_2} + (A\sigma - Q)\frac{A\sigma - Q}{C_1(0)}\right) - \frac{1}{2}\left(Q\frac{Q}{C_2} + (A\sigma - Q)\frac{A\sigma - Q}{C_1(x_{max})}\right)$$

Which simplifies to,

$$W_{in3} = -\frac{1}{2}\frac{(A\sigma - Q)^2}{C_1(x_{max})} \tag{36}$$

A negative quantity, which means this term can be excluded.

Substituting all the determined quantities for output and input works, the un-simplified equation therefore for the efficiency of a VS-TENG is,

$$\eta_o = \frac{\frac{1}{2}Q_{sc}(V_{oc} + V'))}{\left(\frac{1}{2}\frac{(A\sigma)^2}{C_1(x)}\right)} \tag{37}$$

From equation 17 in the previous section, solving for V_{oc} the open circuit condition gives,

$$V_{oc} = \frac{Q_{sc}}{C(x)} \tag{38}$$

In the two-capacitor model, the only capacitance which is dependent on x is $C_1(x)$. The highest Q_{sc} that can be achieved in a TENG is when the charge at the electrodes matches the charge measured at the dielectrics $A\sigma$. This means that,

$$V_{oc} = \frac{A\sigma}{C_1(x)} \tag{39}$$

As the expression for V_{oc} in terms of A, σ, and $C_1(x)$.

The two-capacitor model features two capacitance values in series, therefore the equivalent capacitance can be expressed using Kirchoff's law as,

$$C(x) = \frac{C_1(x)C_2}{C_1(x) + C_2} \tag{40}$$

The short circuit charge Q_{sc} can be expressed as,

$$Q_{sc} = V_{oc}C(x)$$

Substituting the expressions equations 36 and 37 into the expression for Q_{sc} gives,

$$Q_{sc} = \frac{A\sigma C_2}{C_1(x) + C_2} \tag{41}$$

Similarly, the expression for V'

$$V' = \frac{Q_{sc}}{C_2} = \frac{A\sigma C_2}{(C_1(x) + C_2)C_2} = \frac{A\sigma}{C_1(x) + C_2} \tag{42}$$

Equations 39, 40, 41, and 42 can be substituted into equation 37,

$$\eta = \frac{\frac{1}{2}\left(\frac{A\sigma C_2}{C_1(x) + C_2}\right)\left(\frac{A\sigma}{C_1(x)} + \frac{A\sigma}{C_1(x) + C_2}\right)}{\left(\frac{1}{2}\frac{(A\sigma)^2}{C_1(x)}\right)}$$

Expanding the terms and cross multiplying to get a common denominator gives,

$$\eta = \frac{\left(\frac{A\sigma}{C_1(x_{max})}\right)^2\left(\frac{C_1(x_{max})C_2}{C_1(x_{max}) + C_2}\right) + \left(\frac{A\sigma}{C_1(x_{max}) + C_2}\right)^2 C_2}{\left(\frac{(A\sigma)^2}{C_1(x_{max})}\right)}$$

This simplifies to,

$$\eta = \frac{C_2}{C_1(x_{max}) + C_2} + \frac{C_1(x_{max})C_2}{(C_1(x_{max}) + C_2)^2} = \frac{C_2(C_1(x_{max}) + C_2) + C_1(x_{max})C_2}{(C_1(x_{max}) + C_2)^2}$$

Now adding and subtracting the denominator on the numerator gives,

$$\eta_o = \frac{(C_1(x_{max}) + C_2)^2 - (C_1(x_{max}) + C_2)^2 + C_2(C_1(x_{max}) + C_2) + C_1(x_{max})C_2}{(C_1(x_{max}) + C_2)^2}$$

To further simplify to,

$$\eta_o = 1 - \frac{(C_1(x_{max}) + C_2)^2 - C_2(C_1(x_{max}) + C_2) - C_1(x_{max})C_2}{(C_1(x_{max}) + C_2)^2}$$

$$\eta_o = 1 - \left(\frac{C_1(x_{max})}{C_1(x_{max}) + C_2}\right)^2 \tag{43}$$

Finally, equations 38 and 40 can be rewritten to solve for $C_1(x_{max})$ and $C_1(x_{max}) + C_2$.

$$C_1(x_{max}) = \frac{A\sigma}{V_{oc}} \tag{44}$$

$$C_1(x_{max}) + C_2 = \frac{A\sigma}{V'} \tag{45}$$

Substituting equations 44 and 45 into equation 43 gives,

$$\eta_o = 1 - \left(\frac{\frac{A\sigma}{V_{oc}}}{\frac{A\sigma}{V'}}\right)^2$$

Which simplifies into the final equation for the efficiency of a VS-TENG.

$$\eta_o = 1 - \left(\frac{V'}{V_{oc}}\right)^2 \tag{44}$$

The efficiency of a VS-TENG is therefore only dependent on V' and V_{oc}. Equation 44 indicates that the cycle efficiency is limited by the minimum voltage state V' attainable during energy extraction. Any non-zero V'corresponds to residual electrostatic energy remaining stored in the system, which cannot be converted into useful electrical work.

4 RESEARCH OBJECTIVES

The research objectives of this document are:

- To develop and experimentally validate a VS-TENG fabricated using CS deposition techniques.
- To investigate the feasibility of using CS for the fabrication of key TENG components, including copper electrodes, a PFA tribonegative layer, and an aluminum tribopositive layer.
- To evaluate and optimize suitable bond coat strategies using Al and Cu feedstock for enabling reliable deposition and adhesion of PFA directly onto copper substrates.
- To investigate the potential of nylon as an alternative tribopositive material to aluminum, with emphasis on adhesion, triboelectric performance, manufacturability, and material sustainability.
- To characterize the electrical performance of the fabricated TENG by measuring open circuit voltage, short circuit current, and short circuit charge.
- To characterize the operational electrical performance by measuring voltage, current, charge, and power output under varying operating conditions.
- To evaluate energy conversion efficiency and operating feasibility through comparison of experimental results with existing literature.
- To analyze TENG operation using a thermodynamic cycle analogy representing energy harvesting through open- and closed-circuit states.
- To identify key parameters influencing energy harvesting efficiency, including material properties, contact area, and separation distance, and to propose design recommendations aimed at improving performance and enabling practical energy harvesting applications.
- To propose directions for future work, including potential improvements in material selection, device architecture, and experimental methodologies for enhancing VS-TENG performance.

5 EXPERIMENTAL PROCEDURE

5.1 Powder materials and substrates

The powders selected for this study were intended to be used as tribopositive and tribonegative materials for the VS-TENG. From literature review and the governing equations, materials with a high electron affinity and electronegativity demonstrate themselves as ideal candidates for tribonegative materials. Perfluoroalkoxy Alkane (PFA) is a fluoropolymer commonly used in hydrophobic coating applications and in this study as the main tribonegative material. A common issue faced when spraying polymer powders are interparticle cohesive forces and Van der Waals forces influenced by their chemical structures. If there is cohesive attraction between particles this can result in the formation of aggregates prior to powder injection or during flight and influence the particle feeding and particle velocity, affecting the overall deposition. The PFA powder used here (PFA) (FLUON® EA-2000 PW50, AGC Chemicals America Inc, PA, USA) displays an irregular morphology with a flakey geometry with a particle size ranging from 20 to 50 μm. It is shown under SEM in Figure 39.

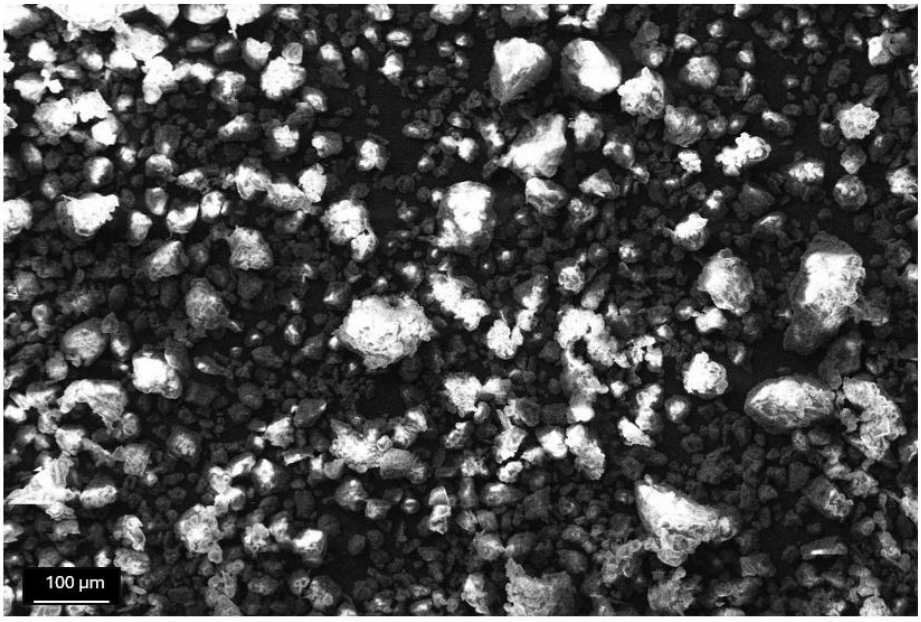

Figure 39: PFA feedstock powder morphology

It is a highly electronegative fluoropolymer developed as a competitor to the commonly available PTFE (Teflon®). The powder itself has an overall irregular morphology with

flake like geometries. Unlike other polymer powders such as Nylon 6 that suffer from aggregate formation and demonstrate feeding challenges, the PFA feedstock does not display this behaviour because of the modifications in the chemical composition of the powder, allowing for the powder to be largely unaffected by any cohesion, making it an appealing powder to investigate in Cold Spray (CS).

A commercially available aluminum (Al) feedstock powder (SST-A5001, Centerline Limited, Windsor, Canada) with an irregular morphology particle size distribution between 5 and 45 µm was selected as the positive dielectric material. The CS deposition of Al is well documented, and the material is positioned on the donor side of the triboelectric series, making it an appealing material selection for a successful proof of concept design. The Al feedstock is shown below in Figure 40.

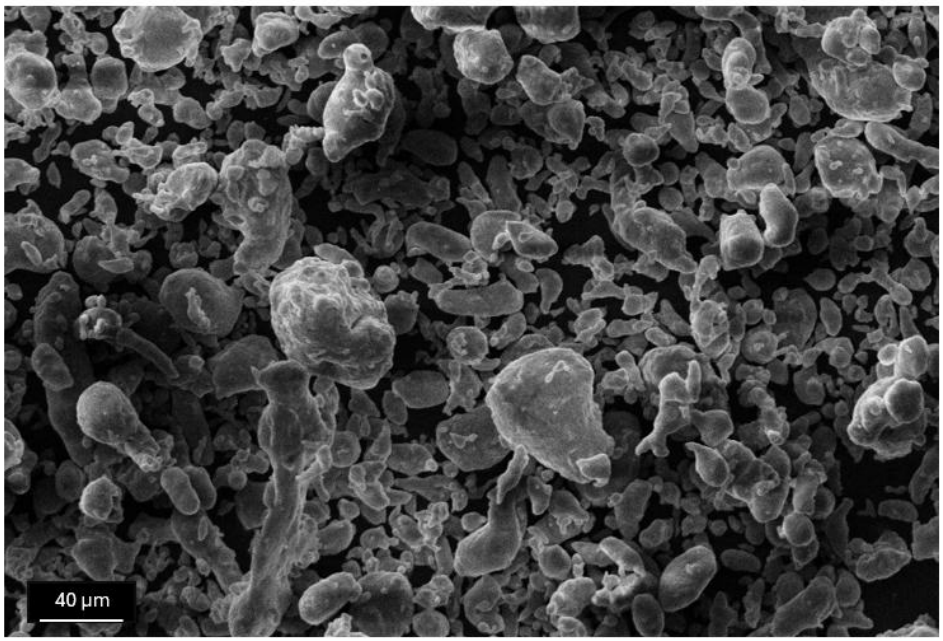

Figure 40: Al feedstock powder morphology

Along with the use of Al for the positive dielectric layer, a Nylon 6 powder (Goodfellow, UK) with a particle size between 15 to 35 µm was also investigated for potential use as a tribopositive material. Nylon is positioned above Al on the triboelectric series, meaning that if a successful coating of Nylon 6 is deposited and paired with the highly electronegative PFA, there would be an increase in electron transfer resulting in a stronger

electric field which should theoretically increase the electrical performance. The Nylon feedstock is shown below in Figure 41.

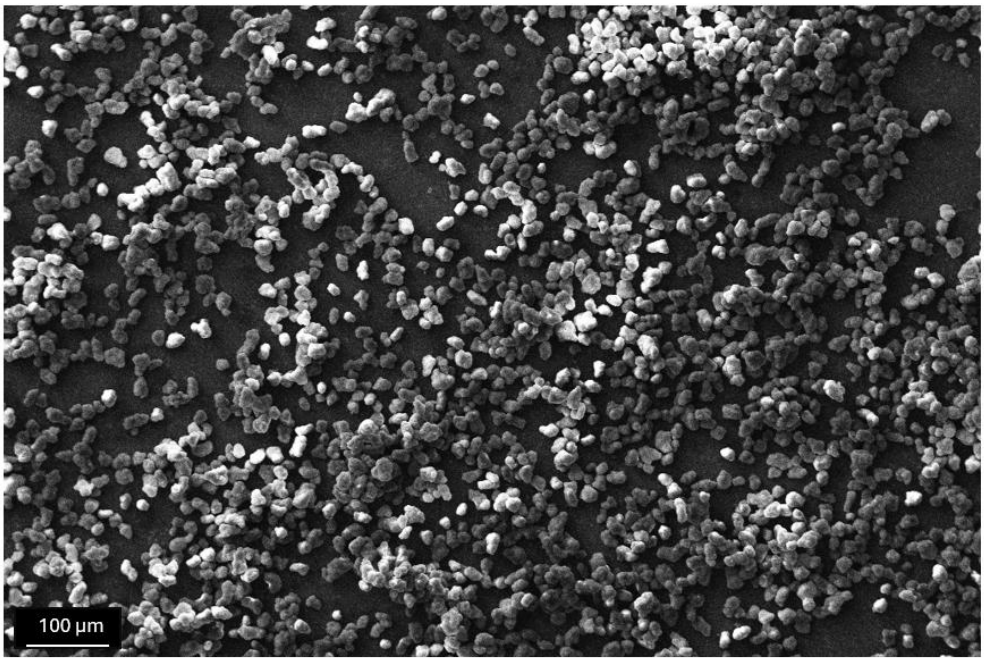

Figure 41: Nylon feedstock powder morphology

A Copper (Cu) 110 plate (Metal Pros, Ottawa, Canada) with a thickness of 0.406 mm was selected as the substrate material and subsequent electrode. A thin substrate was necessary to minimize internal resistance within the electrodes. Since spraying PFA onto copper had not been previously attempted, several surface preparation methods were evaluated to ensure adequate adhesion.

Initial attempts involved grit blasting the copper substrate using ferrosilicate grit (16 mesh – 20 grit) (AG, Ruemelin Manufacturing Company, Milwaukee, WI, USA). However, this method caused excessive bowing of the thin Cu plates, compromising their flat geometry. This deformation affected coating accuracy and reproducibility and hindered full contact between the dielectric layers during TENG operation. Additionally, grit blasting did not provide sufficient surface roughness for effective mechanical interlocking of the PFA powder.

To address these limitations, a copper coating was sprayed onto the as received Cu substrate as an alternative surface preparation method. This approach increased the surface roughness without deforming the substrate.

Given that polymer powders such as PFA require mechanical interlock for successful deposition, CS coatings of Cu and Al were evaluated as bond coats on the Cu substrate. The copper powder used (SST-C5001, CenterLine Ltd., Windsor, Canada) had a particle size distribution between 5 to 45 µm and a dendritic morphology. Previous studies have demonstrated successful cold spray deposition of PFA on aluminum substrates. Therefore, an initial aluminum bond coat was used to establish a proof of concept before transitioning to copper as the bond coat material for the PFA layer. Its morphology is shown below in Figure 42.

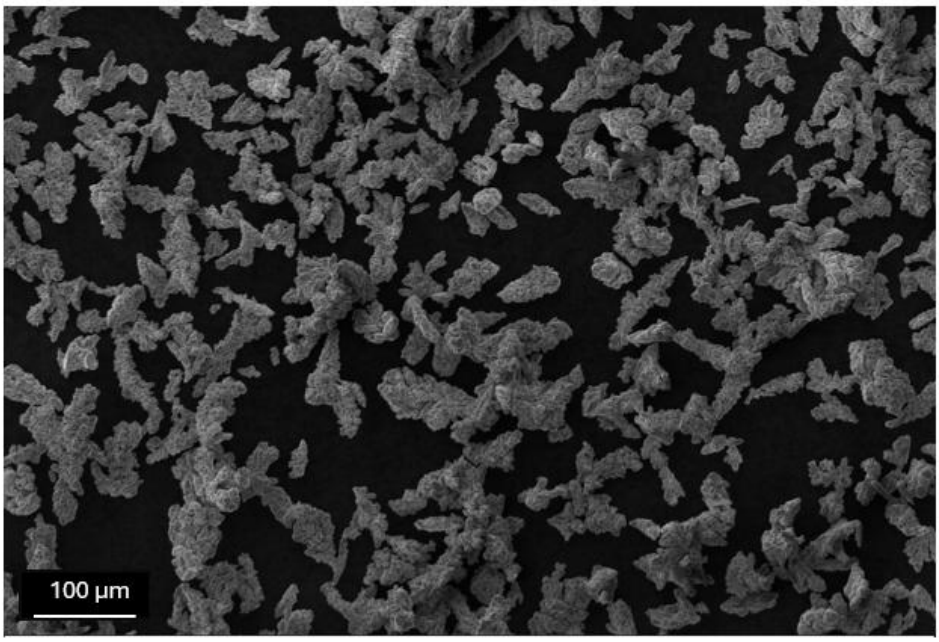

Figure 42: Cu feedstock morphology

5.2 Cold Spray System

5.2.1 Gas Heater, Pressure Regulator, and Control Unit

A commercially available CS system (SST EP, Centerline Ltd, Windsor, On, Canada) was used. It uses a 15 kW three coiled three phased AC electric gas heater which can reach an operating stagnation temperature and pressure of 650 °C and 3.4 MPa respectively. The stagnation conditions for CS are found ahead of the converging diverging section of a CS

nozzle where the gas can be assumed to be stagnant. The gas heater is mounted on a robotic traverse system powered using a series of linear motors and actuators. The stagnation temperature is controlled directly on a touch screen which comes with the SST EP, and the stagnation pressure is adjusted using a pressure regulator connected to a gas bulk back. The control unit and gas heater are shown below in Figure 43a and 43b.

Figure 43: a) CS control unit b) Gas heater with nozzle attached

5.2.2 Powder Feeding Equipment

The feedstock powders were fed using a commercially available powder feeder (AT-1200HP, Thermach Inc., Appleton, Wisconsin, USA) shown in Figure 39a. The feedstock is contained inside of a pressurized canister and is fed into a feeding line directed towards the spray gun via a rotating wheel with holes perforated around its circumference. The rate at which powder is fed can be controlled by changing the rotational speed of the feeding wheel or by changing the size of the holes. The feeder along with an example of a feeder wheel is shown below in Figure 44a and 44b.

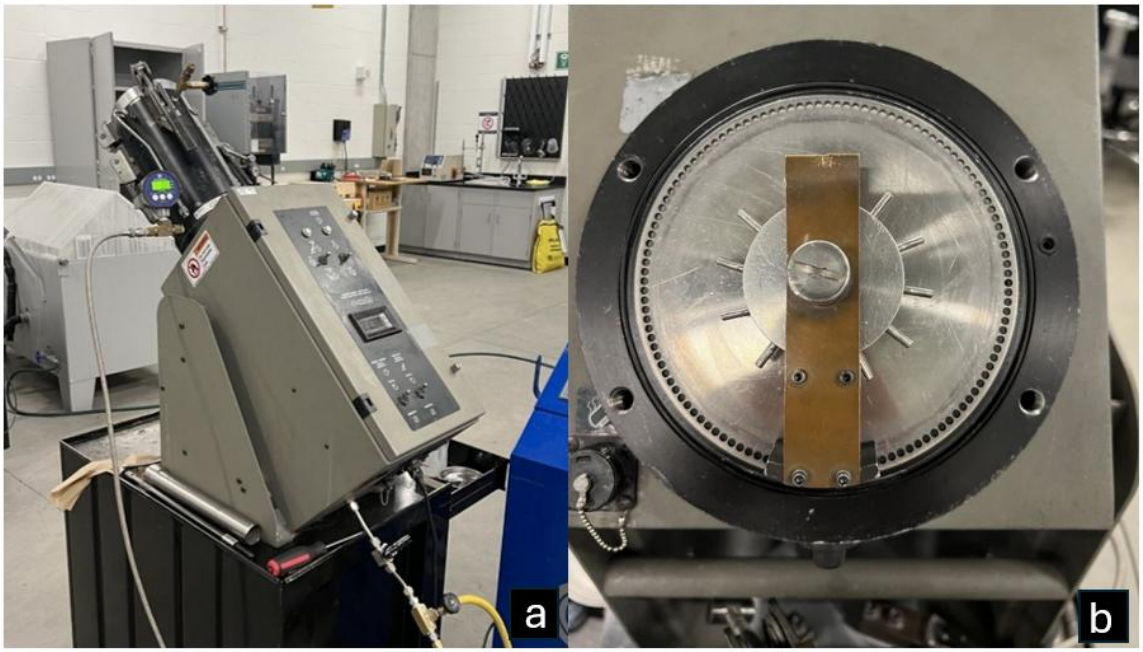

Figure 44: a) Powder Feeder b) Feeder wheel

5.2.3 Spray Chamber and Fan

The spray chamber houses the robotic traverse system, the gas heater, the spray gun, and a moveable stage which can be adjusted in height to satisfy the stand-off distance requirements of the spray. The chamber is also equipped with a hinged door with a plexiglass window to protect the operator(s) during spraying and provide a line of sight during spraying. A fan system provides a suction collecting any excess powder during spraying, preventing powder from evacuating the chamber. Both the Spray Chamber and Fan systems are showed in Figure 45.

Figure 45: Spraying chamber and Fan system

5.2.4 Substrate Pre-Heater

For spraying polymers, the mismatch in thermal expansion coefficients between the polymer feedstock and the metallic substrate was accommodated through the use of a strip heater (Omega Environmental, QC, CA) of dimensions 25.4 mm x 200 mm. Localized substrate heating reduces thermal gradients during deposition, thereby limiting differential contraction upon cooling. This approach improves coating adhesion by mitigating residual thermal stresses and reducing the likelihood of interfacial debonding or microcrack formation in the deposited polymer layer. The temperature was controlled by power source operating with a relay system control system (Vishay Instruments Inc, Model BAM1, PA, USA). Both the strip heater and power source are shown below in Figure 46a and 46b.

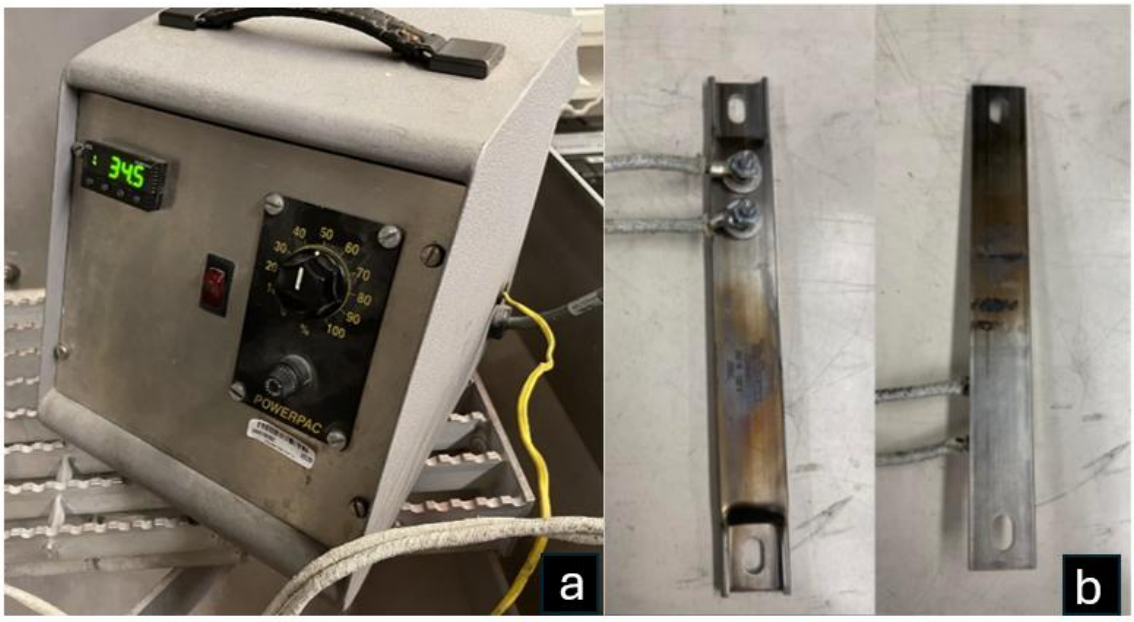

Figure 46: a) Power source b) Strip heater

5.2.5 Nozzle Assemblies and Geometries

Three different nozzles with different geometries were used and are presented in this section; a steel nozzle, a polymer nozzle, and a novel straight section nozzle described below. Different nozzles were used to accommodate for the differences of the nature of different feedstock powders.

5.2.5.1 Steel Nozzle

The steel nozzle assembly is constructed from four components. A powder inlet angled at 45 degrees is built into the diverging area of a converging diverging section, which is mated to a 120 mm diverging section with an exit diameter of 6.6 mm using a nozzle holder and a collet. It has a throat diameter of 2 mm and it is shown in its full assembly below in Figure 47. This nozzle is used for the deposition of the Cu feedstock.

Figure 47: Steel nozzle assembly

A steel nozzle was used for copper spraying due to the higher density and erosive behavior of copper particles during cold spray processing. The greater mechanical strength and wear resistance of steel help maintain nozzle dimensional stability and consistent particle acceleration throughout deposition.

5.2.5.2 Polymer Nozzle

The polymer nozzle, shown in Figure 48 is used to deposit Al feedstock. As with the steel nozzle, the converging diverging sections is one assembly. The main difference is the powder injection is connected directly to a hole in the diverging section at 90 degrees and is screwed in tightly and held in place using two nuts**.** The nozzle holder consists of two pieces and a spring, which when assembled acts as a fastener keeping the diverging section in place. This nozzle has a throat diameter of 2 mm, a diverging section length of 120 mm, and an exit diameter of 6.35 mm, respectively.

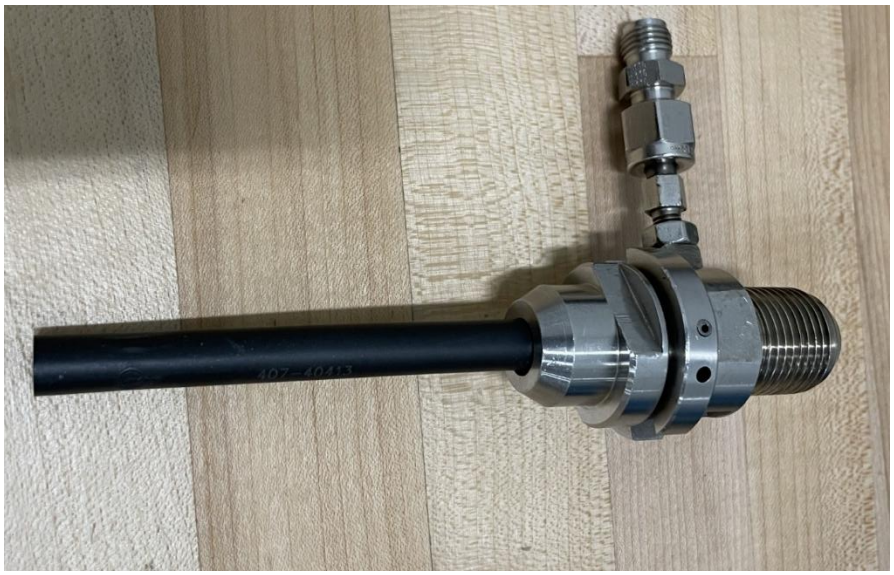

Figure 48: Polymer nozzle assembly

A polymer nozzle was used for aluminum spraying since aluminum particles are relatively soft and ductile, resulting in lower erosive wear during cold spray deposition. Polymer nozzles also help reduce particle adhesion and buildup within the nozzle, improving powder flow stability and reducing clogging during spraying.

5.2.5.3 Straight Section Nozzle

The straight section nozzle is made of stainless steel, and is constructed from three main components: the powder injector, the converging gas inlet, and a straight section nozzle extension with a 151.5 mm length and a diameter of 4 mm. This nozzle was specifically developed using CFD modelling for the deposition of PFA feedstock by Leclerc et al for the CS manufacturing of ice phobic coatings [118]. The reasoning for this nozzle is explained in section 5.2.6. The powder injection assembly shown in Figure 49 consists of a powder inlet connected to the powder feeding line, and a powder outlet which consists of a 3.175 mm copper wire angled downward at a 45-degree angle. The powder injector along with the full nozzle and injector assembly is shown below in Figure 50.

Figure 49: Powder injector

Figure 50: Straight section nozzle with injector attached

5.2.6 Cold Spray Set-up

When spraying using a conventional converging diverging (de Laval) nozzle with the SST-EP system, gas flow from a bulk pack is split into two streams, with one stream directed to the powder feeder and the other stream to the spray gun. Before entering the feeder, the gas flow enters a flow meter and pressure regulator, which restricts the flow to 40 psi. Regulating to higher flow rates by twisting the knob will further reduce the pressure of the flow. The Conventional CS system is illustrated below in a schematic in Figure 51.

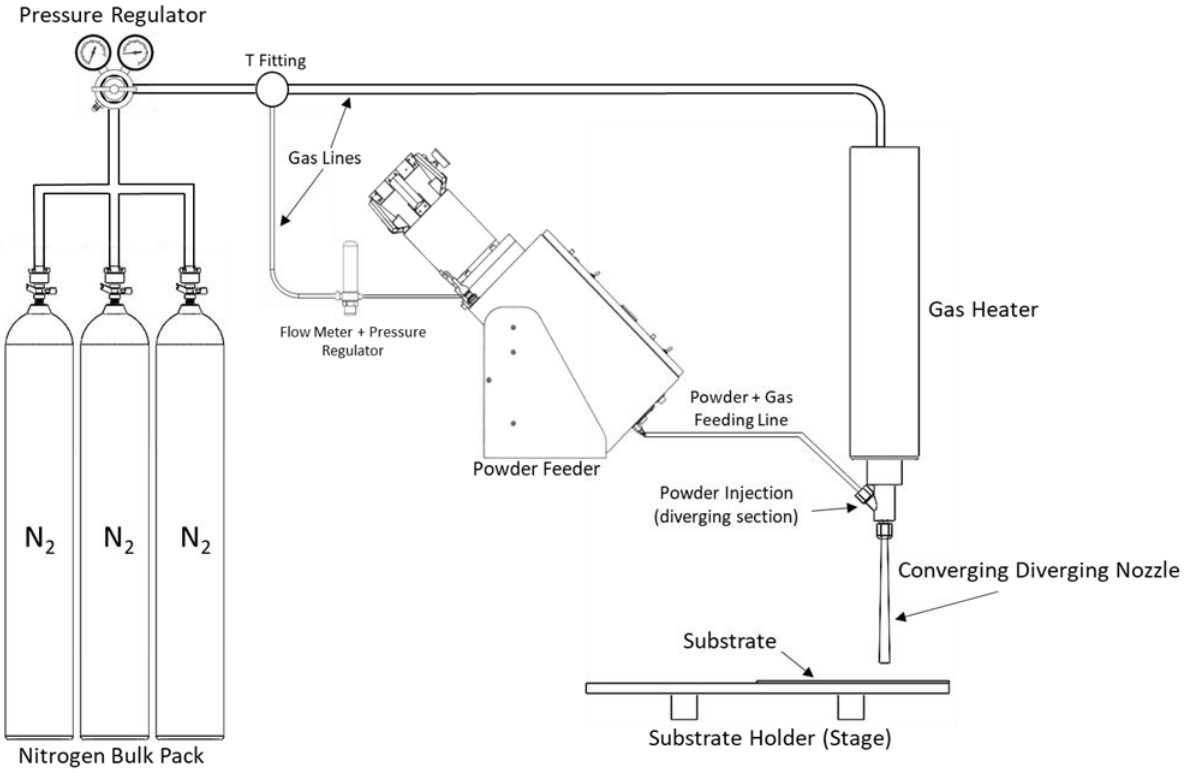

Figure 51: Conventional CS schematic

The low pressure at the powder injector is not an issue with a de Laval nozzle as the powder is injected at the diverging section of the nozzle, where the relative pressure is very low because of the high kinetic energy of the flow. When spraying PFA, higher stagnation pressures lead to high gas velocities, and introducing PFA particles to this flow excessively accelerates them. Using the lowest operating pressure of the SST-EP of 60 psi and making use of a straight section nozzle is shown to slow down the particle flow to subsonic speeds. The slowed down gas stream also prevents high Mach numbers at the nozzle exit which would create large shockwaves ahead of the substrate, considerably slowing down the light PFA particles which carry little momentum. A straight section nozzle is therefore used for two purposes: 1) decreased particle acceleration compared to a de Laval nozzle preventing high Mach numbers at the nozzle exit which create large shockwaves and 2) increased travel time allowing the PFA particles to reach a higher temperature.

The CS set-up for PFA and Nylon 6 powders requires different considerations compared to the commonly sprayed metal powders. As characteristics, polymers have high specific heats and low thermal conductivities, therefore a longer nozzle travel time is required to

energize the particles to produce a dense coating. Another major challenge with polymers in general is how light the powders are. This makes them easily affected by disturbances in the flow such shockwaves and are quick to accelerate or decelerate.

An issue faced when using the straight section nozzle with the conventional setup of the SST-EP is that by design, the pressure of the powder injection is much lower than the pressure of the main gas stream, making it impossible for powder to be injected into the main flow. To remedy this, an additional nitrogen bottle is used and set to the same stagnation pressure of the main flow. This arrangement equalizes the pressure differential at the injection point, stabilizes powder delivery, and enables reliable feeding of low-density polymer particles into the primary jet. A pressure regulator is connected to this auxiliary nitrogen bottle and set to 60 psi. The flow is then passed through a rotameter flow meter as shown in Figure 52a and 52b and this gas stream enters the powder feeder.

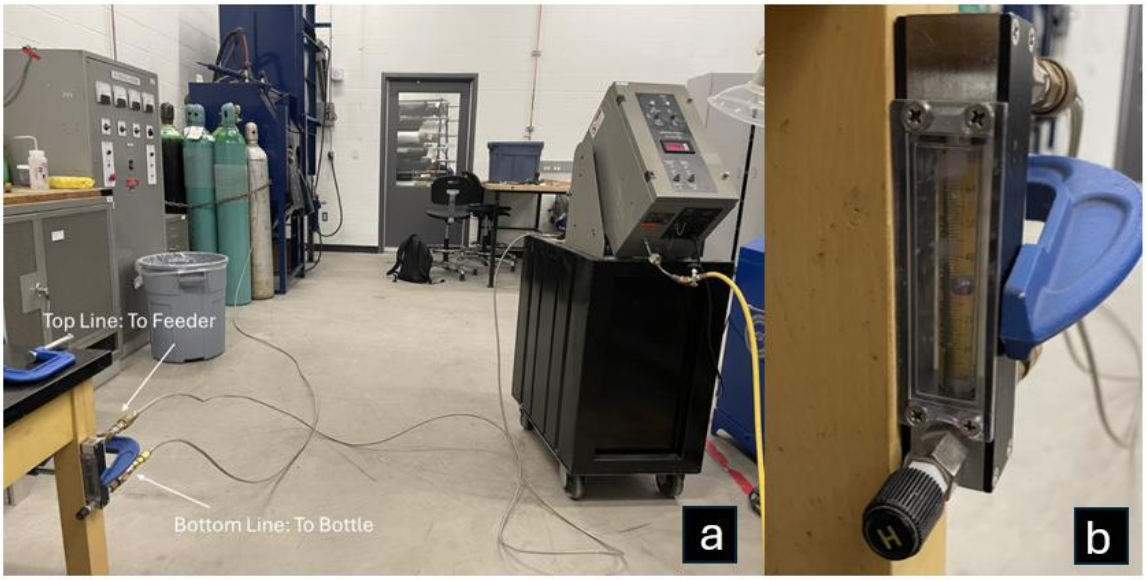

Figure 52: a) Auxiliary gas stream b) Rotameter

Once the rotameter is set to a flow rate within the range of 30-40 SCFH, the pressure gauge on the canister should read roughly around 43 psi. A schematic of the PFA CS set up is shown below in Figure 53. This alteration allows PFA powder to be injected into the main gas stream.

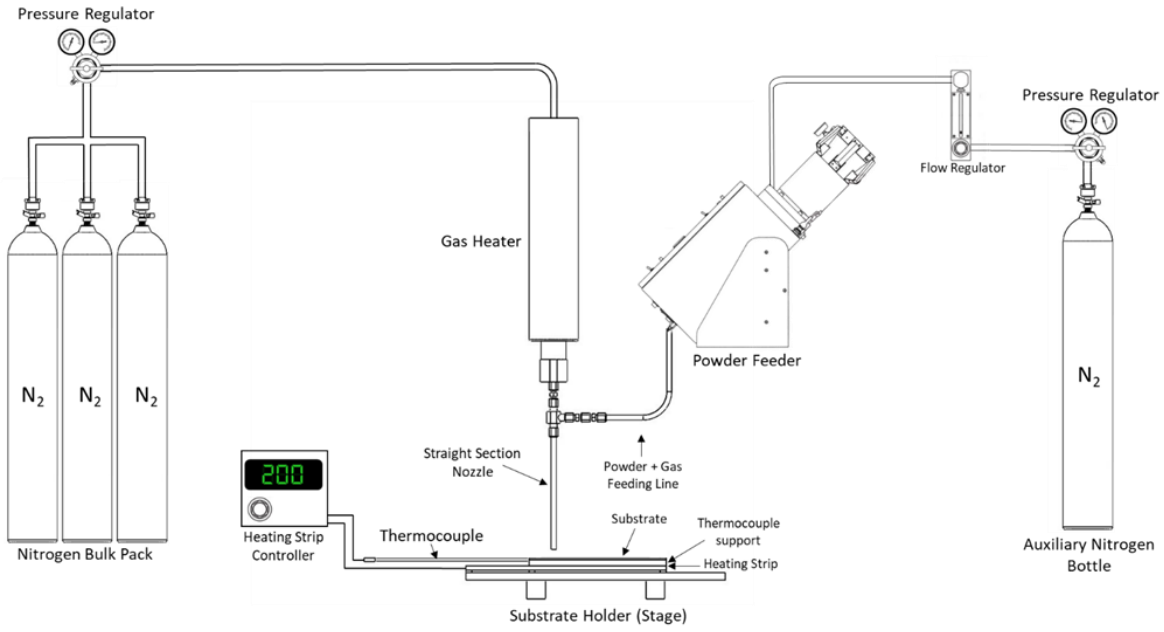

Figure 53: PFA CS setup

Substrate preheating is necessary when making CS coatings of polymers as there is a significant difference in the thermal expansion coefficients of the polymers and metal substrates. Bringing the substrate up to temperature corrects for this difference. The coefficient of thermal expansion of copper which of $16 \times 10^{-6}\,\mathrm{K}^{-1}$ is an order of magnitude lower than that of PFA which is $20 \times 10^{-7}\,\mathrm{K}^{-1}$. In polymer CS deposition, this mismatch can lead to large residual stresses during cooling, as the polymer contracts more rapidly than the metallic substrate. Substrate preheating reduces thermal gradients at the coating–substrate interface and decreases the magnitude of differential contraction after deposition. As a result, residual stresses are reduced, leading to improved coating integrity and adhesion. The strip heater controlled by a thermocouple inserted into a copper support is used to preheat the substrate to 200 ºC prior to spraying. For copper substrates, a temperature of 150 ºC can also be used. When using a strip heater, ceramic blocks are used as insulation, preventing the stage or clamps from becoming heat sinks, ensuring that substrate temperature is maintained. The entire assembly showing the substrate, thermocouple support, thermocouple, ceramic isolation, and heating strip along with an exploded schematic is shown in Figures 54 and 55.

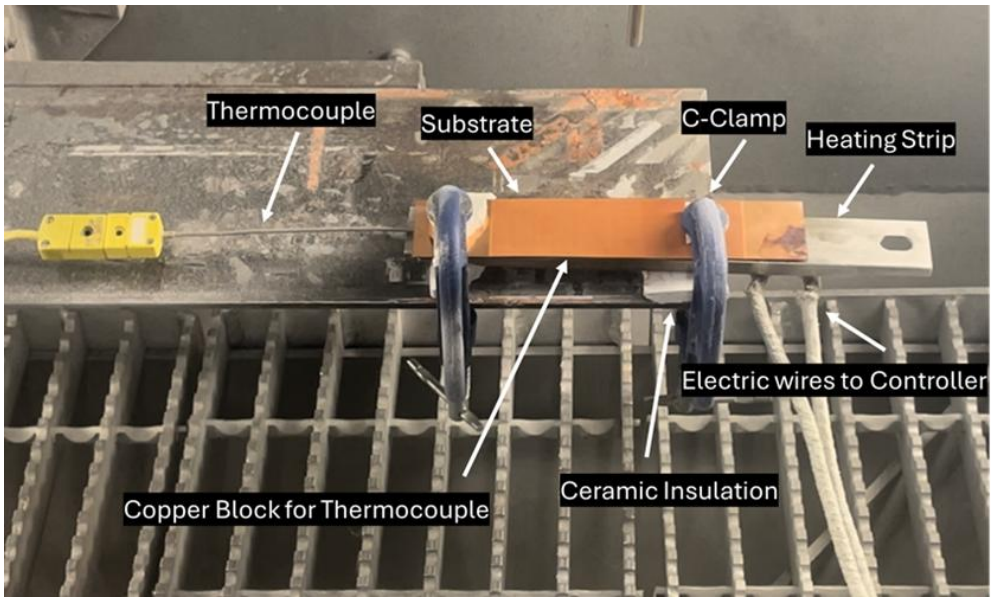

Figure 54: substrate preparation for PFA

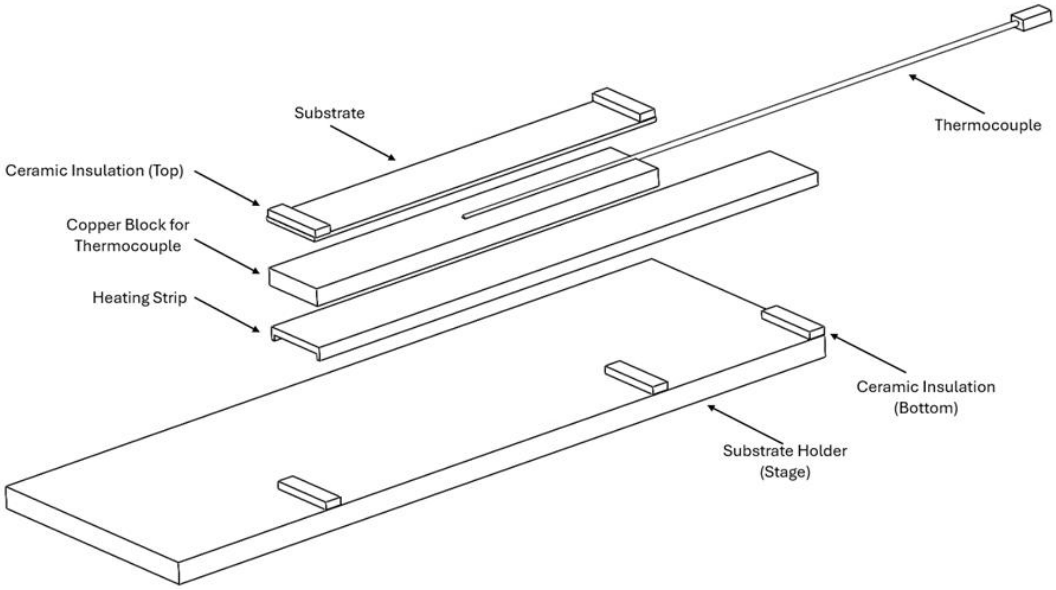

Figure 55: Substrate preparation assembly for PFA spray

5.3 Coating Characterization and Analysis Equipment

5.3.1 Sample Post-Processing

The post-processing of samples begins with the use of a thin silicon carbide wheel mounted to a precision saw (Secotom-10, Struers, Mississauga, CA) to cut samples to an appropriate size for further inspection. This saw was also used to prepare squares which would subsequently be used as the positive and negative dielectrics for the VS-TENG. Based on

material properties, the samples to be inspected can be mounted using a hot mounting system, where plastic pellets melt around the sample in a hot press (LaboPress-3, Struers, Mississauga, CA). However, materials with a melting temperature lower than the melting temperature of the plastic pellets cannot be placed in the press. As an alternative, they are mounted inside an epoxy resin by hand and left to harden overnight. For cross sectional coating views, a grinding/polishing procedure using a sample polishing machine (Tegrapol, Struers, Mississauga, CA) is used to obtain a scratch free, mirror like finish. The equipment used is shown below in Figure 56a and 56b.

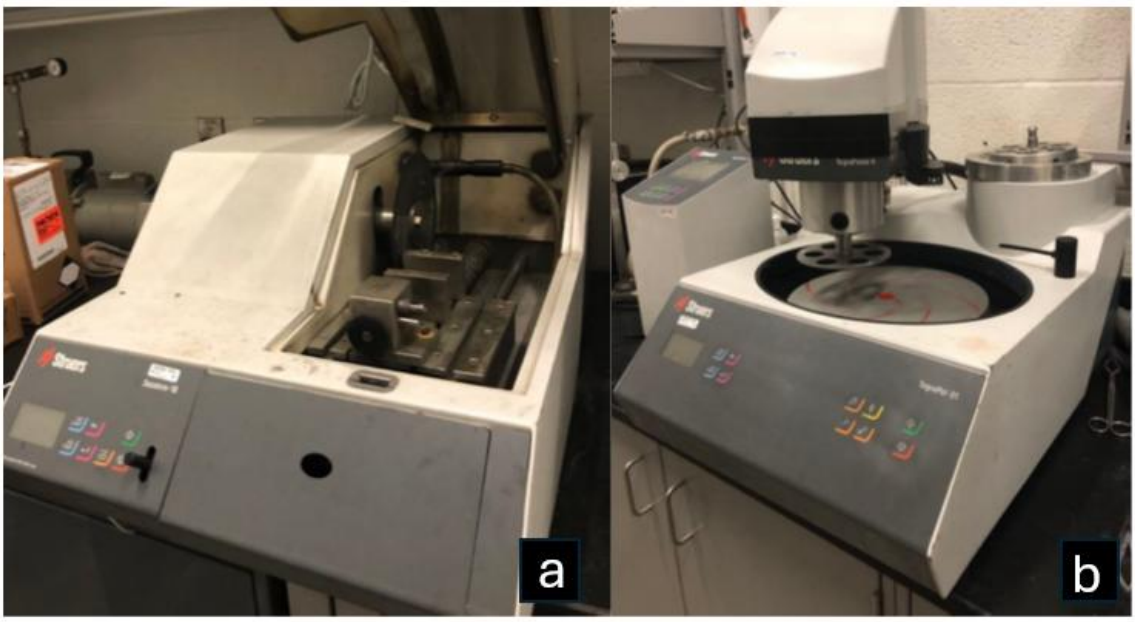

Figure 56: a) Saw b) Sample polishing machine

5.3.2 Scanning Electron Microscope

A scanning electron microscope (EVO-MA10, Zeiss, Germany) is used to examine the particle morphology, sample cross sections, and surface topography of the coatings. A secondary electron and back-scattered electron signal can be used to visualize the coating characteristics. Samples were gold sputtered in a vacuum (Denton Vacuum, USA) to turn a non-conductive surface conductive. Samples were either sputtered after electrical testing to view coating degradation, and as-sprayed samples were not used in VS-TENG applications. Additionally, coating thicknesses were measured by taking multiple measurements along the sample cross sections. A photo of the EVO-MA10 and Denton Vacuum are shown below in 57a and 57b.

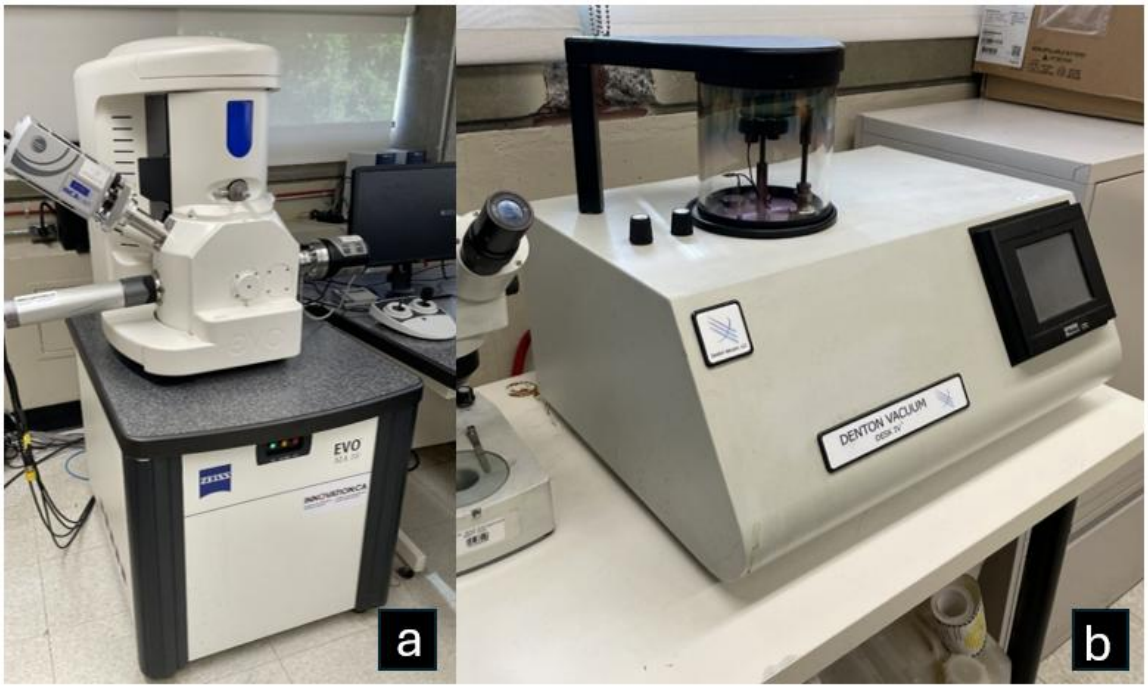

Figure 57: a) Scanning electron microscope b) Gold sputtering machine

5.3.3 Surface Roughness Measurements

The surface measurements of coatings were determined with a profilometer (SRG-4000, Phase II Plus, NJ, USA) which came equipped with a diamond stylus. The roughness of the substrates and coatings were analyzed over a length of 17.5 mm. Surface roughness can be measured from 0.005 to 16 µm using the profilometer.

5.4 Triboelectric Generators and Electrical Testing Equipment

5.4.1 Triboelectric Generator Configurations

Two triboelectric nanogenerator (TENG) designs were investigated to explore material compatibility and performance. Both designs are illustrated below in Figure 58.

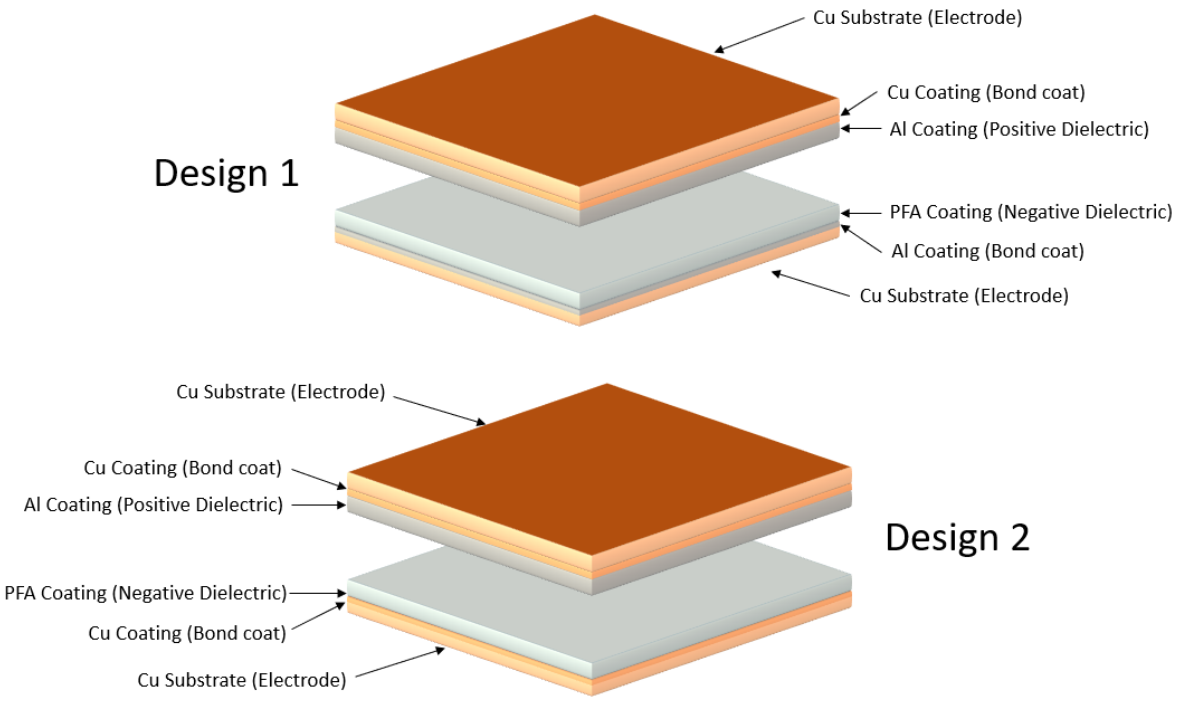

Figure 58: VS-TENG design configurations

The first design utilized a polytetrafluoroethylene (PFA) coating as the negative dielectric layer, deposited onto an aluminum coating. The aluminum layer, acting as the positive dielectric on one layer and as a bond coat for the PFA, was first sprayed onto a copper substrate, which also served as the electrode for the TENG. This configuration was chosen as a proof-of-concept because prior work demonstrated the successful deposition of PFA onto aluminum surfaces using the cold spray process. The positive dielectric layer for this design was fabricated by directly spraying an aluminum coating onto a separate copper electrode, which was prepared by spraying Cu powder as a bond coat. This was used as the exceptionally thin substrate made conventional surface roughening through grit blasting techniques impossible. After spraying, the samples were then cut into 31.75 mm x 31.75 mm squares for use as VS-TENGs.

The second design expanded on this approach by replacing the aluminum bond coat with a copper coating for the PFA layer. This modification aimed to assess the viability of copper as an alternative bond coat material and its influence on the triboelectric properties of the TENG, along with eliminating any electrical side effects the Al may have had. The positive

dielectric configuration remained unchanged, consisting of an aluminum coating on a copper electrode.

The bond coats and triboelectric coatings were sprayed as thin as possible while maintaining complete and dense surface coverage by adjusting the traverse speed and step sizes. This is important for VS-TENG performance because increasing the dielectric thicknesses d_1 and d_2 reduces the effective electric field and lowers the electrostatic induction between the triboelectric surfaces. Thinner dielectric layers help maximize the capacitance. Additionally, minimizing the thickness of metallic bond coats (Al and Cu) reduces the electrical resistance within the conductive layers. Excessively thick coatings may introduce additional voltage drops which reduce the overall electrical performance of the VS-TENG.

Instron Universal Testing Machine

The mechanical displacement of the TENG was performed using an Instron 8801 Universal Testing Machine, shown in Figure 59.

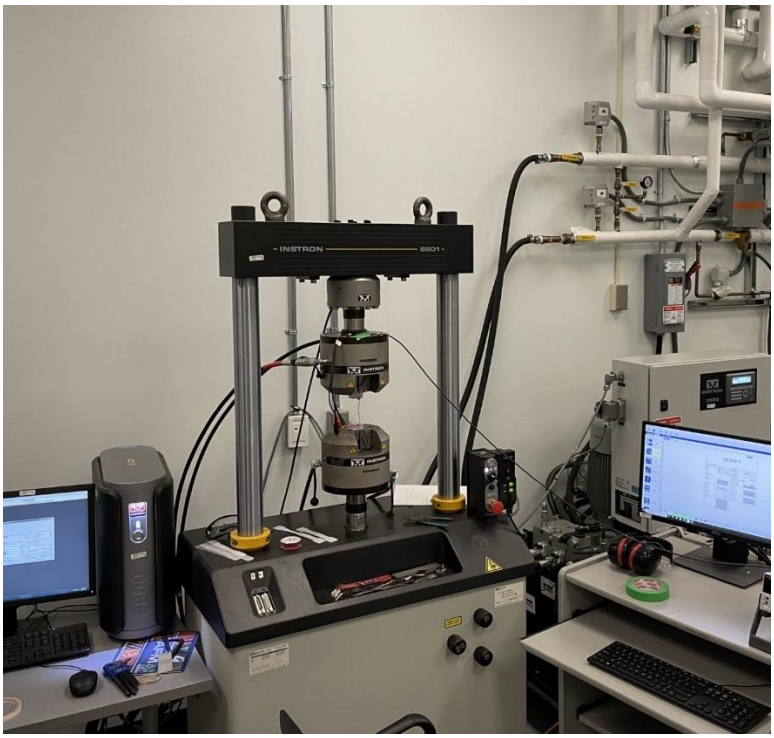

Figure 59: Instron 8801 testing machine

Although commonly used for mechanical property testing such as tensile or compression analysis, in this work, this testing equipment was used for its precise control over displacement and cyclic loading, enabling repeatable vertical contact-separation motions controlling impact speed and frequency. The ability to accurately program oscillation frequency and amplitude was necessary for simulating realistic and consistent operating conditions over extended cycling periods.

Each TENG layer was mounted onto custom polyurethane (PU) supports using super glue, which were then fixed onto the moving and stationary platforms of the Instron system. The machine was programmed to apply periodic vertical oscillations ranging in frequency from 1 to 10 Hz, enabling controlled contact and separation between the tribonegative and tribopositive layers. To determine a consistent and practical separation distance for voltage measurements, the separation distance was gradually increased while monitoring the measured open-circuit voltage. Although theoretical models predict that V_{oc}increases with separation distance under ideal open-circuit conditions, the experimentally measured voltage reaches a peak and subsequently decreased due to non-ideal measurement effects, including finite load resistance and parasitic losses. The separation distance corresponding to the maximum measured voltage was therefore selected and used for all subsequent experiments to ensure repeatable and reliable measurements.

This setup ensured uniform contact pressure and displacement across all samples allowing for repeatability, thus providing consistent mechanical input during performance testing. The automated nature of the Instron 8801 allowed for long-term cycling without user intervention, and all TENGs were then subjected to 6,000 continuous contact-separation cycles to evaluate coating durability and electrical output over time. A TENG mounted to the Instron is shown below in Figure 60.

Figure 60: TENG mounted to Instron machine

5.4.2 Electrical Data Collection

The electrical characterization of the TENG devices was conducted using a Keithley 6517B electrometer, selected for its high input impedance and low current measurement capability, which are necessary for accurately capturing the small signals generated during TENG operation. The electrometer, shown in Figure 61. was used to quantify the main triboelectric performance parameters, including open-circuit voltage (V_{oc}), short-circuit current (I_{sc}), and transferred charge (Q_{sc}). Data collection took place in a controlled laboratory, where humidity levels did not vary between sample collection dates.

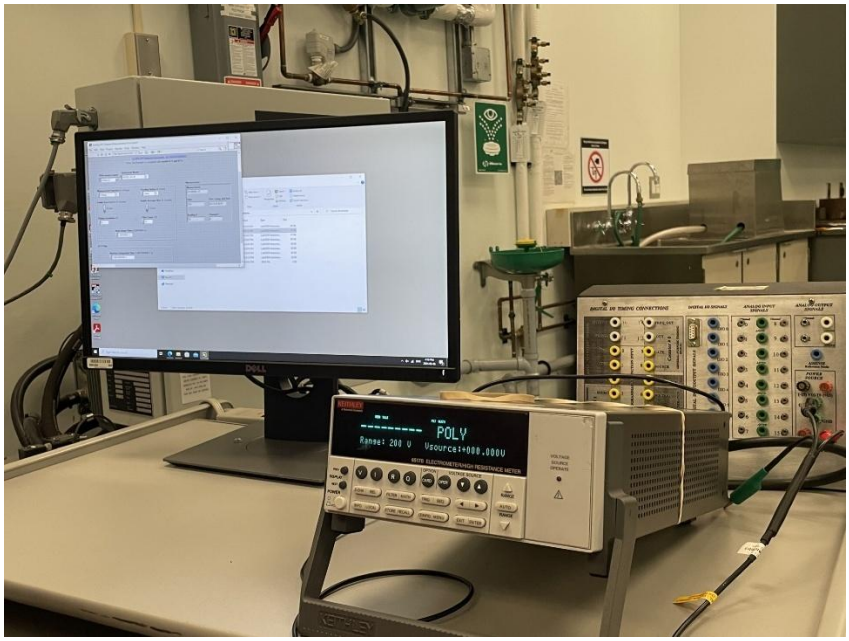

Figure 61: Kiethley 6517B electrometer

For measuring V_{oc}, the TENG was connected directly to the electrometer as shown in Figure 62. The high load impedance of the electrometer allowed for an accurate measurement of V_{oc} under the assumption of $Q = 0$.

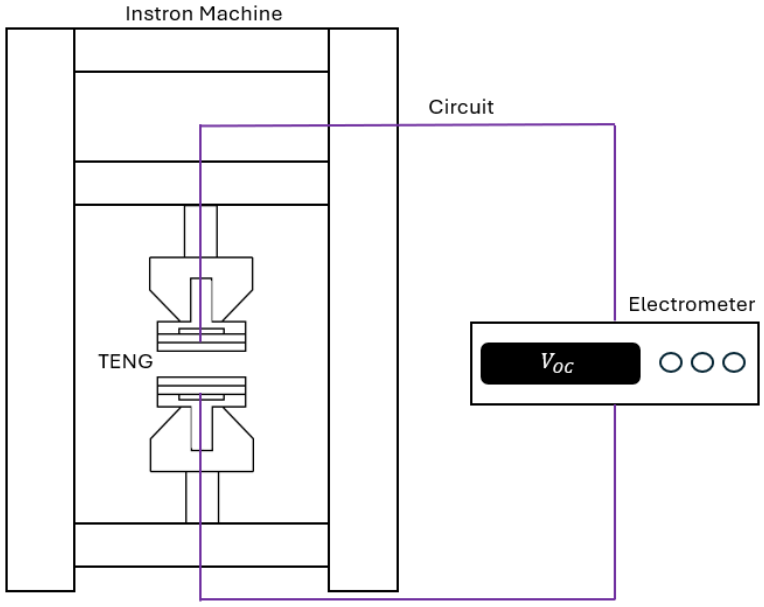

Figure 62: TENG Testing layout for V_{oc}

For determining Q_{sc} and I_{sc}, the two electrodes of the TENG were connected through a parallel external circuit, as shown in Figure 63, providing a low-impedance path for charge

transfer and enforcing the short-circuit condition ($V = 0$). The electrometer, configured for charge and current measurements, possesses a high input impedance that minimizes measurement loading effects while allowing for accurate measurements.

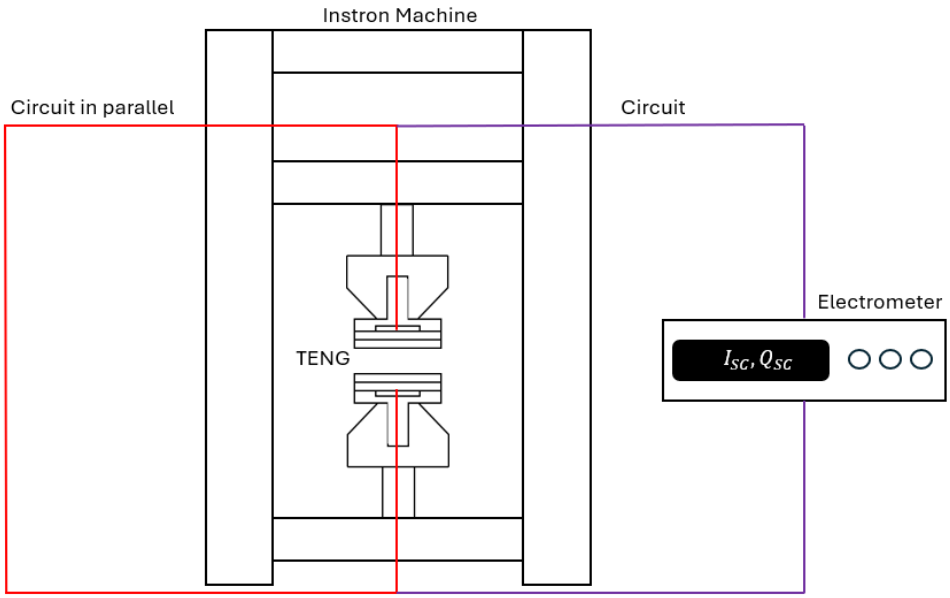

Figure 63: TENG testing layout for Q_{sc} and I_{sc}.

To characterize the voltage V, and current I under more realistic operating conditions, along with power and peak power output, external resistors ranging from 10 to 200 Megaohms were attached and exchanged to identify the location of peak performance. The configuration formed a parallel circuit as shown in Figure 64, with the high load impedance from the electrometer ensuring no interference and accurate measurement.

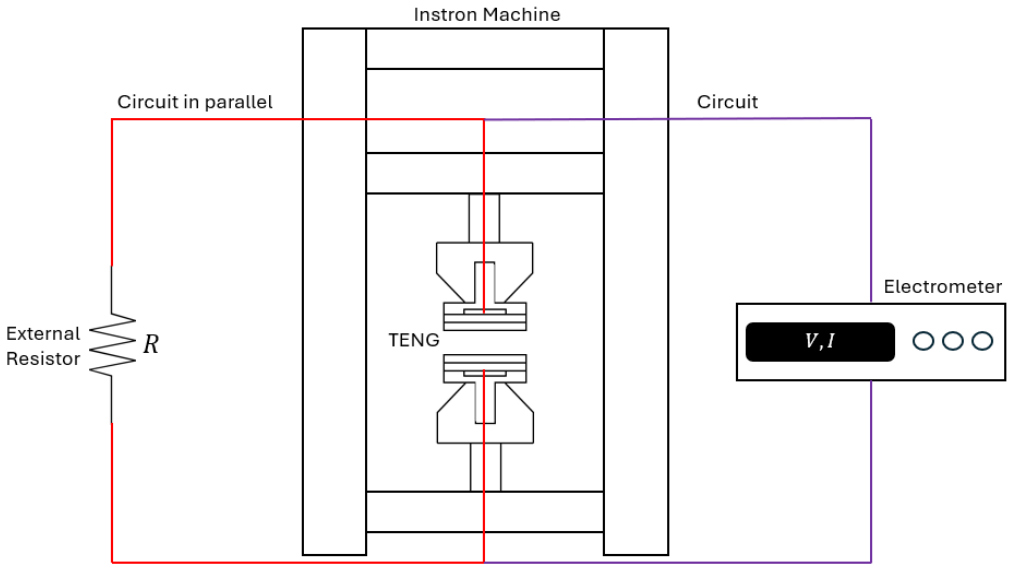

Figure 64: TENG testing layout

Electrical leads were soldered to the copper electrodes of each TENG and connected directly to the electrometer. A LabVIEW-based data acquisition program interfaced with the electrometer via a dedicated driver, enabling automated, real-time data collection throughout the cycling process. Although the electrometer was not calibrated prior to use, it was operated under standard manufacturer settings appropriate for triboelectric measurements.

Data collected corresponded to the contact-separation cycles imposed by the Instron machine. These measurements formed the basis for evaluating the electrical performance and stability of each TENG configuration over repeated operation.

6 RESULTS AND DISCUSSION

This chapter presents the results and discussion for the two TENG designs fabricated. The first design utilized a Cu-Al configuration for the tribopositive layer and a Cu-Al-PFA configuration for the tribonegative layer. In the second design, the tribopositive layer remained unchanged, while the tribonegative layer replaced the aluminum bond coat with copper, resulting in a Cu-Cu-PFA structure. The coatings and corresponding electrical outputs for both designs are presented and discussed in detail. Additionally, an attempt to

deposit a Nylon-based tribonegative layer is included, offering insight into the limitations of certain materials in the CS process.

6.1 Coatings and Characterization

6.1.1 Al Coating

Aluminum has well documented favourable cold spray deposition behavior from previous results. The coating was deposited onto copper substrates using low pressure CS, under parameters optimized for Al adhesion and coating density. Coatings of Al were sprayed for use as a bond coat and a positive dielectric (electron donor). The complete list of spray parameters for the metal powders used is presented in Table 1.

Table 1: CS parameters for metal feedstock

Material	Aluminum	Copper
Powder Geometry	Irregular	Dendritic
Gas Type	Nitrogen	Nitrogen
Stagnation Pressure	500 psi	400 psi
Stagnation Temperature	500 ºC	375 ºC
Stand-off Distance	10 mm	10 mm
Traverse Speed	50 mm/s	150 mm/s
Step Increment	3 mm	3 mm
Number of Passes	10	10
Nozzle Material	Polymer	Steel
Throat Diameter	1.8 mm	2 mm
Nozzle Length	120 mm	120 mm
Exit Diameter	7 mm	6.5 mm

An irregular aluminum powder was deposited using nitrogen as the process gas at a stagnation pressure of 500 psi and a stagnation temperature of 500 °C. The high gas pressure and temperature were selected to maximize particle acceleration and heating prior to impact, ensuring sufficient kinetic energy and deformability of the particles to achieve bonding while maintaining good deposition efficiency. Nitrogen was chosen as the carrier gas due to its inert nature, preventing oxidation of aluminum during flight.

A polymer nozzle was used for aluminum spraying to minimize clogging associated with metallic nozzles. Aluminum particles are relatively soft and, when accelerated at high velocity, can adhere to and clog metallic nozzle surfaces, which may distort the jet profile. The use of a polymer nozzle avoids this effect and ensures process stability.

The stand-off distance of 10 mm, traverse speed of 100 mm/s, step increment of 3 mm, and 10 total passes were selected to obtain a uniform thin coating, necessary for both dielectric and bond coat. This would ensure that the electrical properties of the TENG would be maximized while still allowing for thick coatings to be produced. The relatively fast traverse speed of 50 mm/s promotes a thin deposition layer per pass, while the 3 mm step increment ensures adequate overlap between spray tracks to achieve good coating continuity.

The resulting coating exhibited a uniform silver-gray appearance with no visible delamination or discoloration, indicative of good bonding with no oxidation. Cross-sectional analysis using the SEM shows an average coating thickness of 90 ± 12 μm. An SEM image of the Al coating is shown in Figure 65. The coating was rough across the substrate, and from the cross section there appears to be uniform particle deposition and effective substrate coverage, with a ragged surface profile.

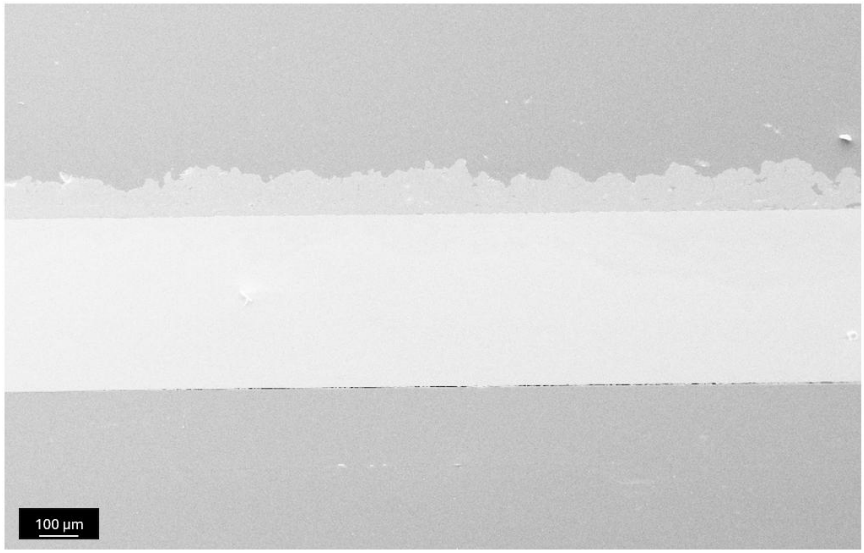

Figure 65: Al Coating on Cu substrate

Surface roughness was measured at an average Ra value of 9.86 $\pm$0.24 µm. This roughness is common for cold-sprayed aluminum and is beneficial for maximizing real contact area with the opposing tribonegative layer in the TENG assembly.

Overall, the Al coating demonstrated the expected quality and microstructural properties for use as a tribopositive electrode in a vertical contact-separation TENG. The coating serves as a reference baseline for subsequent comparison with the PFA tribonegative coating layer.

6.1.2 Cu Bond Coat

Also shown in Table 1 is the summary of the spraying parameters for the Cu powder. A dendritic copper powder was sprayed using nitrogen as the process gas at a stagnation pressure of 400 psi and a stagnation temperature of 375 °C. Compared to aluminum, slightly lower gas pressure and temperature were sufficient to accelerate and soften the copper particles for impact because Cu's higher density and ductility promote effective plastic deformation during deposition. Nitrogen was again used because of ease of availability and helped minimize oxidation in flight, preserving the metallic bonding capability of the particles.

A steel nozzle was selected for copper spraying due to the higher hardness of copper relative to aluminum. In this case, a polymer nozzle may have been prone to erosion or

deformation when exposed to harder, more abrasive copper particles. The stand-off distance was maintained at 10 mm, with a traverse speed of 150 mm/s and a 3 mm step increment. The higher traverse speed was chosen to produce a thinner layer per pass, reducing the risk of excessive buildup and promoting coating uniformity, as this coating was intended to serve as a bond coat and would increase the overall thickness of the Cu substrate, potentially causing issues with internal electrical resistance if built up too thick, while the 3 mm increment ensured track overlap. As with aluminum, 10 passes were applied to gradually build up the coating while maintaining consistency in thickness and surface coverage. Figure 66 provides an SEM image showing the Cu coating on the Cu substrate.

Figure 66: Cu coating on Cu substrate

The coating exhibited a common red brown appearance associated with copper with each spray pass visible from the high traverse speed and step. Figure 67 shows the Cu coating on the Cu substrate.

Figure 67: Cu coating on Cu substrate

There was no delamination, indicative of good adherence. Cross-sectional analysis using the SEM shows an average coating thickness of approximately 95±10 µm. The coating thickness was non uniform across the substrate, providing a rough surface. Visually from the SEM images, no porosity can be seen either.

Surface roughness yielded an average Ra value of 14.07±0.83 µm. This roughness provided a higher average Ra than the traditional grit blasting methods. Several peaks and valleys are visible in the coating which can provide enhanced mechanical interlocking for the PFA coating to adhere to. Overall, the Cu coating demonstrated the expected quality and microstructural properties for use as an electrode in a vertical contact-separation TENG.

The deposition of PFA onto the Al bond coat was successfully carried out using parameters developed by Leclerc et al [118]. In the current work, the Al bond coating had a surface roughness of 9.40 µm, and as-received PFA powder was deposited directly onto it using a straight-section nozzle and substrate preheating. A standoff distance of 15 mm was used. The straight-section nozzle accelerates PFA powder to lower velocity than a conventional converging-diverging nozzle and prevents debonding upon impact. The parameters used for spraying PFA onto Al are summarized in Table 2.

Table 2: CS parameters for PFA onto Al bond coat

Material	PFA
Powder Geometry	Irregular
Gas Type	Nitrogen
Stagnation Pressure in bulk pack	60 psi
Stagnation Temperature	375 ºC
Stand-off Distance	15 mm
Traverse Speed	150 - 200 mm/s
Step Increment	3 mm
Nozzle Material	Steel
Throat Diameter	1.8 mm
Nozzle Length	151.5 mm
Exit Diameter	7 mm
Preheater Temperature	150 – 200 °C

In CS, coating adhesion is strongly influenced by the residual stresses within the coating. When depositing dissimilar materials such as PFA onto Al, the significant difference in their thermal expansion coefficients leads to residual stresses due to thermal mismatch. This can cause mechanical bonds at the coating/substrate interface to fail via sliding movement. To mitigate this issue, the substrate was preheated to 200 °C.

Although the gas exiting the nozzle initially has a higher stagnation temperature of 375 °C, mixing with ambient air and convective cooling at the substrate surface reduces the

effective temperature. The absence of coating delamination indicates that substrate preheating successfully minimized residual stresses caused by the thermal expansion mismatch. An image showing the PFA and Al coatings side by side is shown in Figure 68.

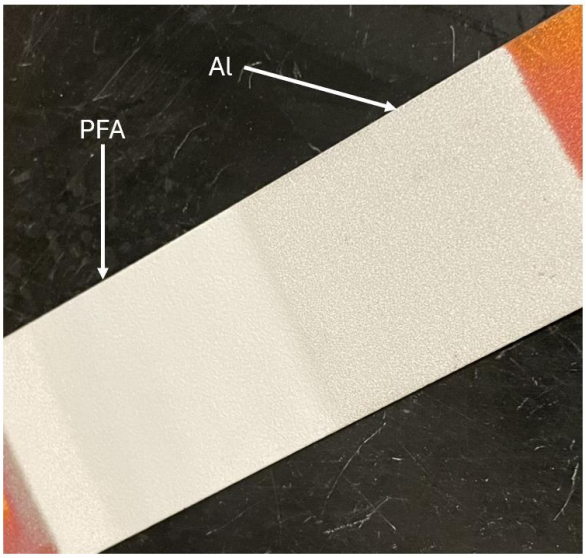

Figure 68: PFA and Al coatings side by side

A coating thickness of 105 ± 4 µm was obtained by spraying single passes of PFA onto the Al substrate. While thicker PFA coatings can be achieved through multiple passes, as demonstrated in previous works, the decision to use a thinner, single-pass layer in this study was driven by functional requirements specific to vertical contact-separation TENGs, as shown in equation 16 in Chapter 3.1.5. Excessive coating thickness can interfere with charge transfer efficiency and reduce overall device performance, as it alters the dielectric thickness. Thus, a minimal and continuous coating was desired to preserve the triboelectric properties while also maintaining mechanical stability and decent adhesion. An SEM image in Figure 69 shows the PFA on the Al bond coat.

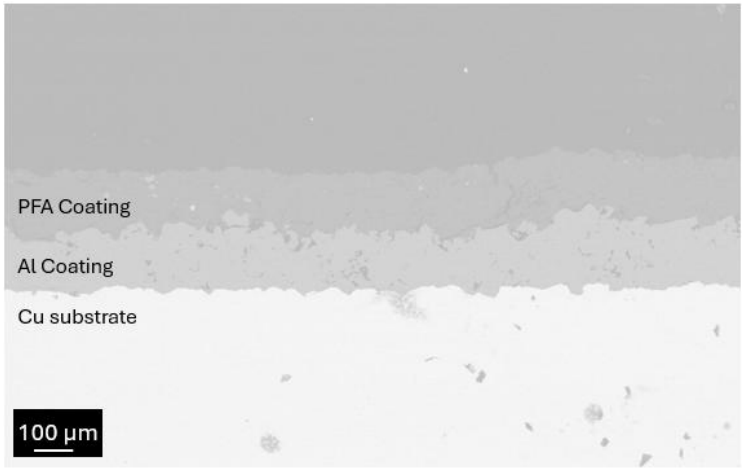

Figure 69: PFA on Al bond coat on Cu substrate

6.1.3 PFA Coating on Cu Bond Coating

The deposition of PFA directly onto the Cu substrate represented a novel aspect of this study and required additional development work, as no established parameters existed for this specific material combination within the CS framework. Initial spray trials used grit-blasted copper substrates with a surface roughness of approximately 4.17 ± 0.27 µm µm Ra, prepared using silica grit and blasted at 45° relative to the substrate surface on both sides. This approach was intended to minimize substrate bending; however, due to the thinness of the samples, bending still occurred. Initial coatings were sprayed on the grit blasted copper with substrate preheating to 200 °C implemented, as with the Al trials, to reduce residual stresses arising from the thermal expansion mismatch between Cu and PFA. However, despite this thermal conditioning, significant coating delamination was observed shortly after deposition. This suggested that adhesion failure was driven primarily by inadequate mechanical interlocking or interfacial instability, rather than purely by thermal stresses.

To improve bonding, the blasting parameters were then modified by increasing the grit blasting pressure which raised the surface roughness to approximately 4.39 ± 0.19 µm Ra. This adjustment aimed to create deeper anchor points for the relatively soft PFA particles to embed into. However, delamination persisted across the coated area, indicating that further roughness alone could not resolve the underlying adhesion issue. A delaminated PFA coating on the grit blasted substrate is shown in Figure 70.

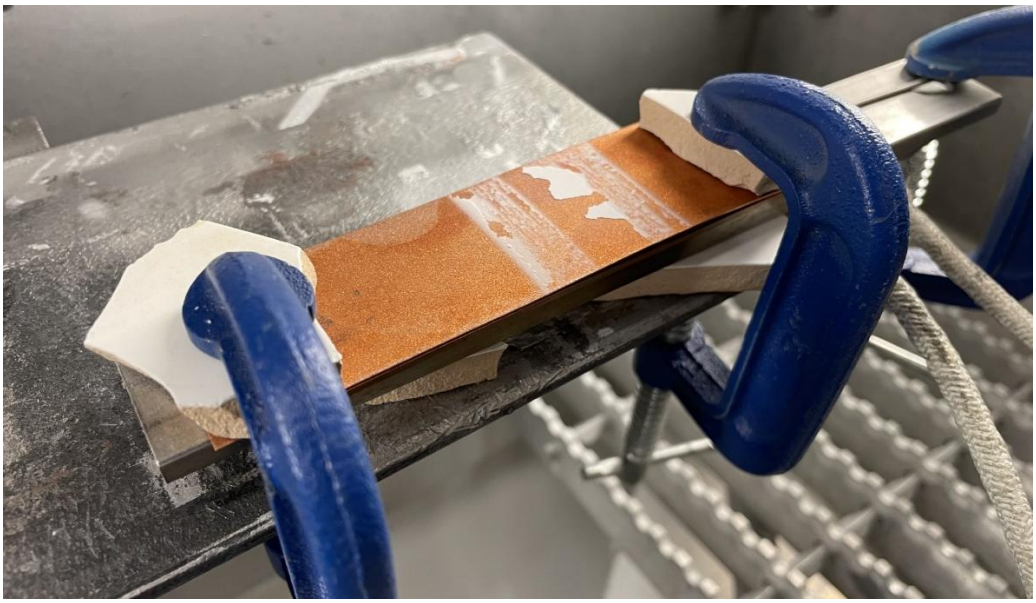

Figure 70: Delaminated PFA coating on grit blasted Cu substrate

It is also worth noting that any bending induced in the substrate during grit blasting may have reduced heat transfer from the strip heater. The resulting air gap between the heater and the substrate increases thermal resistance, thereby limiting effective heat conduction to the substrate.

A new approach was then developed: a cold-sprayed copper bond coat was applied directly onto as received Cu substrate prior to PFA deposition. This bond coat raised the effective surface roughness to Ra= 14.07±0.83 µm and introduced an intermediate layer with higher surface complexity than grit blasted surfaces. Following the application of the bond coat, a uniform and adherent PFA layer was successfully deposited. A PFA coating thickness of 107 ± 6 µm was reached. This multi-layer approach improved not only the mechanical anchoring but may have also helped distribute interfacial stresses more uniformly. There was a discoloration of the Cu bond coat and substrate when preheating was performed at 200 °C. This is from oxidation which is accelerated at higher temperatures. Decreasing the preheating temperature to 150 °C showed no discoloration of the Cu coating and did not lead to delamination of the PFA to the Cu bond coat. A successful coating of PFA onto Cu is showed in Figure 71, along with SEM photos at 100x and 250x magnifications shown in Figures 72a and 72b, respectively.

Figure 71: Successful coating of PFA onto Cu bond coat

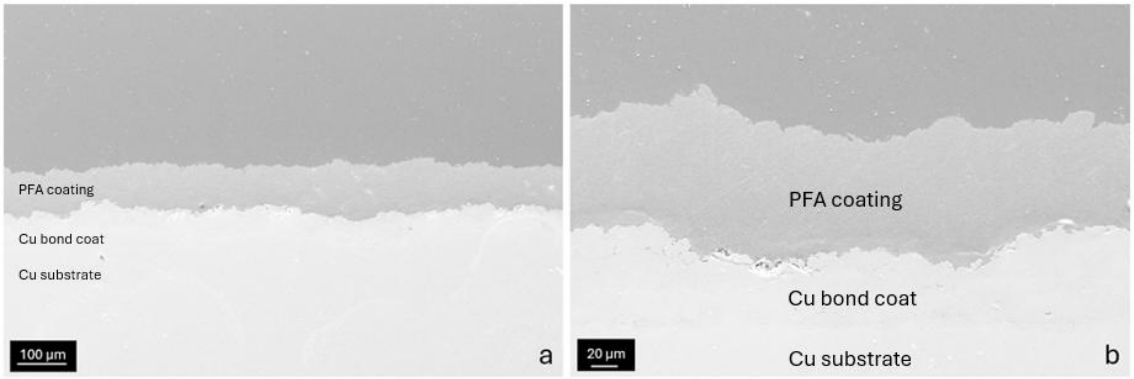

Figure 72: a) PFA on Cu bond coat at 100x mag b) PFA on Cu bond coat at 250x mag

In parallel, the step size used during spraying was increased from 3 mm to 5 mm. This modification improved the overall uniformity of the deposited layer by minimizing localized heat buildup and reducing the potential for stress concentration at overlap regions and delamination. The combined adjustments of enhanced surface preparation, substrate preheating, the use of a bond coat, and using the existing optimized spraying parameters were critical in achieving a PFA coating on Cu. The results provide a useful baseline for future studies involving polymer-metal CS interfaces. The gas temperature used was 375 °C, and a stagnation pressure of 60 psi was used. A summary of coating deposition by

varying the substrate preheating temperature, step, and traverse speeds is shown below in Table 3.

Table 3: Spraying Trials for PFA directly onto Cu

Substrate Type	**Substrate Preheater Temperature (°C)**	**Step Size (mm)**	**Traverse Speed (mm/s)**	**Coating Success (Yes/No)**
Grit Blasted Cu	200	3	150	No
Grit Blasted Cu	200	5	150	No
Nitrogen Grit blast Cu	200	3	150	No
Nitrogen Grit blast Cu	150	3	200	No
Nitrogen Grit blast Cu	150	5	200	No
Cold sprayed Cu	150	3	150	No
Cold sprayed Cu	150	3	200	Yes

6.2 Electrical Characterization

6.2.1 Open Circuit Voltage

Following the successful depositions of the Al, Cu, and PFA coatings the TENG layers were constructed and mounted for electrical characterization. They were then connected directly to the Kiethley 6517B electrometer with a load impedance 200 MΩ where V_{oc} could be determined.

V_{oc} for a TENG is the representation of the maximum potential difference generated between the electrodes when no current flows between them, shown in Figure 30 from Chapter 3.1.5. This is known as the open circuit condition. To measure this, the high resistance provided by the electrometer is necessary to assume the circuit is open circuit, as resistance is infinite in this case. For a TENG operating in vertical contact separation, V_{oc} is determined by the amount of charge transferred during contact and how this charge interacts with the electric field as the electric field separates. While infinite plates were assumed for developing the general model governing the electrical characteristics of TENGs, V_{oc} does not actually increase indefinitely with separation distance. It reaches a maximum at an optimal gap and then decreases.

This arises as competing effects act simultaneously. As the electrodes separate, the effective capacitance between them decreases, increasing the potential difference and increasing V_{oc}. However, the actual charge on the surface can begin to decrease because of current leakage along the surface, and dielectric relaxation especially on the polymer surface. As polymers are not perfect insulators and have finite conductivity, over time the charges located in them can reorient, move through the material, reducing the surface net charge available for generating voltage.

The maximum V_{oc} occurs when the rate of voltage increase from decreasing capacitance is balanced by the rate of voltage decrease caused by charge loss or redistribution. Beyond this separation distance, further separation reduces the strength of the electric field which leads to a drop in measured voltage.

To account for this, the separation distance was varied experimentally to identify the point of maximum V_{oc}. The optimal distance was found this way and was then used for all

subsequent measurements. Figure 73 shows the voltage increase and subsequent decrease as a function of separation distance for both Designs 1 and 2.

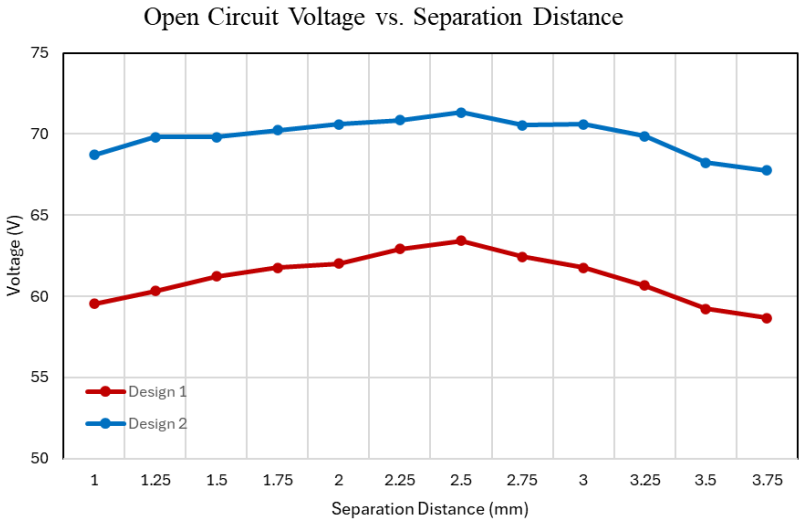

Figure 73: Open circuit voltage vs. separation distance

Both designs showed a gradual rise in V_{oc}, peaking in each case at approximately 2.50 mm before decreasing again. As the separation distances are the same, this indicates that the difference in voltage generated is not because of the operating distance, rather factors relating to the configurations and material choices of the TENGs and charge transferred upon contact. The voltage for Design 1 started at 59.55 $\pm$ 0.098 V at a separation distance of 1 mm and gradually increased to 63.42 $\pm$ 0.01 V before beginning to drop after 2.50 mm. Similarly for Design 2, a reading of 68.71 $\pm$ 0.01 V was recorded at 1.00 mm and increased until reaching 71.32 $\pm$ 0.01 V, which as Design 1 also occurred at 2.50 mm. The full waveforms for V_{oc} for both Design 1 and Design 2 are shown in Figure 74 at the separation distance which generated the highest V_{oc}, and at a frequency of 8 Hz. A screenshot of one full waveform, showing all the steps of voltage generation upon separation, a drop to zero after full separation, and voltage generation upon re-engaging is shown in Figure 75.

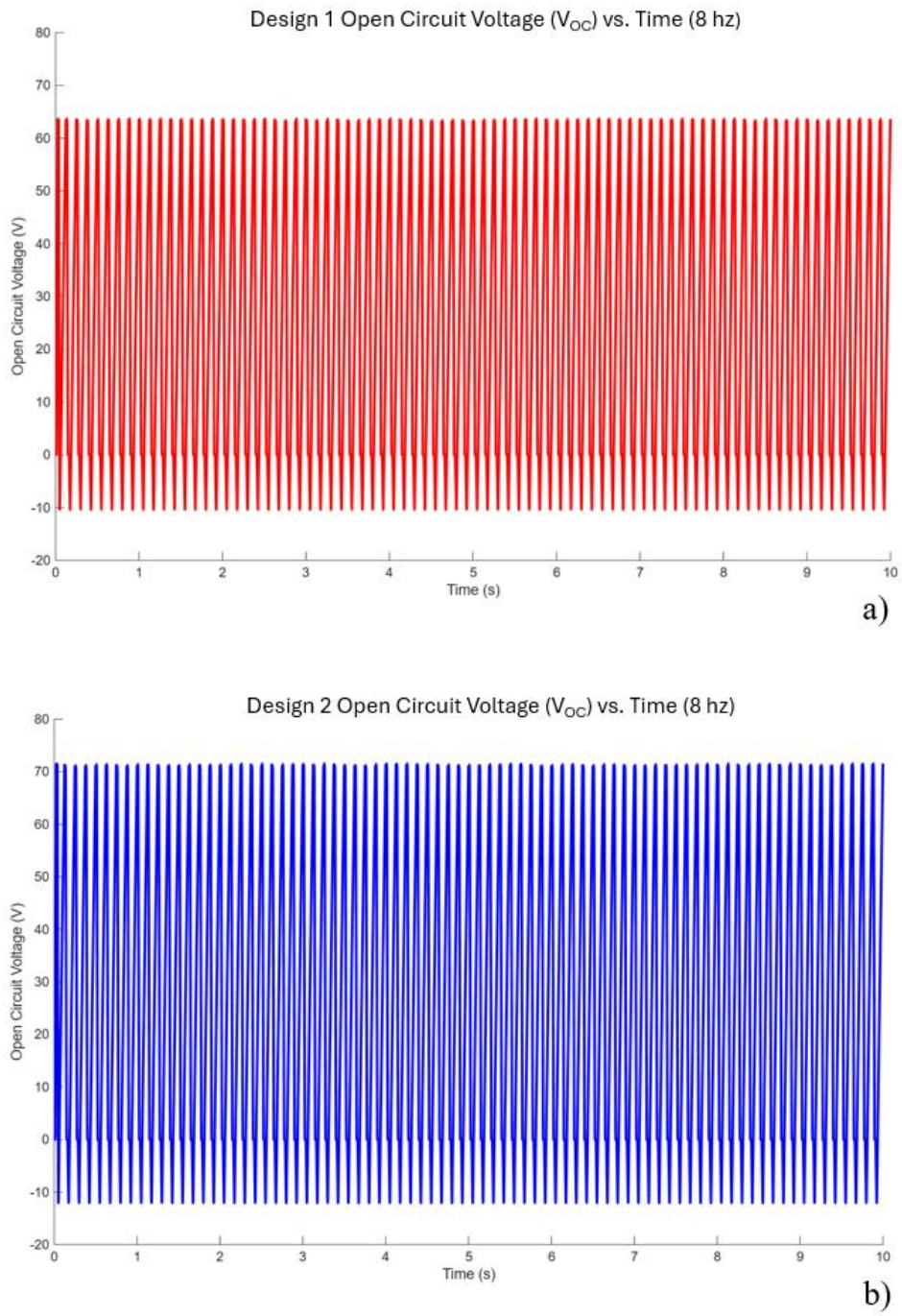

Figure 74: Open Circuit Voltage a) Design 1 b) Design 2

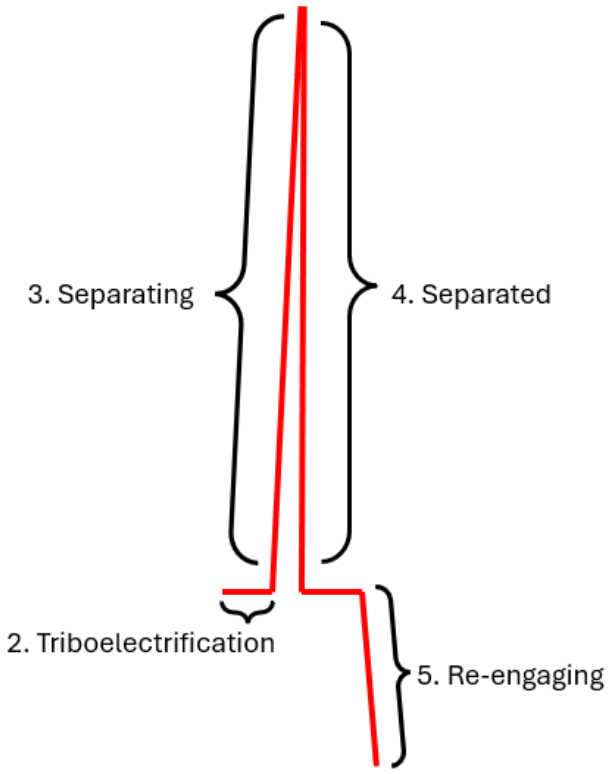

Figure 75: One cycle for a VS-TENG, showing voltage generation at 2. Triboelectrification, 3. Separating. 4. Separated, and 5. Re-engaging

A calculation was not made to determine the theoretical V_{oc}, which is consistent with current reporting literature. The accurate determination of the parameter σ is difficult as it depends on the material pair of both dielectric surfaces. For PFA and Al, no universally accepted σ exist, which means no reliable theoretical calculation of V_{oc} could be performed. Experimentally however, because the electrometer used possesses a high load impedance of 200 MΩ, current flows between the electrodes of the VS-TENG can be assumed to be zero, which allows the system to be reasonably assumed to be in the open-circuit condition.

The higher V_{oc} observed in Design 2 can be attributed to the direct deposition of PFA onto a Cu bond coat. Design 1 used an Al bond coat as Al had already been established as a successful substrate material for PFA. However, Al is a tribopositive material and would have allowed for an additional electric field to be generated which opposes the direction of the electric field direction of the air gap which is what induces V_{oc}. This is illustrated in a diagram in Figure 76.

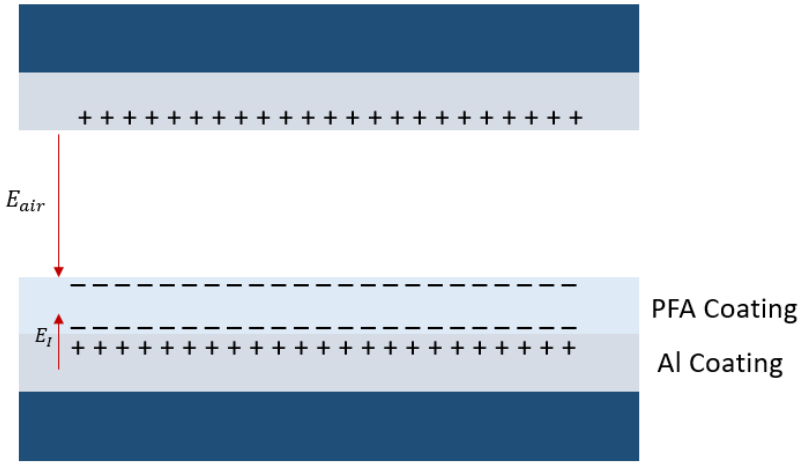

Figure 76: TENG diagram showing potential electric field generated at coating interface

This does interestingly bring an additional reason however for the better adherence of PFA onto Al as opposed to Cu. As PFA is negative on the triboelectric series and Al is positive, the local electric field generated at the interface of these two materials creates an electric field which could allow for additional attractive forces, complementing the mechanical interlocking and Van der Waals interactions that normally govern bonding between polymers and metals. Here, the interface of Al and PFA provides an electric field which opposes the electric field in the air gap, E_{air}. Because these two electric fields are opposite in direction, it could potentially reduce the total V_{OC}. This may help explain why V_{OC} is smaller for Design 1, the VS-TENG using an Al bond coat, compared to design 2, which sprays PFA directly on a Cu bond coat.

While this mechanism does offer a plausible theoretical explanation for why there is less available voltage in design 1 and better bonding, an actual contribution to adhesion is not quantified. Validation could be performed through controlled experiments comparing adhesion strengths such as peel tests or nanoindentation of PFA on Al vs. PFA on Cu. Studies could examine the effect of charging the interface to measure the difference in polarities at the interface. These investigations could help determine whether the triboelectric effect plays a measurable role in enhancing polymer-metal adhesion.

6.2.2 Short Circuit Current

The I_{sc} of a TENG represents the instantaneous current that flows between the electrodes when the external circuit is closed, reflecting the rate at which charge is transferred during

each contact–separation cycle. It is expressed in equation 14 in Chapter 3.1.3. Unlike V_{oc}, which represents the maximum potential difference when no current flows, I_{sc} provides insight into the dynamic behavior of charge flow under short-circuit conditions.

For V_{oc} measurements, the TENG electrodes were connected directly to the electrometer, which has a very high input resistance, ensuring that no current flows and that the measured voltage corresponds to the open-circuit potential. In contrast, measuring I_{sc} requires a zero-resistance path between the electrodes. To achieve this, a parallel circuit with negligible resistance was created, effectively shorting the electrodes while allowing current to flow freely. The high input resistance of the 6517B ensured that there were no parasitic current leaks toward the instrument, and its independent power supply did not impose additional loads on the TENG. This configuration ensures that the measured current corresponds to the true short-circuit current.

In a VS-TENG, I_{sc} depends strongly on the speed of contact and separation as demonstrated in equation 14. Faster motion induces a larger rate of current. To study this, the frequency of the Instron actuator was varied from 1 to 10 Hz, with the oscillation following a sine wave pattern. The separation distance was kept at 2.50 mm. Both designs showed steadily increasing currents up to around 6 and 8 Hz, with there being no significant difference in I_{sc} between 8 and 10 Hz. The increase in current does demonstrate that I_{sc} is directly related to mechanical excitation rate. The I_{sc} waveforms from 2-10 Hz in increments of 2 Hz are shown below in Figures 77 to 81. The average values per frequency measurement is shown in Table 4.

Table 4: Average Isc per frequency measurement

Frequency	**2 Hz**	**4 Hz**	**6 Hz**	**8 Hz**	**10 Hz**
Design 1 I_{sc} (µA)	1.170	1.213	1.291	1.314	1.322
Design 2 I_{sc} (µA)	1.384	1.421	1.472	1.477	1.480

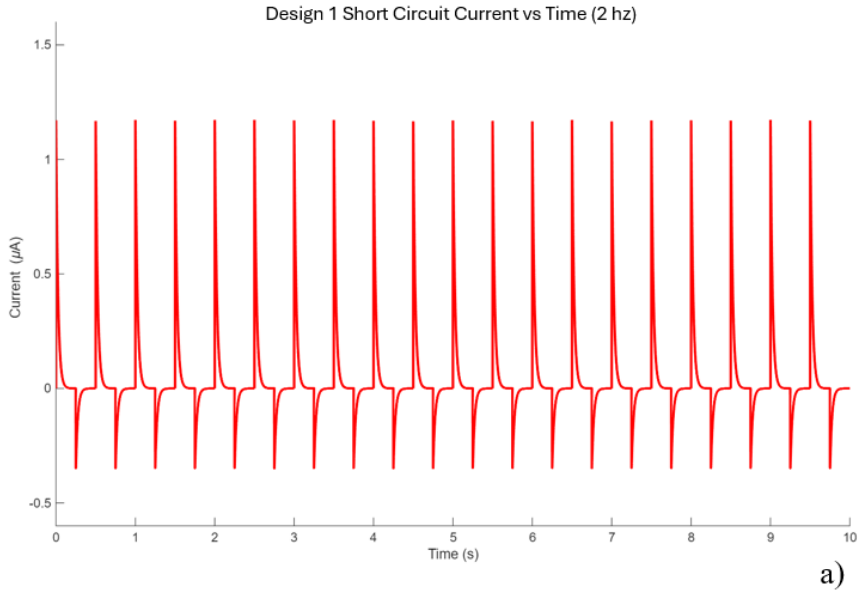

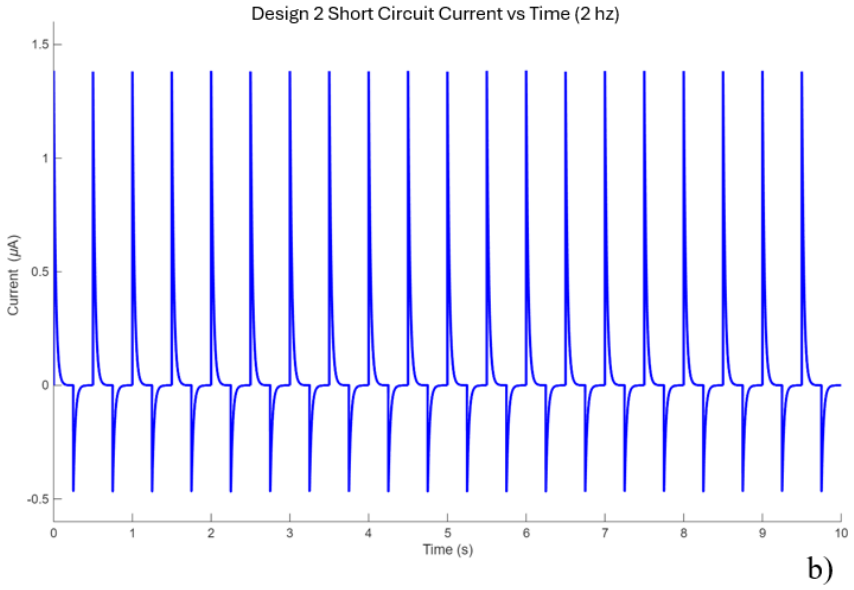

Figure 77: Short circuit current at 2 Hz a) Design 1b) Design 2

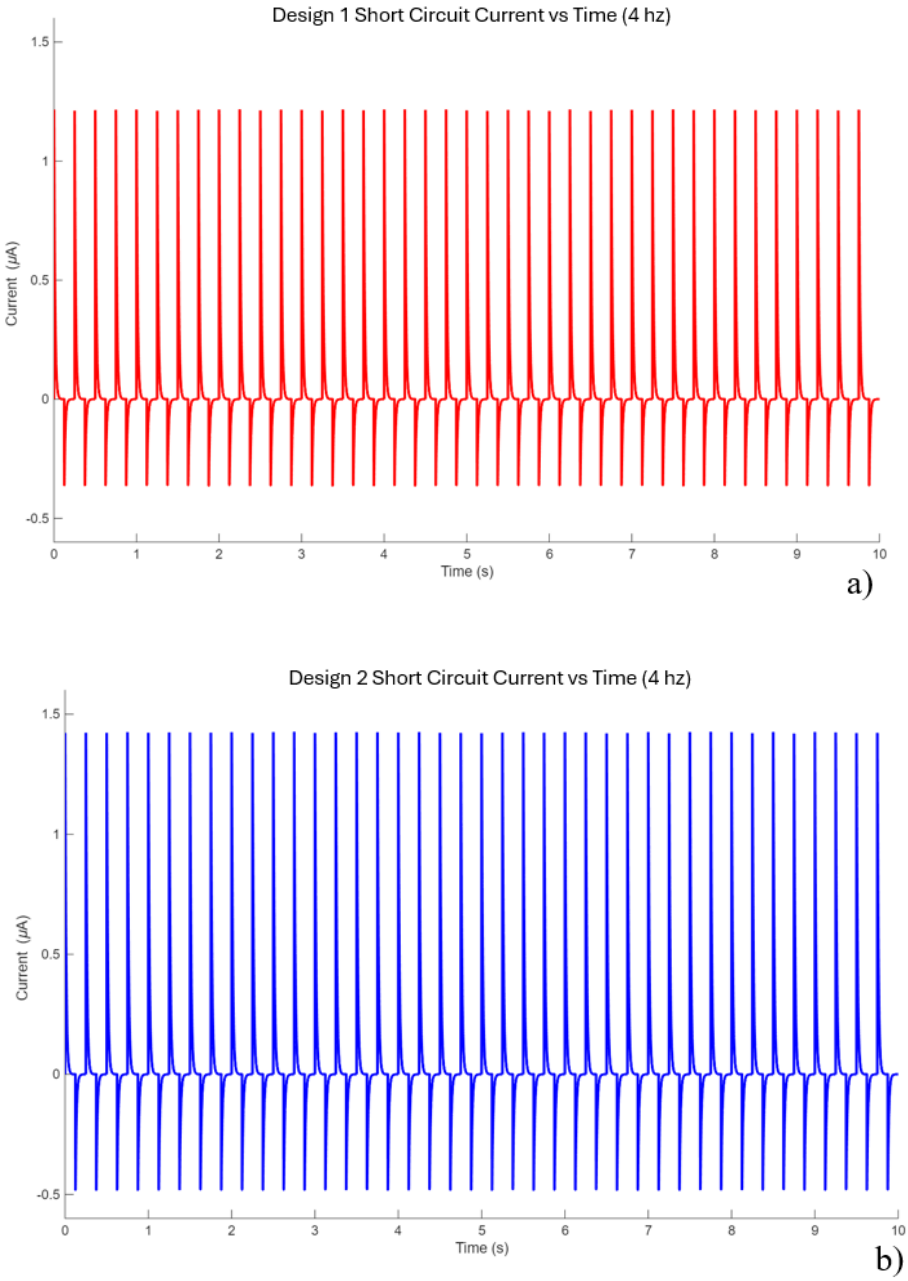

Figure 78: Short circuit current at 4 Hz a) Design 1b) Design 2

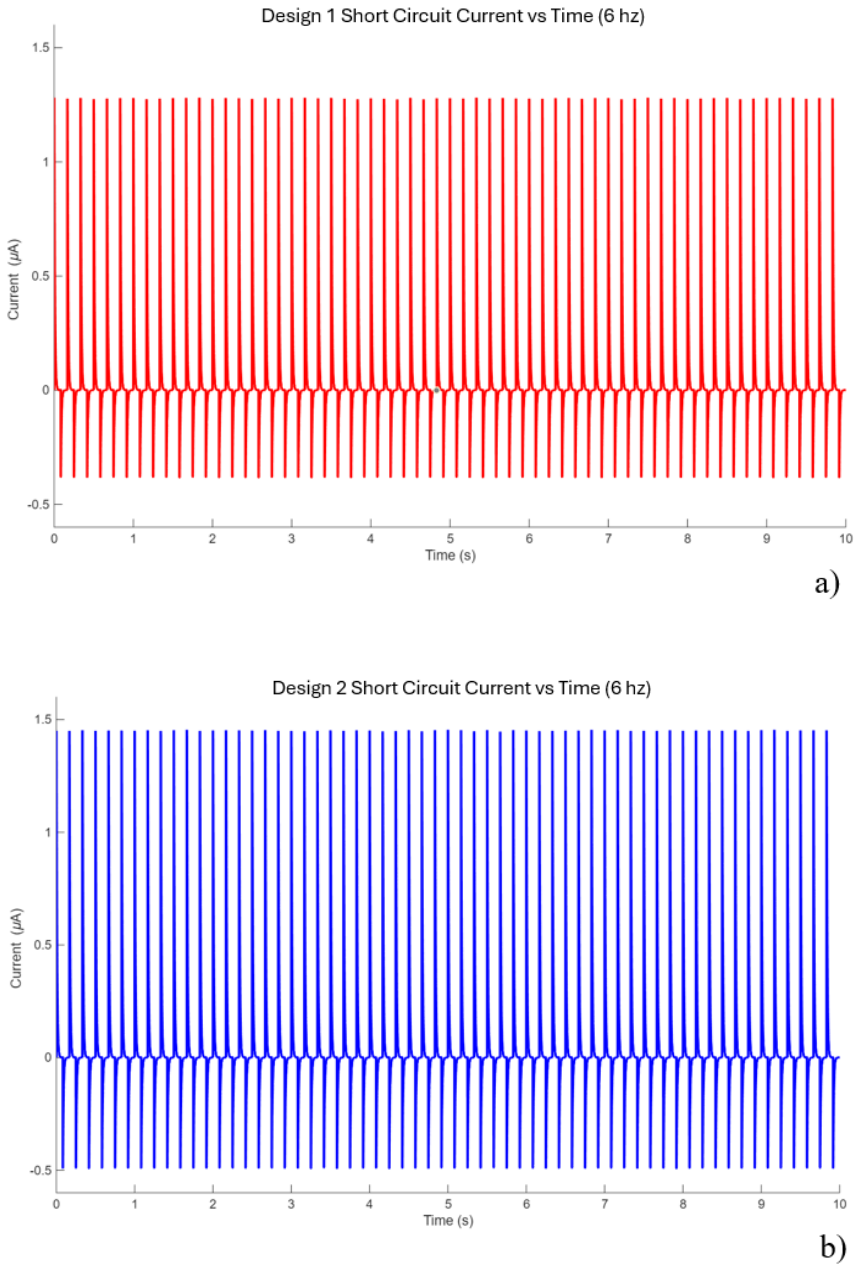

Figure 79: Short circuit current at 6 Hz a) Design 1b) Design 2

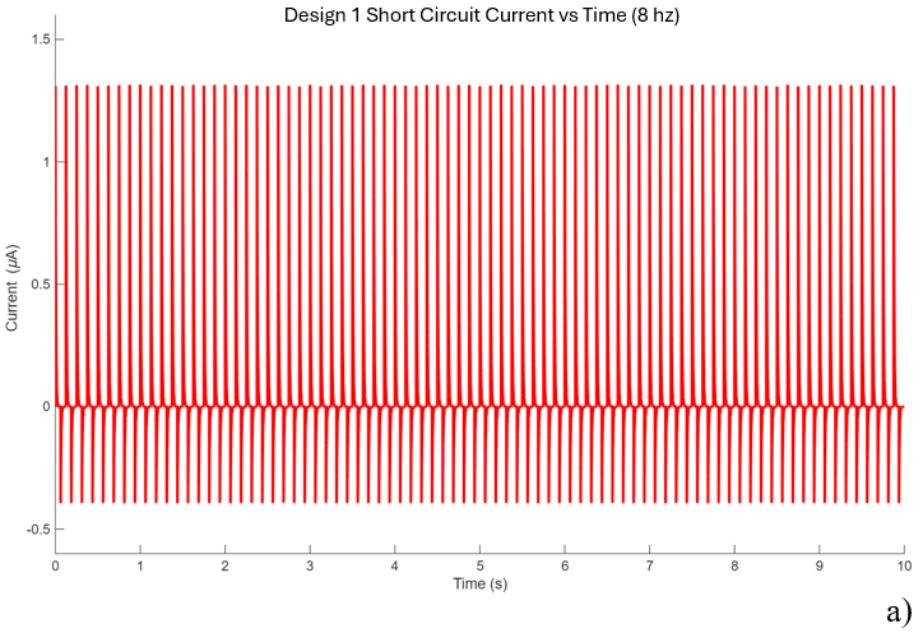

a)

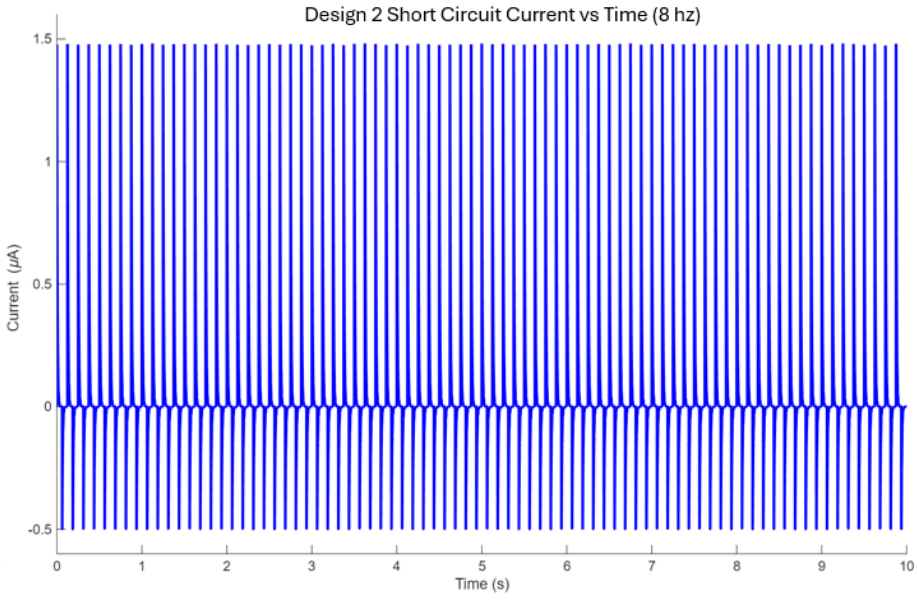

b)

Figure 80: Short circuit current at 8 Hz a) Design 1b) Design 2

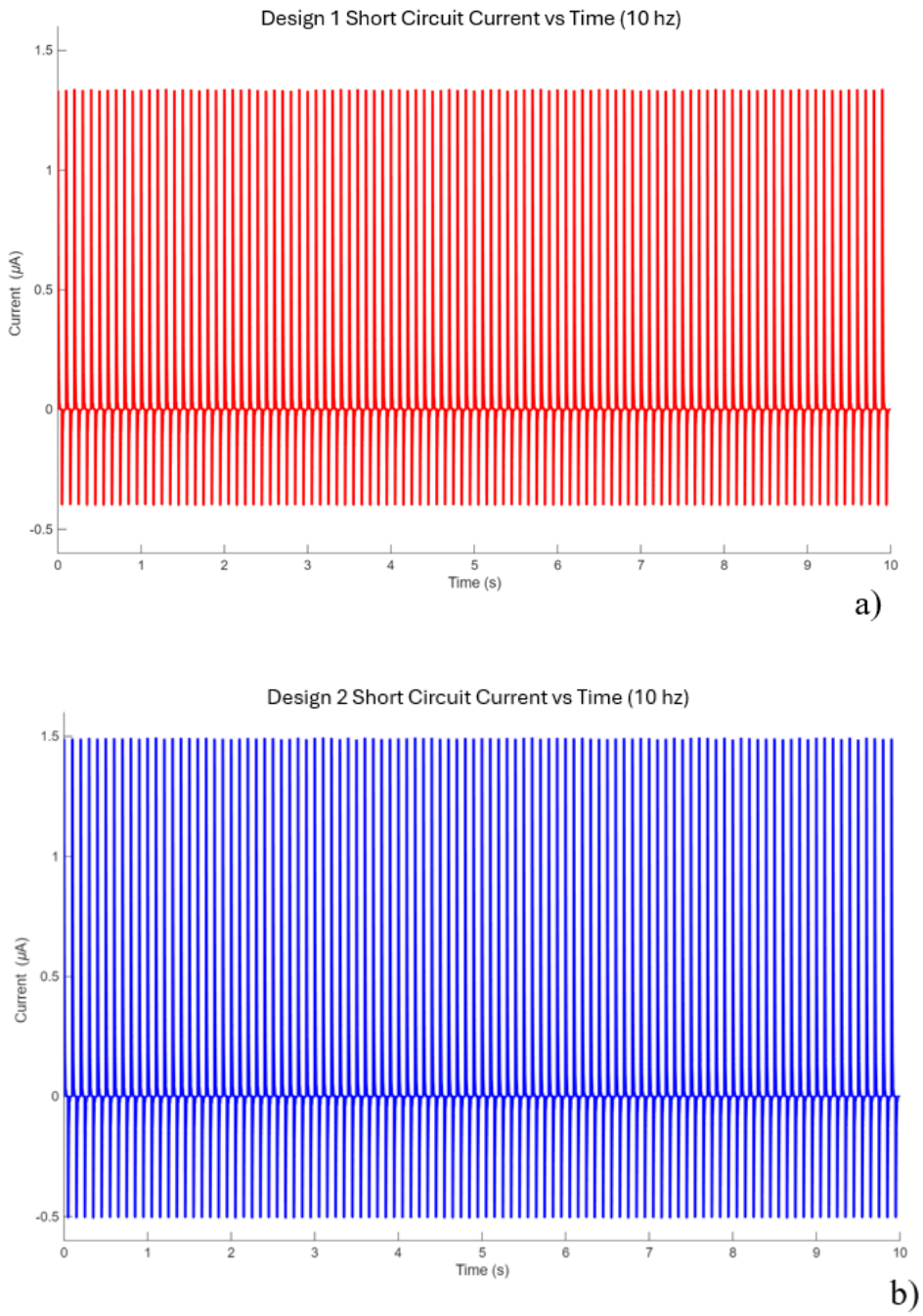

Figure 81: Short circuit current at 10 Hz a) Design 1b) Design 2

The plateaus of I_{sc} in the 6 – 10 Hz range arises as the contact time between the triboelectric layers decreasing as frequency increases. First, the contact time between the triboelectric layers decreases as frequency increases. When the electrodes separate too quickly, there is insufficient time for the surface charges to fully transfer during contact, limiting the

maximum achievable electron transfer between dielectrics, and decreasing the surface charge density σ. Second, instrumentation limitations impose additional constraints. Electrometers and data acquisition systems have finite response times, rise times, and sampling rates; if the mechanical excitation becomes faster than the instrument can accurately follow, the measured current may underestimate the true instantaneous I_{sc}. Together, these factors explain why the measured current plateaus around 8 Hz, and why no significant differences were observed up to 10 Hz.

Design 2 consistently produced higher peak currents than Design 1 across all frequencies, reaching a maximum of 1.480 μA compared to 1.322 μA for Design 1. This behavior is consistent with trends observed in V_{oc} measurements. The improved current output in Design 2 can be attributed to the direct deposition of PFA onto a Cu bond coat. The higher available voltage in Design 2 allows more current to flow through a minimal-resistance path, whereas the Al bond coat in Design 1 introduces an opposing field that reduces charge transfer as discussed in 6.2.1.

Both designs exhibited repeatable current waveforms over multiple cycles which indicates consistent operation and no loss of surface charge from any dielectric relaxation or leakage.

6.2.3 Short Circuit Charge

The short-circuit charge (Q_{sc}), appears on the electrodes after being connected. It represents the total electrical charge transferred between the electrodes during a single cycle and is shown on the electrodes in Figure 25 in Chapter 3.1.3. It is expressed by isolating for Q_{sc} when $V = 0$ from the condition that $V_{air} = V_1 + V_2$, where V_1 and V_2 are the voltages present in dielectrics d_1 and d_2, respectively. It is expressed in Chapter 3.1.3 in equation 13. Q_{sc} is a fundamental parameter in TENG characterization because it reflects the maximum charge that can be mobilized between the electrodes and, therefore, the charge available on the dielectric surfaces. When measured, Q_{sc} corresponds to the point at which the charges on the electrodes and dielectrics are equalized, representing the maximum allowable charge that can be transferred in a single cycle. This makes Q_{sc} an important parameter in understanding the efficiency and performance of the TENG in converting mechanical energy into electrical energy.

Experimentally, Q_{sc} was measured using the Kiethley 6517B electrometer in charge-measurement mode. In this configuration, the electrodes were connected directly to the electrometer, with a circuit in parallel used to allow the free movement in electrons. The set up is shown in Figure 60 in Chapter 5.4.3. The electrometer is equipped by design with a feedback capacitor with high stability and low leakage located in the input stage of its current/voltage converter. When charges flow into the input terminal, it accumulates on the feedback capacitor. As the voltage across the capacitor can also be measured, the charge can therefore be calculated and then displayed as the product of capacitance and voltage,

$$Q_{sc} = C_f V_f$$

Where C_f and V_f are respectively, the capacitance and voltages across the capacitor.

Q_{sc} is dependent on the separation distance x(t), seen in equation 13. Although faster contact separation cycles increase the current and enables more rapid charge redistribution, it does not affect how much charge can transfer. This is dictated by the triboelectric pairing from the dielectric materials selected and the electric field strength between dielectrics quantified by V_{oc}. If, however, the contact time is too short, charge transfer may be incomplete, limiting Q_{sc} and showing lower readings. In the experiments conducted, both designs displayed stable and repeatable Q_{sc} measurements. The values selected were taken at the 2.5 mm separation distance determined when finding V_{oc}. The frequency was varied again from 2-6 Hz. The Q_{sc} waveforms are shown below in Figure 82 and 83.

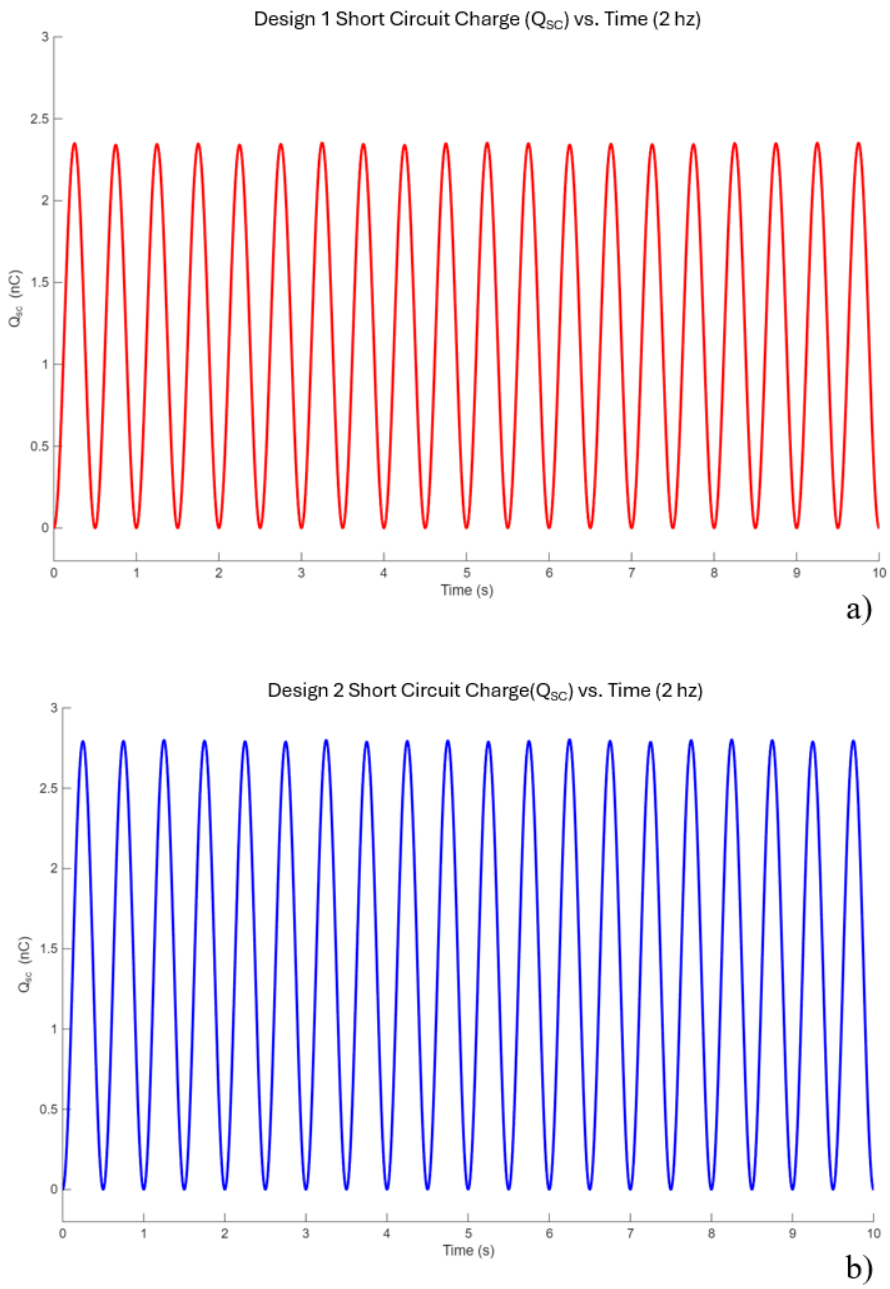

Figure 82: Short circuit charge at 2 Hz a) Design 1 b) Design 2

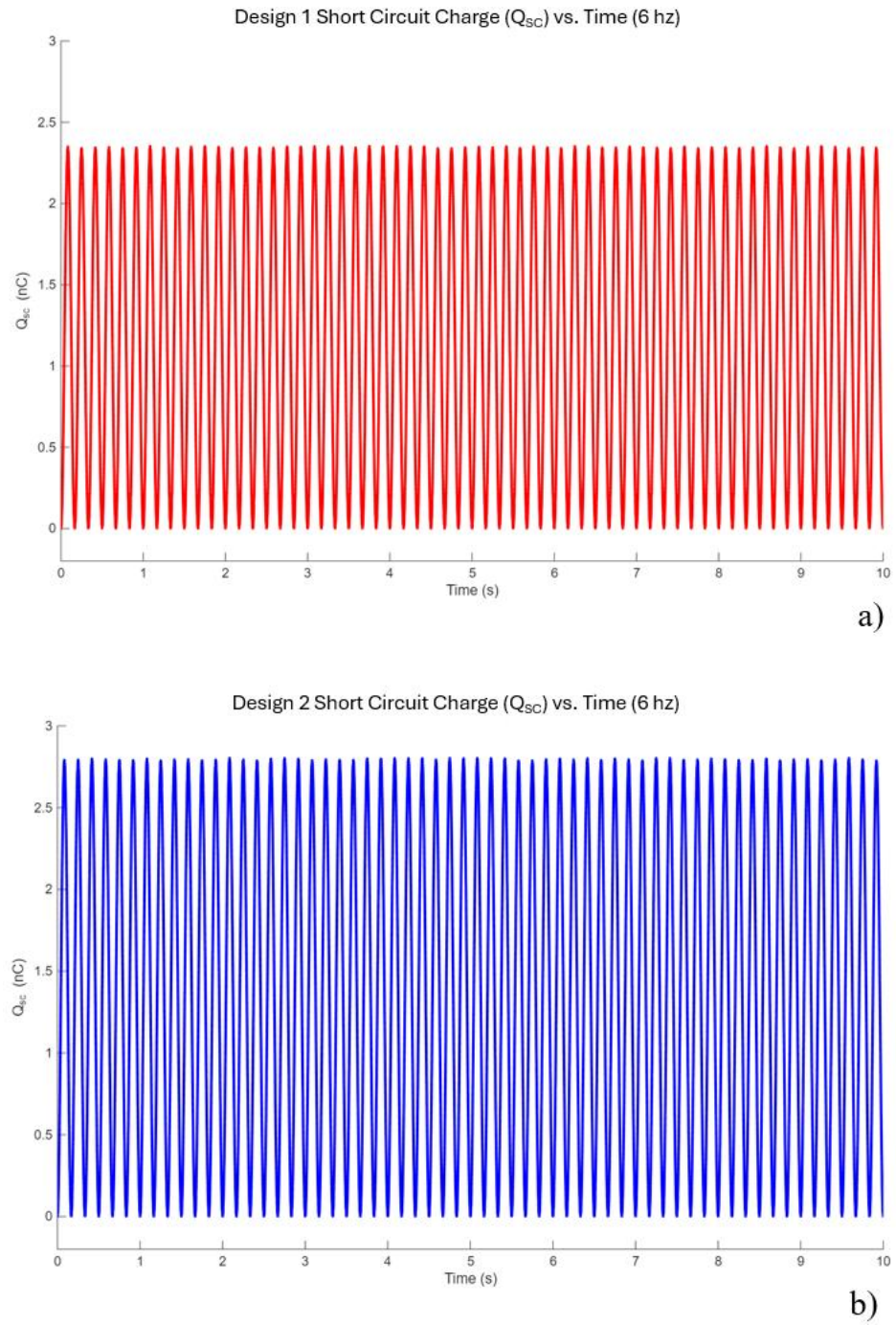

Figure 83: Short circuit charge at 6 Hz a) Design 1 b) Design 2

Design 2 consistently exhibited higher Q_{sc} values than Design 1, reaching 2.800 nC compared to 2.344 nC for Design 1. This observation is consistent with the trends in V_{oc} and I_{sc}. The superior performance of Design 2 can be attributed to the direct deposition of PFA onto a Cu bond coat, which facilitates more efficient charge accumulation and transfer.

In contrast, the Al bond coat in Design 1 introduces a partial opposing field relative to PFA, reducing net charge transfer and resulting in lower Q_{sc}.

Both designs showed repeatable Q_{sc} values over multiple cycles, indicating minimal loss of surface charge due to dielectric relaxation or leakage. These results demonstrate that the combination of Cu and PFA in Design 2 not only produces higher voltage and current but also maximizes the total charge transferred per cycle, confirming its improved overall electrical performance.

6.2.4 Operational Output Voltage (V)

The operational output voltage represents the potential difference measured across an external load when the TENG is operating under practical electrical conditions, rather than in the open-circuit state. For these measurements, a 10 MΩ resistive load was connected across the electrodes, as this was where peak power was determined to be. The electrometer was connected in parallel, shown in Figure 61 in Chapter 5.4.3. The separation distance was kept at the optimal 2.50 mm determined from the V_{oc} experiments. Measuring the output under load provides insight into the actual voltage the TENG can deliver to an external circuit, which is necessary for evaluating its usability in real-world applications.

The output voltage depends on both the intrinsic charge generated by the triboelectric layers and the voltage division between the TENG internal capacitance and the external load resistance. As expected, the output voltage under the 10 MΩ load is lower than the open-circuit voltage, because a portion of the voltage is dropped across the internal impedance of the TENG as current flows. The waveforms at a frequency of 8 Hz for both designs is shown in Figure 84.

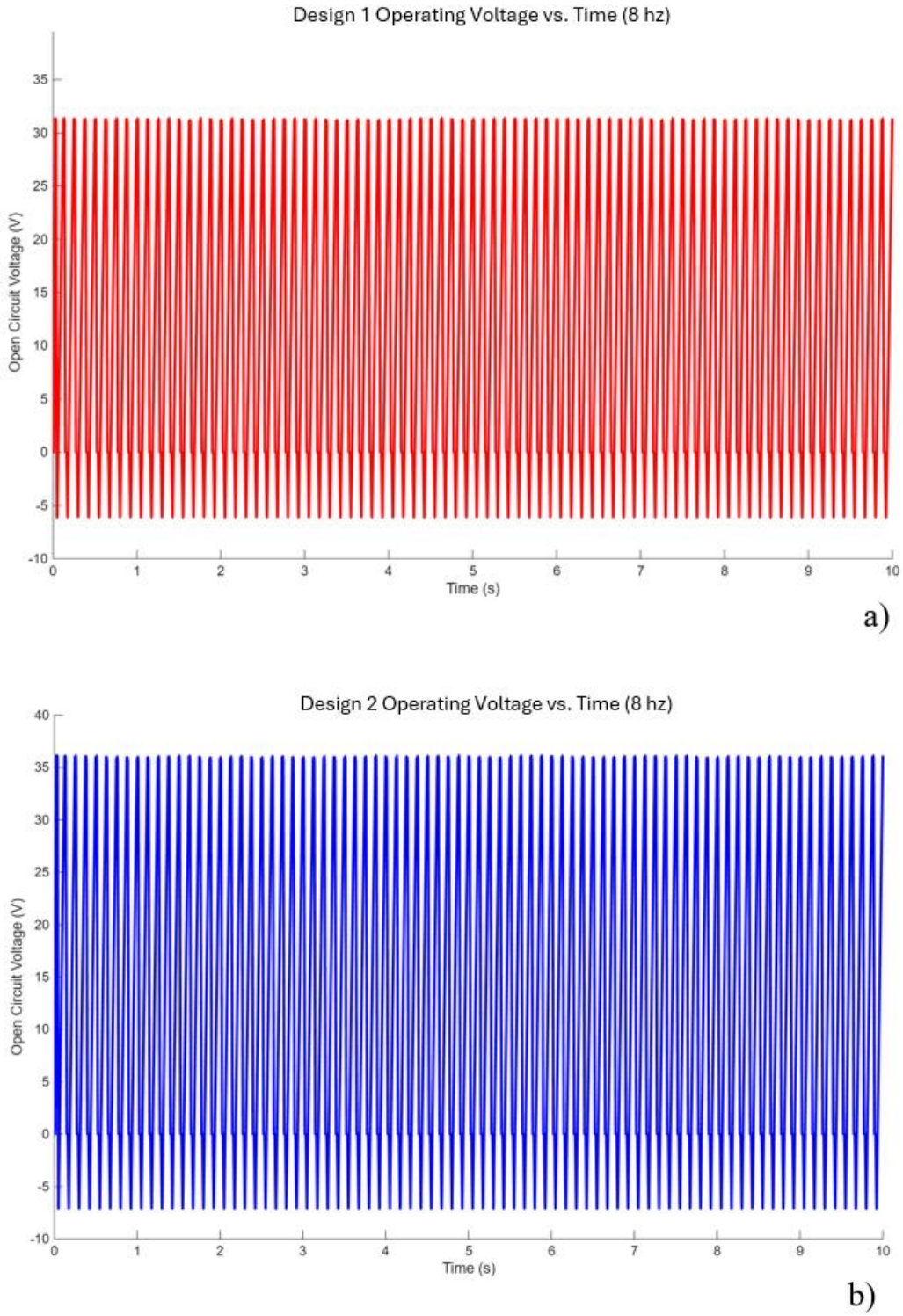

Figure 84: Operating voltage at 10 MΩ load a) Design 1 b) Design 2

Design 2 consistently produced higher output voltages than Design 1, reaching a maximum of 36.83 V compared to 31.28 V for Design 1. This behavior aligns with the higher V_{oc} and Q_{sc} observed previously and reflects the more efficient charge generation and transfer enabled by the Cu bond coat. Both designs displayed stable and repeatable voltage waveforms over multiple cycles as shown in the figures.

6.2.5 Operational Output Current (I)

Similarly to the operational output voltage, the operational output current represents the current flowing through the external resistive load during typical TENG operations. With the 10 MΩ external resistor in place and the electrometer connected in parallel with separation distance maintained at 2.5 mm (Figure 61), current measurements were taken. The waveforms for both designs are shown for 2 Hz and 8 Hz in Figures 85 and 86.

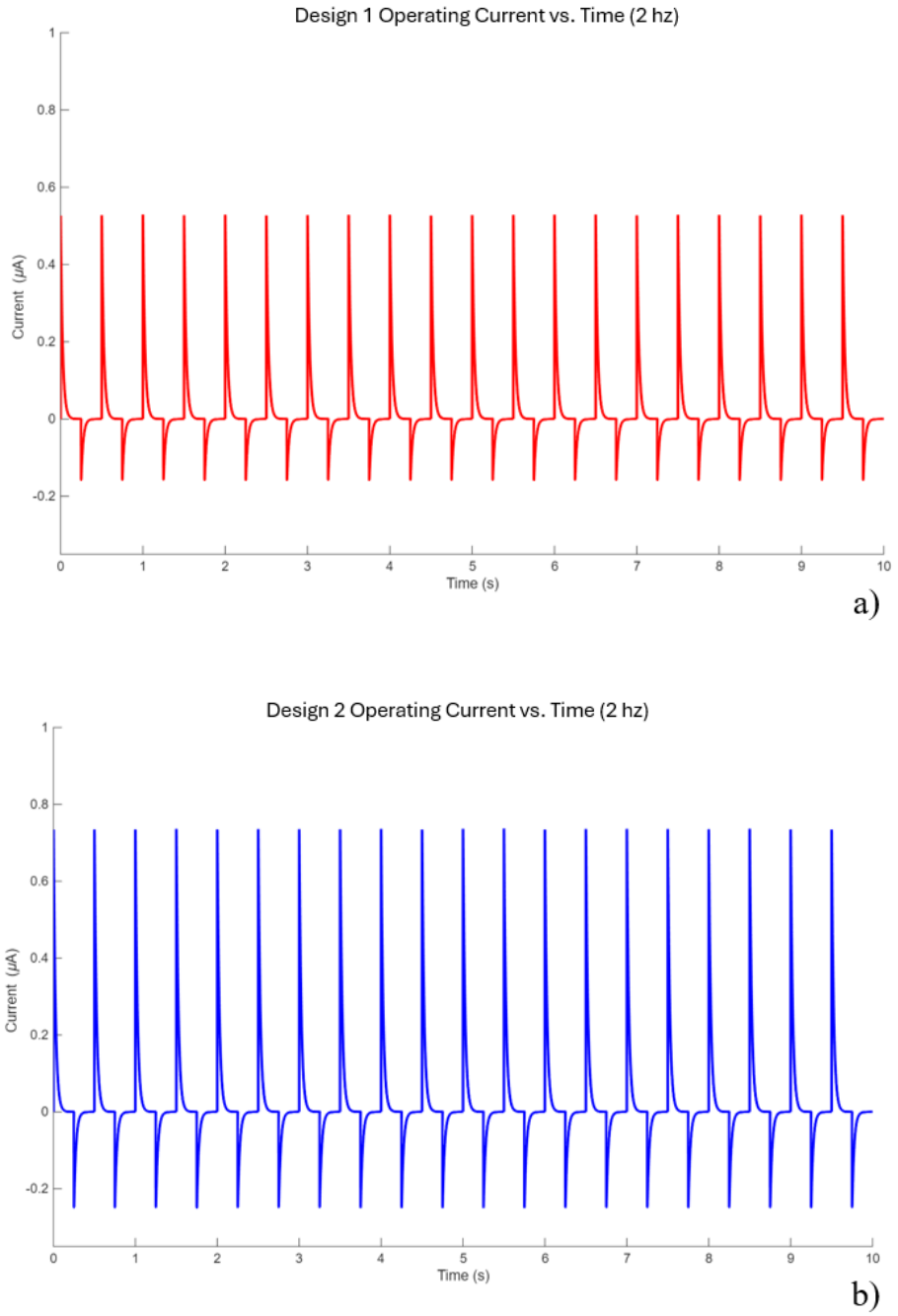

Figure 85: Operating current at 10 MΩ and 2 Hz a) Design 1 b) Design 2

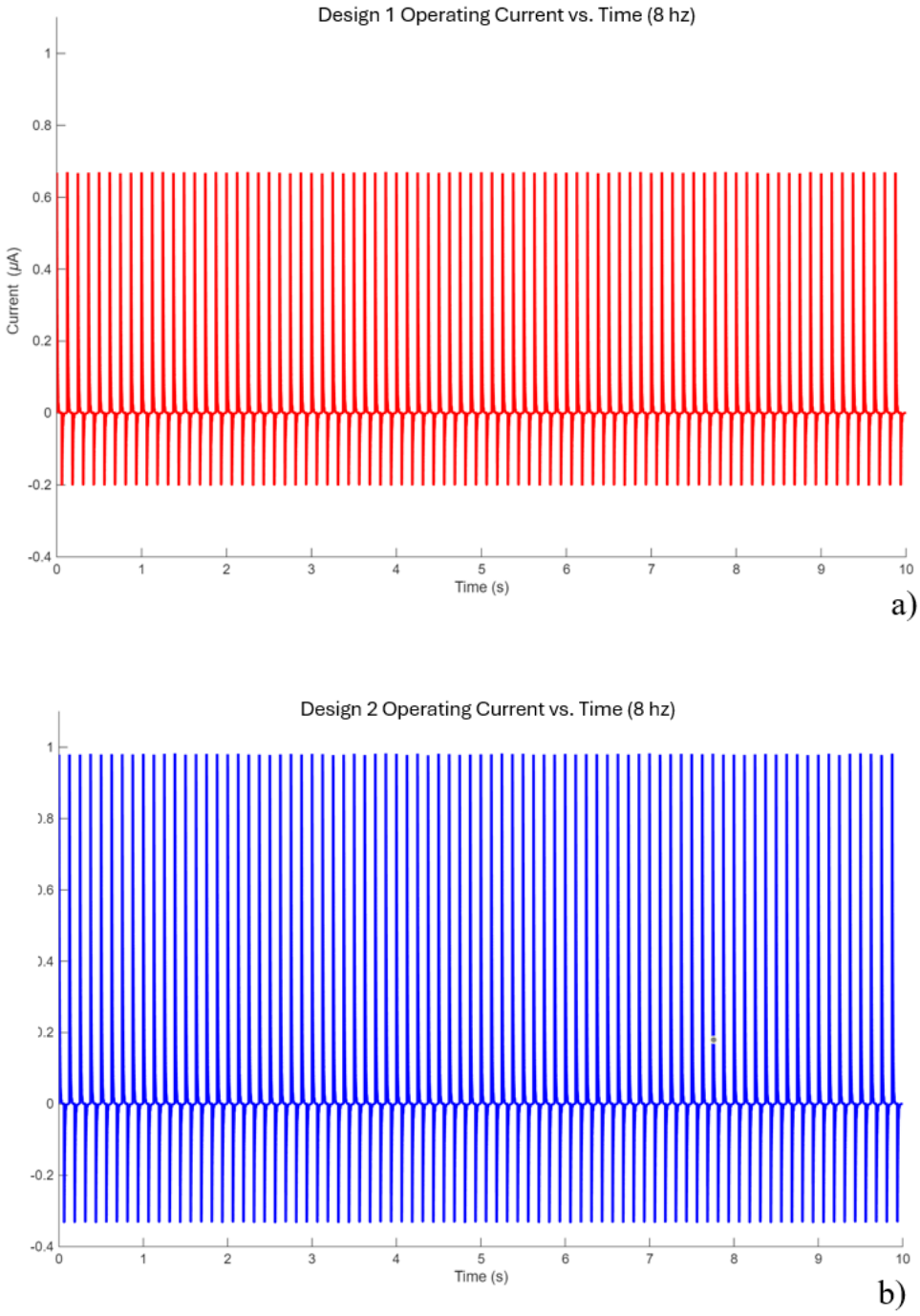

Figure 86: Operating current at 10 MΩ and 8 Hz a) Design 1 b) Design 2

Similar to I_{sc}, the output current is influenced by both the charge accumulated on the triboelectric layers and the rate of mechanical excitation. Design 2 produced higher output currents than Design 1 across all frequencies, consistent with its higher V_{oc}, I_{sc}, and Q_{sc}. The improved performance can again be attributed to the Cu bond coat, which promotes more efficient charge accumulation on the PFA layer and minimizes opposing electric field effects.

Both designs showed repeatable current waveforms over multiple cycles, indicating minimal influence of dielectric relaxation or leakage under the selected load and operating conditions. These measurements confirm that the enhanced electrical performance of Design 2 observed in V_{oc}, I_{sc}, and Q_{sc} translates directly into higher practical output under typical circuit loading conditions.

6.2.6 Power Output

The power output of a TENG represents the electrical power generated that can be delivered to a system during operation.

Experimentally, the output voltage and current were measured by using a circuit and attaching external loads by substituting resistors from 100 kΩ being the lowest to the load of the electrometer of 200 MΩ, all while keeping the separation distance at 2.50 mm and using an operating frequency of 6 Hz. The instantaneous power was calculated at each point, defined using Ohm's law,

$$P = \frac{V^2}{R}$$

and the external load where maximum power output occurred was identified. This allows determination of the load condition under which the TENG can deliver its highest power, necessary for practical applications and operational conditions for use as an energy harvesting or powering low frequency electric devices. The relationships between voltage, current, external resistance, and power for both designs are shown in Figure 87 and Figure 88.

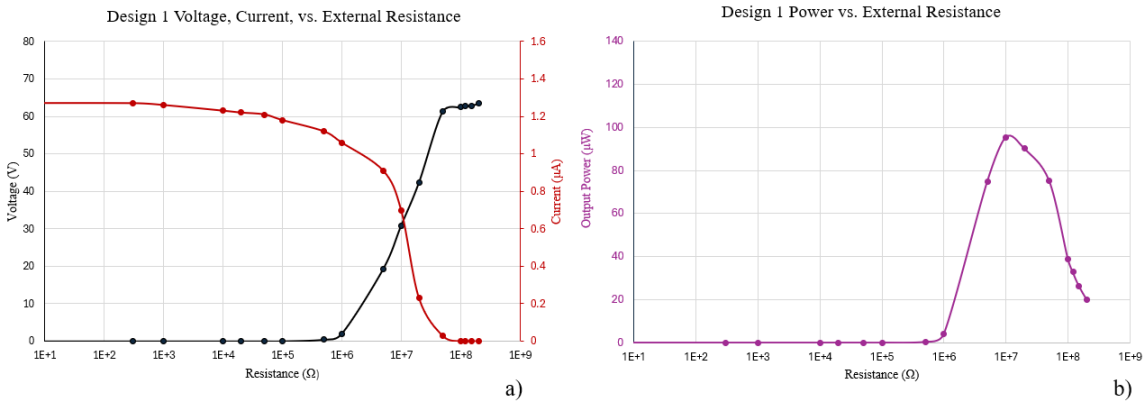

Figure 87: Design 1 a) voltage, current, vs external resistance b) power vs external resistance

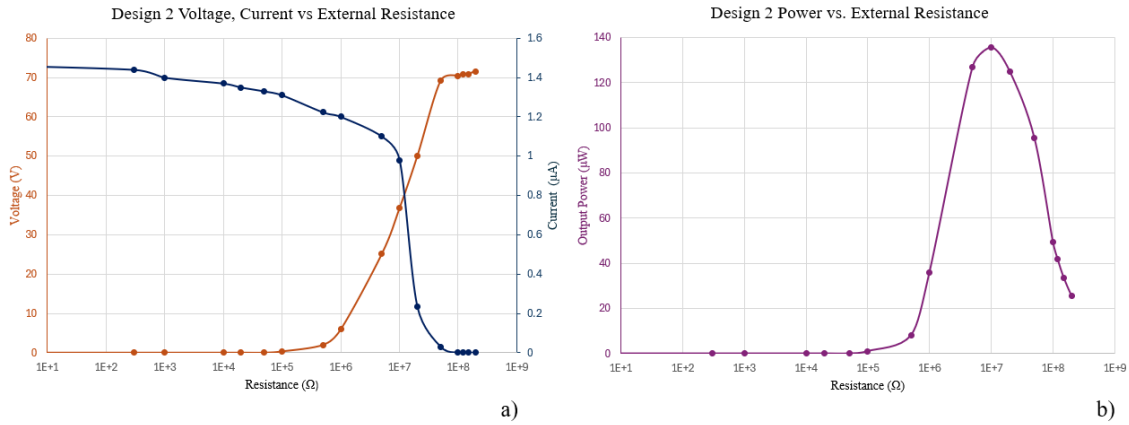

Figure 88: Design 2 a) voltage, current, vs external resistance b) power vs external resistance

Design 2 was consistently producing higher maximum power than Design 1, reaching 137 μW compared to 98 μW. Both peak powers occurred at an external load resistance of 10 MΩ. The observation on power is consistent with the trends observed in V_{oc}, I_{sc}, and Q_{sc}, and reflects the enhanced charge transfer facilitated by the Cu bond coat. The combination of higher voltage and higher current in Design 2 results in a combined effect on power.

Both designs also exhibited repeatable power output over multiple cycles, indicating stable operation and minimal losses over the typical periods exposed to.

6.2.7 Conversion Efficiencies

The energy conversion efficiencies for the ideal TENG cycle were derived in Chapter 3.1.6 and can now be used as the values of V_{oc} and V' have been determined experimentally.

Using equation 44, the efficiency of Design 1 and Design 2 are 96.13% and 96.24%, respectively. These values although appearing high are expected for VS-TENGs as they have high rates of conversion efficiency.

VS-TENGs are known for their remarkably high energy conversion efficiency, often reaching values above 90% under ideal conditions. The high efficiency comes from how mechanical work is converted directly into electrical energy through the triboelectric effect.

A key point in understanding the efficiency of VS-TENGs is distinguishing between the total mechanical work applied to the system and the work that is harvested as electricity. Not all the mechanical input contributes to current generation. Some energy is lost to material deformation, surface vibrations, and damping in the air, while a fraction remains stored temporarily as electrostatic potential without immediately being converted to current. Despite these losses, most of the work done in the separation phase is captured as electrical energy because the electrostatic forces scale with the surface charge density and separation distance. The TENG coupled with the triboelectric effect is designed to maximize the proportion of input work that directly produces a voltage difference and drives charge flow in the external load.

Another factor contributing to VS-TENG efficiency is their design for low-frequency, small-amplitude mechanical inputs. Unlike conventional generators or turbines, which are designed to extract energy from high-speed, high-force sources, VS-TENGs are optimized to harvest ambient energy from sources such as human motion, footsteps, vehicle vibrations, or passing trains. The energy available in these scenarios is relatively small, and the TENG can operate effectively because it does not require large-scale mechanical infrastructure. Its simplicity in converting localized mechanical deformation into electricity allows the device to function efficiently even when forces are intermittent and low in magnitude.

The vertical contact-separation mode additionally reduces losses associated with lateral motion or friction. This contrasts with lateral sliding TENGs, where some input energy is dissipated as heat through frictional sliding, the vertical mode ensures that the energy spent on moving the surfaces apart is mostly recovered as electrical energy. The efficiency can thus be interpreted as the ratio of harvested electrical work to the mechanical work required to charge and discharge the TENG surfaces, rather than to the total mechanical force applied.

6.2.8 Comparative Performances Between Designs

While individual measurements of V_{oc}, I_{sc}, Q_{sc}, and power output provide insight into the operating characteristics of each TENG, the most meaningful evaluation comes from comparing these parameters together. Design 2 consistently outperformed Design 1 across all metrics, demonstrating higher V_{oc}, greater I_{sc}, larger Q_{sc}, and better power density under identical testing conditions. This suggests that the modifications incorporated into Design 2, mainly from the direct CS deposition of PFA on the Cu bondcoat allowed for significant electrical performance enhancements.

The consistent trends observed across Q_{sc}, V_{oc}, and I_{sc} further validate that Design 2 can reach a higher steady-state charge balance, which translates into improved charge transfer dynamics and thus greater usable output. Moreover, the superior power output measured under matched load resistance confirms that Design 2 not only generates more charge but also converts it into usable electrical energy more efficiently. In practice, this comparative advantage makes Design 2 a more robust and scalable design for future applications, where both maximized energy harvesting and reliable electrical performance are essential.

6.3 Durability and Wear

To evaluate both the durability of the TENG devices and the wear resistance of the deposited coatings, the samples were subjected to 6000 consecutive cycles of vertical contact-separation motion. This cycling procedure not only simulates sustained operational use of the TENGs but also provides a measure of how well the PFA and aluminum layers withstand repeated mechanical contact without significant degradation. After cycling, the electrical performance of the TENGs was re-tested and compared with the initial measurements to assess changes in output. By linking device performance with coating

integrity, this analysis highlights the importance of material robustness and interfacial stability in ensuring long-term reliability. All the re-tested electrical properties including V_{oc}, Q_{sc}, I_{sc}, operating voltage V, and operating current I,are shown from Figures 89 to 93. Table 5 summarizes all the average values of the measured properties.

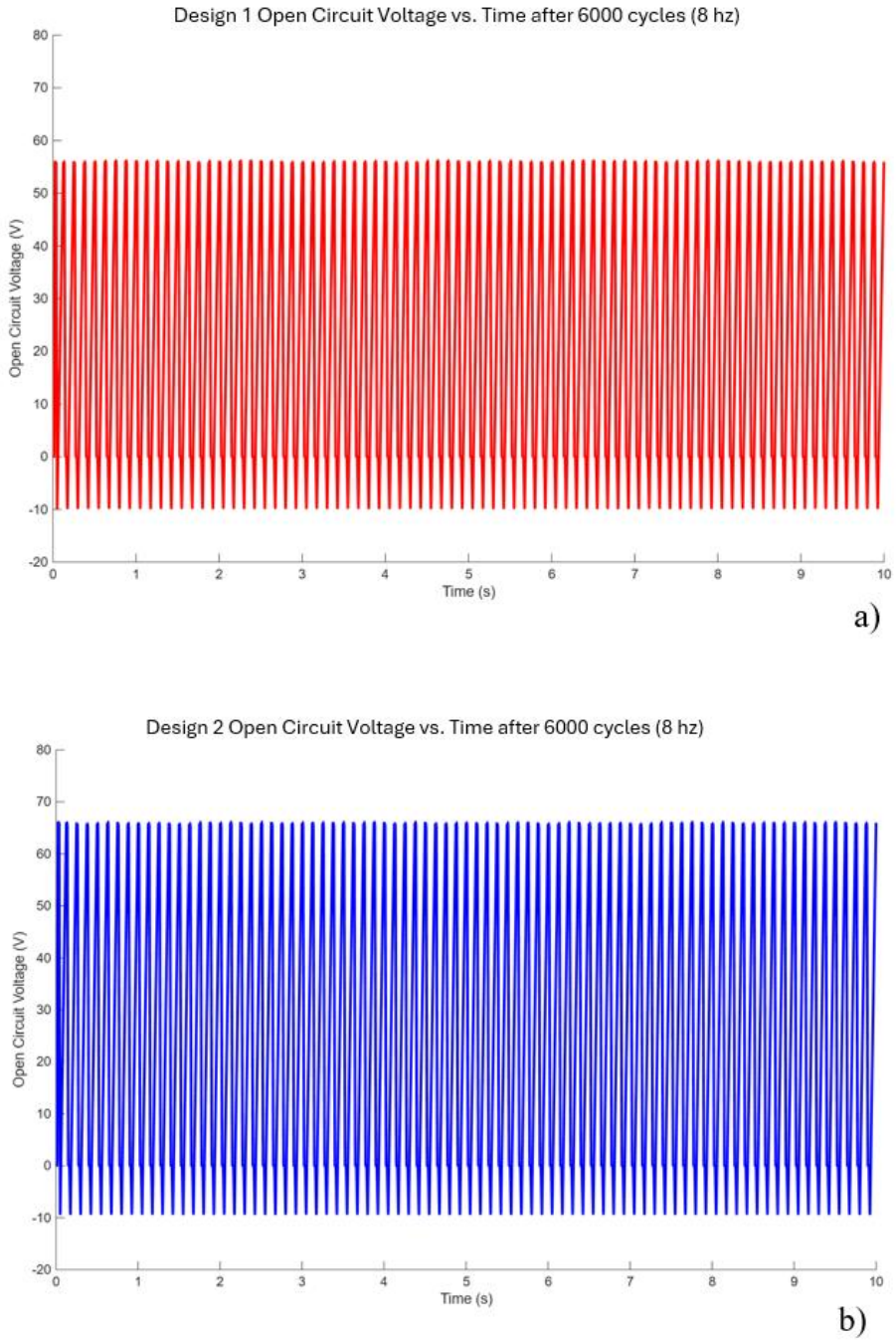

Figure 89: Open circuit voltage after 6000 cycles a) Design 1 b) Design 2

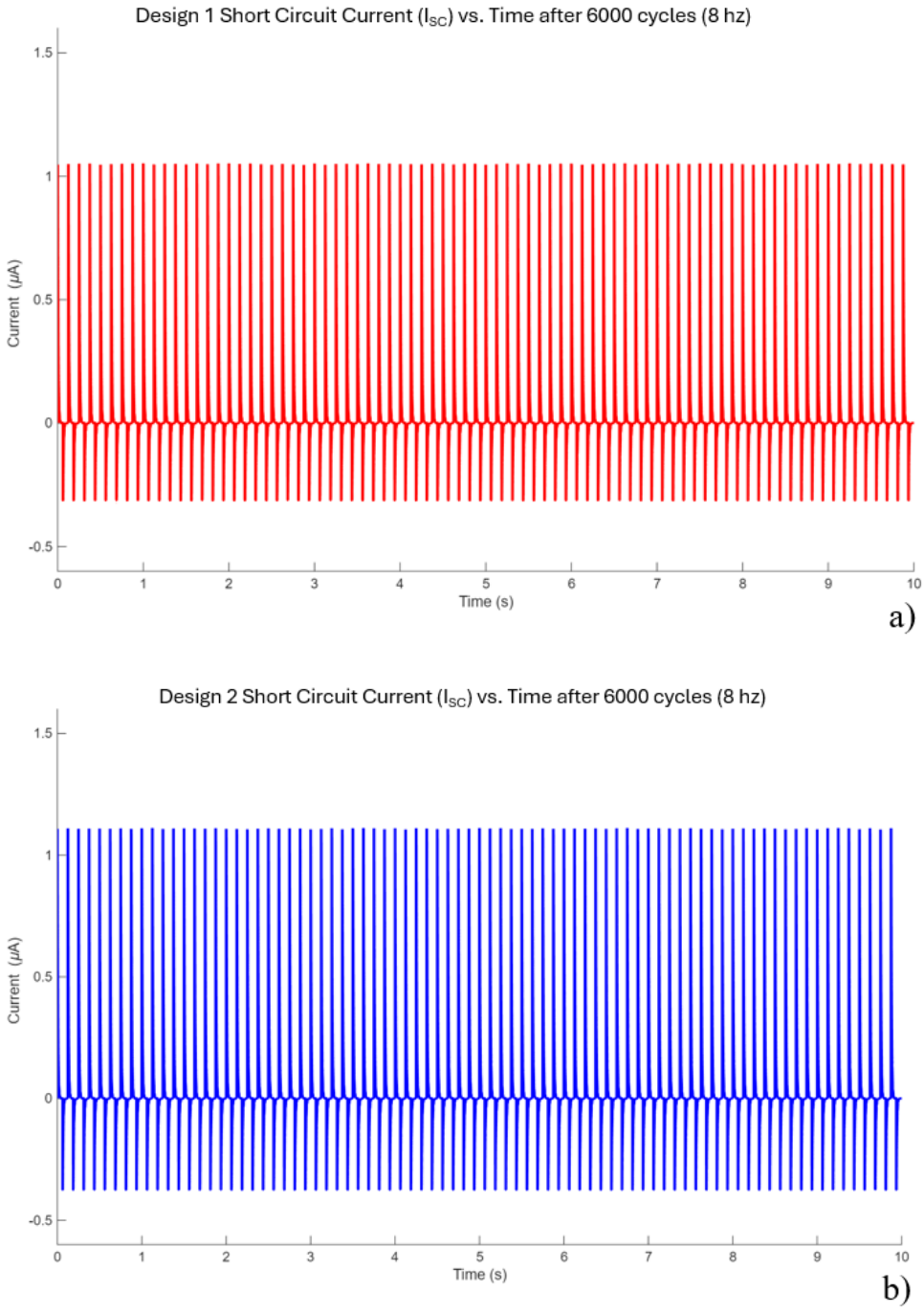

Figure 90: Short circuit current after 6000 cycles a) Design 1 b) Design 2

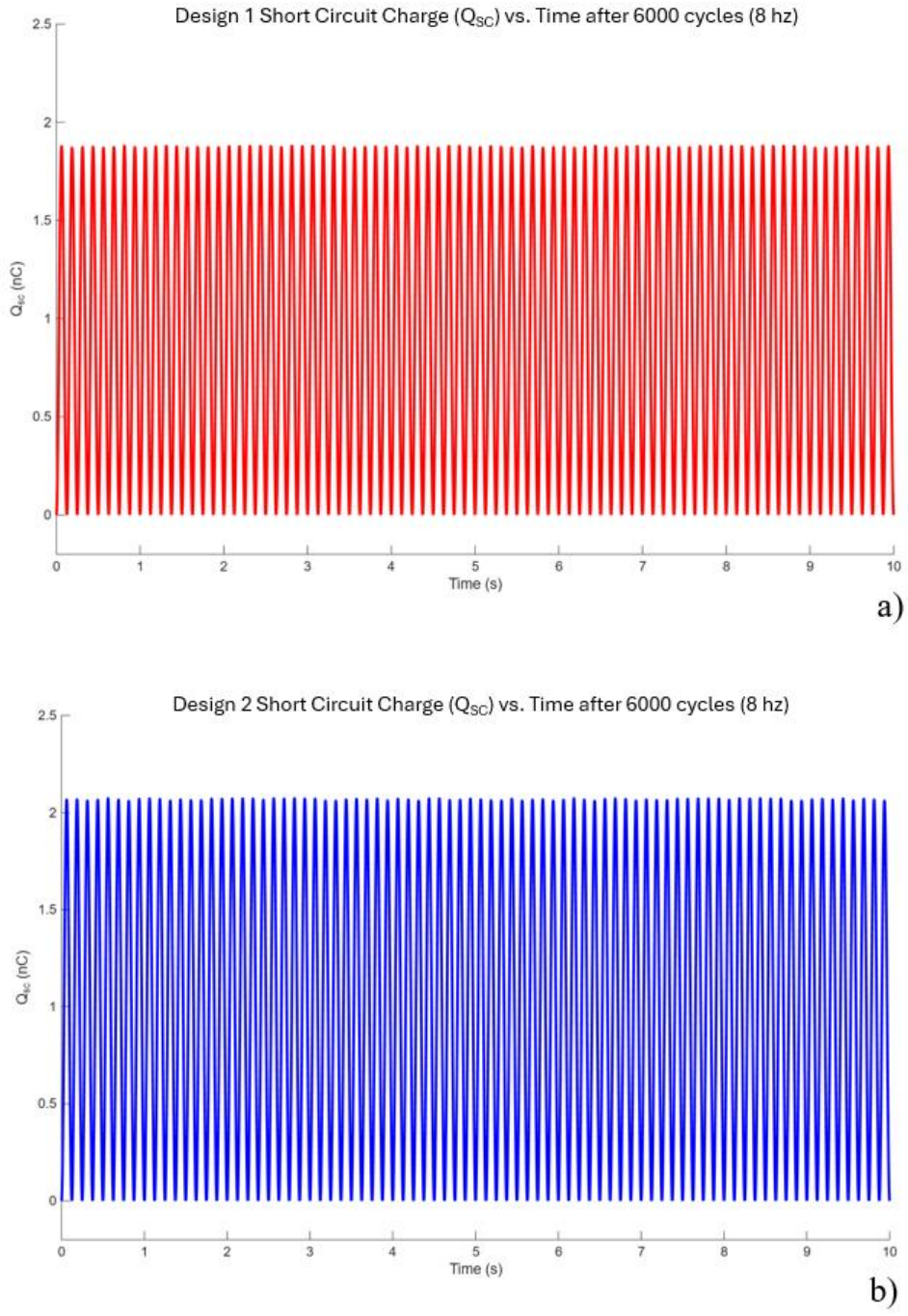

Figure 91: Short circuit charge after 6000 cycles a) Design 1 b) Design 2

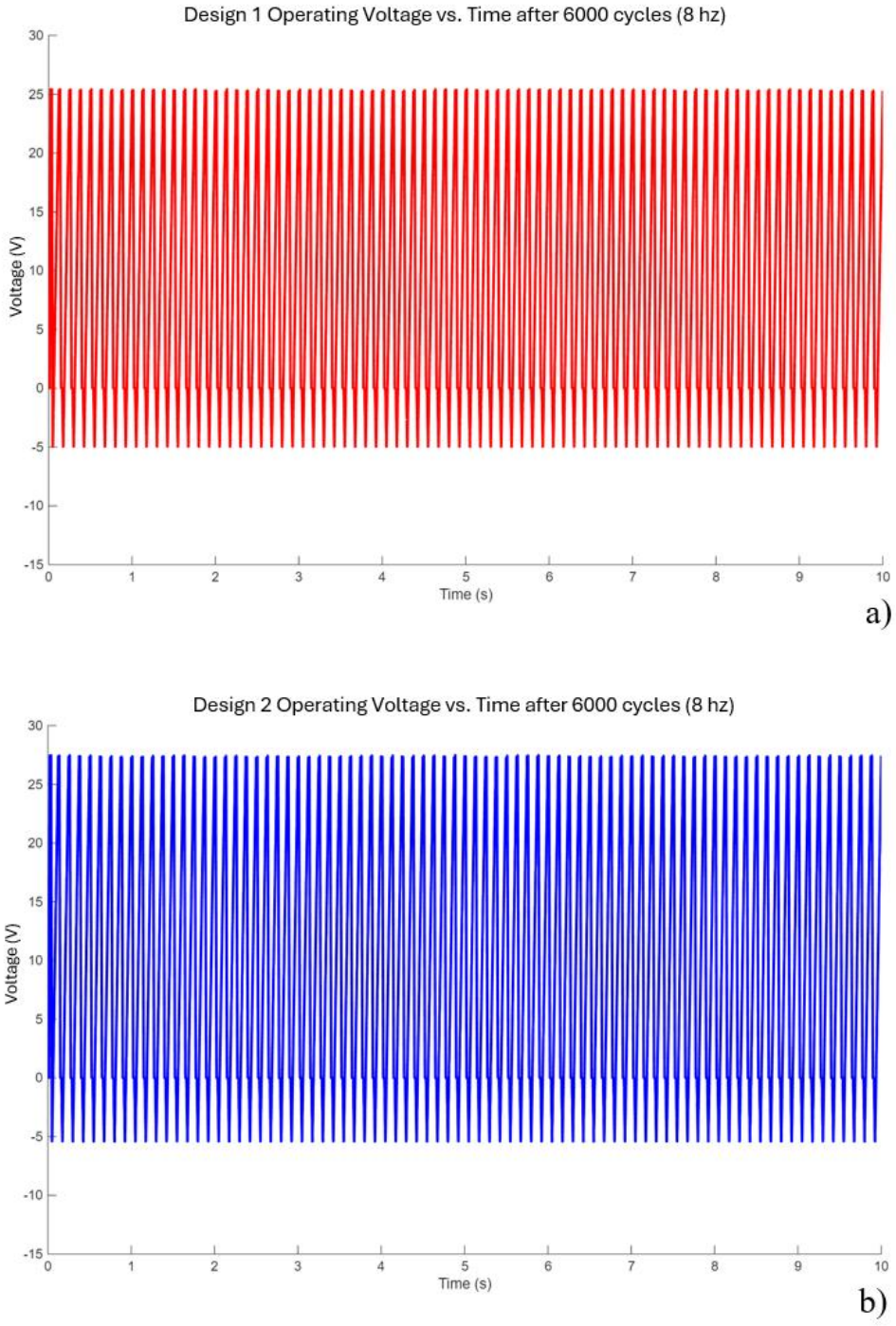

Figure 92: Operating voltage after 6000 cycles a) Design 1 b) Design 2

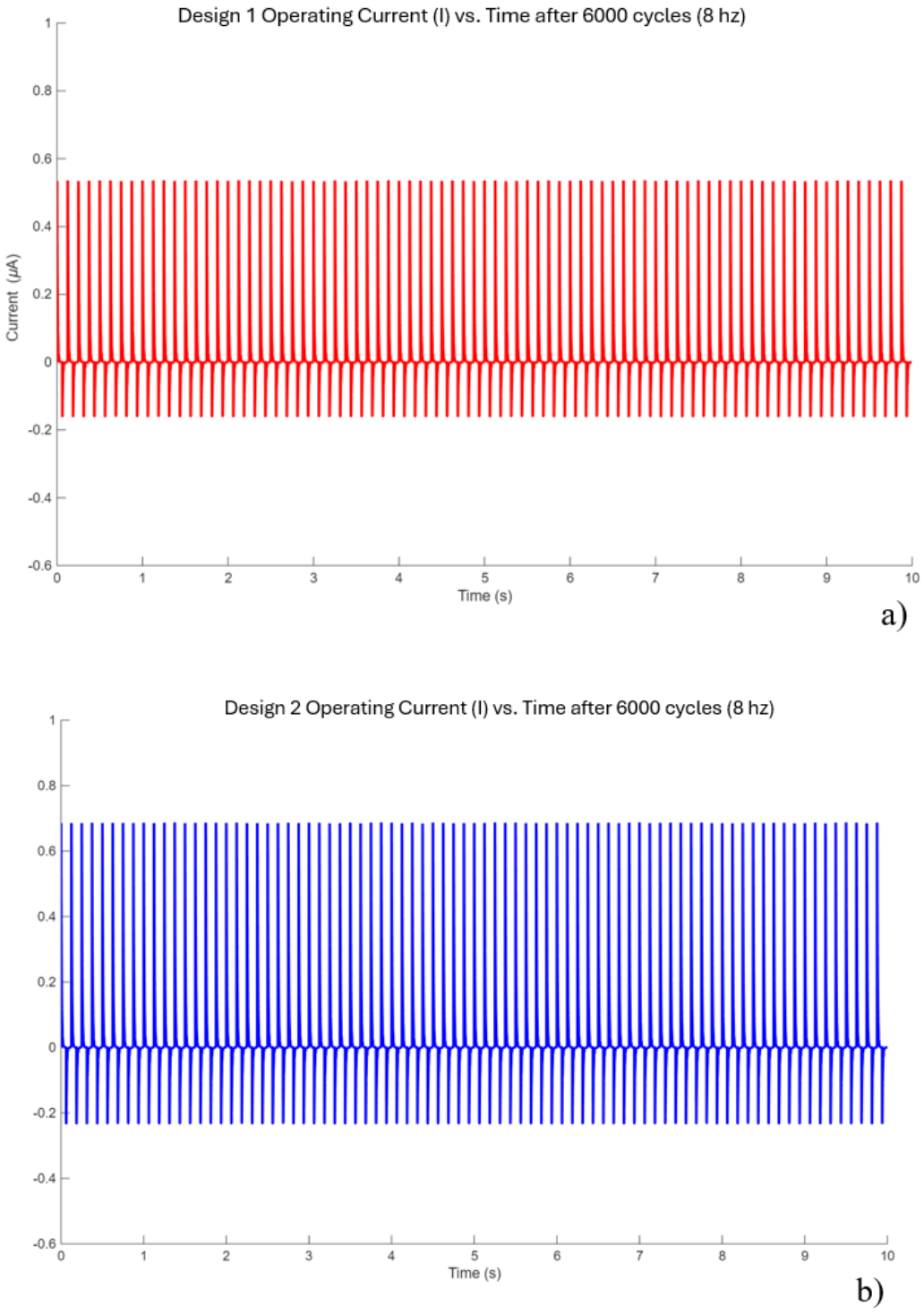

Figure 93: Operating current after 6000 cycles a) Design 1 b) Design 2

Table 5: Measured electrical properties before and after cycling

Property	Measured Value Before Testing		Measured Value After 6000 Cycles		Percent Drop	
	Design 1	Design 2	Design 1	Design 2	Design 1	Design 2
V_{oc} (V)	63.42	71.32	56.98	65.87	10.15%	7.64%
Q_{sc} (nC)	2.34	2.80	1.87	2.06	20.09%	26.43%
I_{sc} (µA)	1.31	1.48	1.05	1.11	19.85%	25.00%
V (V)	31.27	36.83	25.36	27.44	18.90%	29.35%
V'(V)	-6.15	-7.14	-4.95	-5.42	19.51%	26.86%
η(%)	96.13	96.24	96.20	96.01	0.07%	0.25%
I (µA)	0.691	0.971	0.544	0.686	21.27%	29.35%
P (µW)	95.48	135.60	64.31	75.295	32.66%	44.47%

The results presented in Table 5 provide a direct comparison between the two TENG designs before testing and after 6000 operation cycles. Design 2 initially exhibits higher performance across all measured parameters, including open-circuit voltage, transferred charge, short-circuit current, load current, and power output. Before testing, Design 2 delivers a maximum power of 135.6 µW compared to 95.5 µW for Design 1. This shows that Design 2 benefits from a more favourable charge transfer process and more efficient electrode interactions in its initial state, which enhances its energy conversion efficiency.

However, durability testing reveals that Design 1 maintains a greater portion of its performance after extended cycling. While both designs undergo degradation, the percent drop for Design 1 remains consistently lower than that of Design 2.

These differences can be attributed to the choice of bond coat materials for the PFA coating, as Al was used as the tribopositive material sprayed directly onto a Cu coating. Al was used as the bond coat for Design 1, providing strong adhesion for the PFA layer and improving long-term durability, whereas Copper served as the bond coat for Design 2, which offered less robust bonding but better initial electrical performance. The decrease in V_{oc} is 10.15% for Design 1 compared to 7.64% for Design 2, but for more critical output parameters such

as transferred charge, current, and power, Design 1 retains 67–80% of its original values, whereas Design 2 retains only 55–75%. The most pronounced difference appears in the maximum power output, where Design 1 shows a 32.7% decline, while Design 2 experiences a substantially larger 44.5% drop. After 6000 cycles, the power outputs of both designs become almost comparable, underscoring the superior durability of Design 1.

In addition to the previously reported parameters, the voltage on the negative, V', along with the conversion efficiency were also evaluated. While both V' and the conventional voltage measurements show the expected degradation over 6000 cycles, being 19.51% for Design 1 and 26.86% for Design 2, the energy conversion efficiency remains remarkably stable at approximately 96% for both designs, with no observable drop. This suggests that the mechanisms responsible for energy loss in these TENG such as charge leakage, or incomplete charge transfer are minimal and largely unaffected by surface wear or material fatigue. The consistency of the efficiency indicates that, despite a reduction in the major output values from degradation of the electrodes or triboelectric layers, the proportion of input mechanical energy converted into electrical energy remains effectively unchanged.

SEM analysis of the deposited coatings revealed the presence of microcracks at the interface between the triboelectric layer and the substrate. These are shown for each coating in Figure 94 to Figure 96.

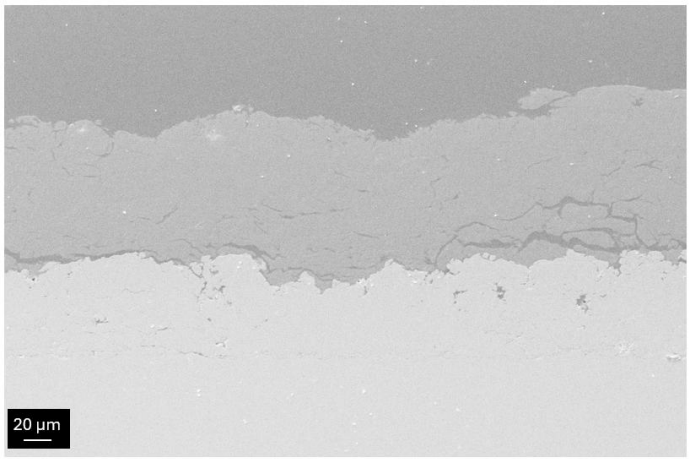

Figure 94: PFA coating on Cu bond coat after 6000 cycles

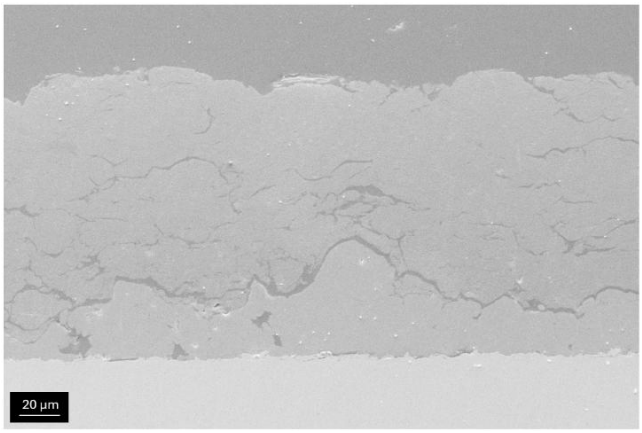

Figure 95: PFA coating on Al bond coat after 6000 cycles

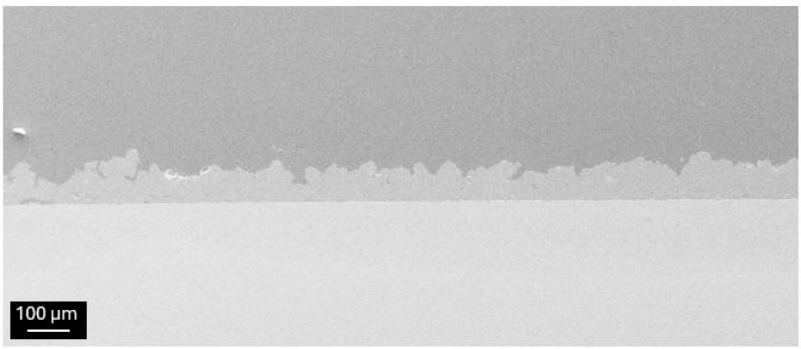

Figure 96: Al coating on Cu substrate after 6000 cycles

After 6000 cycles, heavy flaking and cracks were observed on PFA coatings for both Cu and Al and delamination in areas of the coating were observed under SEM. The Al and Cu coatings show no changes in their structures, and this is likely due to the much higher hardness of the metal coatings compared to the polymer PFA.

These cracks likely play a role in the observed voltage drops during TENG operation. Mechanically, cracks reduce the effective contact area between the triboelectric layer and the opposing electrode, which limits the charge transfer during the contact-separation cycle. Electrically, cracks can introduce localized regions of poor capacitance or incomplete charge transfer, effectively acting as micro-scale barriers that dissipate, do not withhold, or redistribute surface charges. Over repeated cycles, the formation and propagation of these cracks may worsen, further reducing the TENG's output voltage and overall efficiency. This observation shows that durability is not just about layer adhesion

or bulk mechanical stability but also about maintaining a continuous, crack-free interface which ensures consistent electrical performance over the lifetime of the device.

These results highlight an important trade-off between initial performance and long-term reliability. Design 2 is more efficient at the outset, but its material selection renders it more susceptible to fatigue, surface degradation, or charge trapping effects over repeated contact–separation cycles. In contrast, Design 1 may be less optimized for initial peak performance but demonstrates greater resilience because of the aluminum bond coat, making it more suitable for long-term applications where consistent power delivery is critical. This durability advantage suggests that Design 1 could provide more stable output in practical scenarios, especially for devices requiring prolonged reliability without frequent replacement.

6.4 Limitations in Nylon Spray

During attempts to spray Nylon 6 powder, reliable feeding proved nearly impossible despite extensive parameter adjustments. The powder, with a particle size distribution of 15 – 35 μm, exhibited highly cohesive behavior and resisted all attempts to assimilate into the gas stream. This can be attributed to several fundamental factors. Initial tests using the conventional CS setup led to no feeding, even when toggling pressure and temperature values. Because of the low melting point of Nylon 6 of 220 °C, temperature could not have been adjusted such that the stagnation temperature exceeded the melting temperature. Adjusting the pressure additionally led to no feeding. The polymer CS setup was employed as an alternative method, but the feeding pressure now was limited to a maximum of 60 psi and a minimum of 40 psi from how the equipment was designed prior. The attempted spray parameters are shown in Table 6.

Table 6: Nylon 6 spray parameters

Temperature (°C)	**Stagnation Pressure (psi)**	**Nozzle Type**	**Substrate Preheater Temperature (°C)**	**Spray Success (Yes/No)**
200	100	Converging-diverging	N/A	No
200	200	Converging-diverging	150	No
220	200	Converging-diverging	150	No
220	60	Straight Section	150	No
240	60	Straight Section	150	No

Nylon is hygroscopic and readily absorbs ambient moisture, which makes the particles sticky and prone to agglomeration. When heated near its melting point, the material can begin to soften and sinter, further encouraging bridging within the feed system. The particle size range itself is problematic, as it lies in a regime where van der Waals forces, electrostatic charging, and acquiring condensation, makes the powder difficult to fluidize. In addition, Nylon particles are light and charge easily, adhering to canister walls and tubing surfaces even when switching from rubber to steel hoses. From a flow standpoint, flow assimilation was further limited by pressure mismatches: the injector gas stream

required higher momentum to achieve the 30 scfh feed rate experimentally determined to fluidize polymers, yet this flow was not sustained because of the sticky nature of the powder. This may have caused pressure drops and local flow disturbances at the injection point.

Based on these challenges, several initial recommendations can be made from a fluid dynamics perspective. First, proper drying of Nylon powder is essential, but the drying should occur externally in a controlled oven or desiccant system at moderate temperatures (80–100 °C) to avoid approaching the softening point. After heating, cooling and storage under dry nitrogen or a moisture free environment to minimize reabsorption. Drying at temperatures approaching the melting point should be avoided, as it promotes sintering and exacerbates sticking.

Additionally, careful attention should be given to electrostatic effects by grounding all metallic components. The use of a surfactant can be applied here if possible. Flow path optimization by shortening and straightening tubing and increasing its diameter would further reduce frictional and electrostatic losses that hindered powder transport. From a material perspective, adjusting the particle size distribution to remove excess fines or employing minor flow aids could improve cohesion, though this would require evaluation for compatibility with the intended coating application. For example, in TENGs this may not be beneficial, as the addition of foreign material may hinder electric predictions and characterization. Using vibration at the feeder and around the hose to further agitate the powder could also be beneficial to powder flowing.

If possible, the powder feeder itself should be reconsidered for cohesive polymers. A mechanism incorporating a porous distributor to introduce carrier gas evenly beneath the powder, would help disrupt agglomerates and maintain a stable, aerated bed. This approach is commonly applied in pneumatic conveying of fine and cohesive powders and is more reliable than relying solely on mechanical vibration or feed-wheel modifications.

Electrostatic charging is another factor that must be eliminated or mitigated. Nylon readily accumulates charge through frictional contact, which leads to adhesion on feeder walls and hoses. Grounding all metallic components, replacing insulating connections with conductive alternatives, and potentially incorporating ionizing devices at both the powder

injection point in the hose and the nozzle inlet would help neutralize charge buildup. Additionally, simplifying the feed pathway using short, straight, and wider-diameter tubing would reduce frictional resistance and particle-wall interactions, improving transport efficiency.

Finally, materials-based modifications may offer longer term solutions. Adjusting the particle size distribution, such as removing excessive fines or using powders with slightly larger mean diameters, could improve flowability by reducing cohesive forces. Alternatively, the use of flow aids or surface treatments such as adding hard additives such as silica or alumina particles, or treatment by means of a surfactant might mitigate sticking and improve fluidity, mechanically and physically. This would pose design challenges as additives would need to be carefully evaluated prior for compatibility with coating adhesion and final desired material properties. For example, in the case of TENGs this may not be beneficial, as the addition of foreign materials may make electric predictions and characterization more difficult. Using vibration at the feeder and around the hose to further agitate the powder could also be beneficial to powder flowing.

In summary, the difficulties encountered in feeding Nylon 6 powders are consistent with known challenges of handling cohesive, hygroscopic polymers. Addressing these issues will likely require a combination of powder pre-conditioning, modifications to the feeder design, improved feeding strategies, and consideration of electrostatic and particle-size effects. Future work should focus on systematically testing these approaches, beginning with controlled powder drying and fluidized-bed feeding, before progressing to injector redesign and mechanical assistance. These issues should be addressed prior to beginning any additional feeding or spray work. The nylon powder clogging the canister after a spray trial is shown in Figure 97.

Figure 97: Nylon 6 powder sticking to the canister liner

7 CONCLUSIONS AND FUTURE WORK

This thesis presented the design, fabrication, and performance evaluation of vertical contact-separation triboelectric nanogenerators (VS-TENGs) using CS as the manufacturing process. The study demonstrates that CS can successfully produce triboelectric layers, enabling high energy conversion efficiencies of up to 96%. By selecting PFA as the tribonegative layer, Al as the tribopositive layer, and Cu as the electrode and substrate materials, the VS-TENGs could effectively convert nearly all work associated with surface charging and discharging into electrical energy, minimizing mechanical losses and showing good electrical output. Initial readings of V_{oc} were high, but current output was still low, and the subsequent power was below average of those found in the literature. At best, these devices could power a self powered switch or charge a capacitor for use in a charging circuit. The governing principles of charge transfer, electric field variation, and current generation were analyzed to understand and optimize each stage of the TENG operating cycle and experimental results agreed with the foundational principles of the underlying theories.

CS allowed for successful deposition of PFA on Al and Cu substrates as the primary novelty, with good initial adhesion and minimal surface damage. Wear testing by repeatedly engaging the TENG layers showed a significant drop of electrical performance as the adhesion of PFA directly to Cu was poor. Durability testing revealed that both material choice and deposition parameters significantly influence long term performance under repeated mechanical cycling, emphasizing the importance of stable triboelectric interfaces for reliable operation. Attempts to replace Al with Nylon 6 were unsuccessful due to poor powder flow and the presence of cohesiveness in the feedstock. This highlights current limitations in polymer CS for TENG fabrication and points to opportunities for improved deposition strategies.

Future work should focus on enhancing both adhesion and long term viability of the triboelectric layers. Techniques such as surface texturing, masked deposition to increase contact area, or optimized CS parameters for polymers could improve energy harvesting performance. The effect of surface area should also be analyzed, as an overall rough area does increase the available surface area, it does not necessarily directly increase the true

contact area because of potential inconsistencies in surface roughness and morphology. As the PFA coating performed better mechanically than electrically when sprayed on the Al bond coat than on the Cu bond coat, an investigation should be made to determine if charge transfer and the triboelectric effect is present as a viable bonding mechanism. Additionally, exploring alternative triboelectric material pairings with superior electrical and mechanical properties may yield higher output and improved stability. Addressing these challenges will be essential for advancing VS-TENGs from laboratory prototypes to practical, long-lasting energy harvesting devices suitable for self-powered sensors and electronics.

REFERENCES

[1] F. Yildiz, “Potential Ambient Energy-Harvesting Sources and Techniques”, Journal of Technology Studies, vol. 35, no. 1, p. 40-48, 2009, doi: None.

[2] Hassan Askari, Amir Khajepour, Mir Behrad Khamesee, Zia Saadatnia, Zhong Lin Wang, Piezoelectric and triboelectric nanogenerators: Trends and impacts, Nano Today Volume 22, 2018, Pages 10-13, ISSN 1748-0132, https://doi.org/10.1016/j.nantod.2018.08.001.

[3] Guang Zhu, Bai Peng, Jun Chen, Qingshen Jing, Zhong Lin Wang, Triboelectric nanogenerators as a new energy technology: From fundamentals, devices, to applications, Nano Energy, Volume 14, 2015, Pages 126-138, ISSN 2211-2855, https://doi.org/10.1016/j.nanoen.2014.11.050.

[4] Wang, Zhong Lin, et al. Triboelectric Nanogenerators. 1st ed. 2016., Springer International Publishing, 2016, https://doi.org/10.1007/978-3-319-40039-6.

[5] Fauchais, Pierre, and Ghislain Montavon. “Thermal and Cold Spray: Recent Developments.” Key Engineering Materials, vol. 384, Trans Tech Publications, Ltd., p. 1–59. 2008 doi:10.4028/www.scientific.net/kem.384.1.

[6] Razavipour, M., Rahmati, S., Zúñiga, A. et al. Bonding Mechanisms in Cold Spray: Influence of Surface Oxidation During Powder Storage. J Therm Spray Tech 30, 304–323 (2021). https://doi.org/10.1007/s11666-020-01123-5

[7] Cavaliere, P., Silvello, A. Crack Repair in Aerospace Aluminum Alloy Panels by Cold Spray. J Therm Spray Tech 26, 661–670 (2017). https://doi.org/10.1007/s11666-017-0534-9

[8] AL-Mangour, B., Vo, P., Mongrain, R. et al. Effect of Heat Treatment on the Microstructure and Mechanical Properties of Stainless Steel 316L Coatings Produced by Cold Spray for Biomedical Applications. J Therm Spray Tech 23, 641–652 (2014). https://doi.org/10.1007/s11666-013-0053-2

[9] Shuo Yin, Pasquale Cavaliere, Barry Aldwell, Richard Jenkins, Hanlin Liao, Wenya Li, Rocco Lupoi, Cold spray additive manufacturing and repair: Fundamentals and applications, Additive Manufacturing, Volume 21, 2018, Pages 628-650, ISSN 2214-8604, https://doi.org/10.1016/j.addma.2018.04.017.

[10] Gärtner, F., Stoltenhoff, T., Schmidt, T. et al. The cold spray process and its potential for industrial applications. J Therm Spray Tech 15, 223–232 (2006). https://doi.org/10.1361/105996306X108110

[11] Yang Yu, Hengyu Li, Da Zhao, Qi Gao, Xiang Li, Jianlong Wang, Zhong Lin Wang, Tinghai Cheng, Material’s selection rules for high performance triboelectric nanogenerators, Materials Today, Volume 64, 2023, Pages 61-71, ISSN 1369-7021, https://doi.org/10.1016/j.mattod.2023.03.008.

[12] Ankan Paul, Chaitanya S. Wannere, Veronica Kasalova Paul v. R. Schleyer, Henry F. Schaefer The Peculiar Trend of Cyclic Perfluoroalkane Electron Affinities with Increasing Ring Size J. Am. Chem. Soc. 2005, 127, 44, 15457–15469 https://doi.org/10.1021/ja053310w

[13] E. Leivo, T. Wilenius, T. Kinos, P. Vuoristo, T. Mäntylä, Properties of thermally sprayed fluoropolymer PVDF, ECTFE, PFA and FEP coatings, Progress in Organic Coatings, Volume 49, Issue 1, 2004, Pages 69-73, ISSN 0300-9440, https://doi.org/10.1016/j.porgcoat.2003.08.011.

[14] Zhang, D., Shipway, P.H. & McCartney, D.G. Cold gas dynamic spraying of aluminum: The role of substrate characteristics in deposit formation. J Therm Spray Tech 14, 109–116 (2005). https://doi.org/10.1361/10599630522666

[15] Weixu Yang, Xiaoli Wang, Ping Chen, Yanqiang Hu, Lizhou Li, Zhen Sun, On the controlled adhesive contact and electrical performance of vertical contact-separation mode triboelectric nanogenerators with micro-grooved surfaces, Nano Energy, Volume 85, 2021, 106037, ISSN 2211-2855, https://doi.org/10.1016/j.nanoen.2021.106037.

[16] Sihong Wang, Long Lin, Zhong Lin Wang, Triboelectric nanogenerators as self-powered active sensors, Nano Energy, Volume 11, 2015, Pages 436-462, ISSN 2211-2855, https://doi.org/10.1016/j.nanoen.2014.10.034.

[17] Pan, S., Zhang, Z. Fundamental theories and basic principles of triboelectric effect: A review. Friction 7, 2–17 (2019). https://doi.org/10.1007/s40544-018-0217-7

[18] Benjamin, Park. A History of Electricity (the Intellectual Rise in Electricity) from Antiquity to the Days of Benjamin Franklin. J. Wiley, 1898, https://www.biodiversitylibrary.org/page/17835084.

[19] Pan, Shuaihang, and Zhinan Zhang. "Triboelectric effect: A new perspective on electron transfer process." Journal of Applied Physics 122.14 (2017), https://doi.org/10.1063/1.5006634

[20] C. Xu, Y. Zi, A. C. Wang, H. Zou, Y. Dai, X. He, P. Wang, Y.-C. Wang, P. Feng, D. Li, Z. L. Wang, On the Electron-Transfer Mechanism in the Contact-Electrification Effect Adv. Mater. 2018, 30, 1706790. https://doi.org/10.1002/adma.201706790

[21] E. N. Jayaweera, K. Rohana Wijewardhana, Thilini K. Ekanayaka, Amir Shahzad, and Jang-Kun Song ACS Sustainable Chemistry & Engineering 2018 6 (5), 6321-6327 doi: https://doi.org/10.1021/acssuschemeng.8b00136

[22] https://www.science-sparks.com/a-hair-raising-experiment/

[23] Z. L. Wang, Triboelectric Nanogenerator (TENG)—Sparking an Energy and Sensor Revolution. Adv. Energy Mater. 2020, 10, 2000137. https://doi.org/10.1002/aenm.202000137

[24] Yang Xu, Guanbo Min, Nikolaj Gadegaard, Ravinder Dahiya, Daniel M. Mulvihill, A unified contact force-dependent model for triboelectric nanogenerators accounting for surface roughness, Nano Energy, Volume 76, 2020, 105067, ISSN 2211-2855, doi: https://doi.org/10.1016/j.nanoen.2020.105067.

[25] Dan Yang, Yufeng Ni, Xinxin Kong, Shuyao Li, Xiangyu Chen, Liqun Zhang, and Zhong Lin Wang, Self-Healing and Elastic Triboelectric Nanogenerators for Muscle Motion Monitoring and Photothermal Treatment, ACS Nano 2021 15 (9), 14653-14661 doi: https://doi.org/10.1021/acsnano.1c04384

[26] Z. Lin, B. Zhang, Y. Xie, Z. Wu, J. Yang, Z. L. Wang, Elastic-Connection and Soft-Contact Triboelectric Nanogenerator with Superior Durability and Efficiency. Adv. Funct. Mater. 2021, 31, 2105237. https://doi.org/10.1002/adfm.202105237

[27] Lingyi Liao, Qingsong Mei, Juying Li, Zihao Chen, Yuqi Peng, Lufei Bai, Microstructure dependence of the triboelectric behavior of metals, Chemical Engineering Journal, Volume 523, 2025, 168118, ISSN 1385-8947, doi: https://doi.org/10.1016/j.cej.2025.168118.

[28] Yuzheng Shao, Bin Luo, Tao Liu, Chenchen Cai, Xiangjiang Meng, Shuangfei Wang, Shuangxi Nie, Harvesting energy from extreme environmental conditions with cellulosic triboelectric materials, Materials Today, Volume 66, 2023, P 348-370, ISSN 1369-7021, doi: https://doi.org/10.1016/j.mattod.2023.04.006.

[29] Guanbo Min, Yang Xu, Peter Cochran, Nikolaj Gadegaard, Daniel M. Mulvihill, Ravinder Dahiya, Origin of the contact force-dependent response of triboelectric nanogenerators, Nano Energy, Volume 83, 2021, 105829, ISSN 2211-2855, doi: https://doi.org/10.1016/j.nanoen.2021.105829.

[30] S. Gong, K. Li, S. Zhao, S. Gong, H. Guo, Q. Li, J. Chen, Alternating Electrical Polarity Enabled Efficient Charge Capture Triboelectric Nanogenerator for Self-Powered Environmental Purification and Monitoring System. Adv. Funct. Mater. 2025, e11489. doi: https://doi.org/10.1002/adfm.202511489

[31] Sung-Ho Shin, Young Eun Bae, Hyun Kyung Moon, Jungkil Kim, Suk-Ho Choi, Yongho Kim, Hyo Jae Yoon, Min Hyung Lee, and Junghyo Nah Formation of Triboelectric Series via Atomic-Level Surface Functionalization for Triboelectric Energy Harvesting ACS Nano 2017 11 (6), 6131-6138 doi: https://doi.org/10.1021/acsnano.7b02156

[32] Changjun Yang, Yamei Wang, Yan Wang, Zehui Zhao, Liwen Zhang, Huawei Chen,

[33] Highly stretchable PTFE particle enhanced triboelectric nanogenerator for droplet energy harvestings, Nano Energy, Volume 118, Part A, 2023, 109000, ISSN 2211-2855, https://doi.org/10.1016/j.nanoen.2023.109000.

[34] I.V. Vasenina, K.P. Savkin, O.A. Laput, D.N. Lytkina, V.V. Botvin, A.V. Medovnik, I.A. Kurzina, Effects of ion- and electron-beam treatment on surface physicochemical

properties of polytetrafluoroethylene, Surface and Coatings Technology, Volume 334, 2018, Pages 134-141, ISSN 0257-8972, https://doi.org/10.1016/j.surfcoat.2017.11.035.

[35] Nuanyang Cui, Long Gu, Yimin Lei, Jinmei Liu, Yong Qin, Xiaohua Ma, Yue Hao, and Zhong Lin Wang, Dynamic Behavior of the Triboelectric Charges and Structural Optimization of the Friction Layer for a Triboelectric Nanogenerator ACS Nano 2016 10 (6), 6131-6138 doi: https://doi.org/10.1021/acsnano.6b02076

[36] Vu Nguyen, Rusen Yang, Effect of humidity and pressure on the triboelectric nanogenerator, Nano Energy, Volume 2, Issue 5, 2013, Pages 604-608, ISSN 2211-2855, https://doi.org/10.1016/j.nanoen.2013.07.012.

[37] Yuanjie Su, Guangzhong Xie, Si Wang, Huiling Tai, Qiuping Zhang, Hongfei Du, Hulin Zhang, Xiaosong Du, Yadong Jiang, Novel high-performance self-powered humidity detection enabled by triboelectric effect, Sensors and Actuators B: Chemical, Volume 251, 2017, P 144-152, ISSN 0925-4005, https://doi.org/10.1016/j.snb.2017.04.039.

[38] Kun Wang, Zhirong Qiu, Jiaxin Wang, Ye Liu, Rong Chen, Haoqun An, Jae Hyeon Park, Chan Hee Suk, Chaoxing Wu, Jintang Lin, Tae Whan Kim, Effect of relative humidity on the enhancement of the triboelectrification efficiency utilizing water bridges between triboelectric materials, Nano Energy, Volume 93, 2022, 106880, ISSN 2211-2855, https://doi.org/10.1016/j.nanoen.2021.106880.

[39] He Zhang, Liwei Quan, Jinkai Chen, Chengkan Xu, Chenhui Zhang, Shurong Dong, Chaofeng Lü, Jikui Luo, A general optimization approach for contact-separation triboelectric nanogenerator, Nano Energy, Volume 56, 2019, Pages 700-707, ISSN 2211-2855, https://doi.org/10.1016/j.nanoen.2018.11.062.

[40] Xuan Zhang, Linfeng Chen, Yan Jiang, Weichun Lim, and Siowling Soh Rationalizing the Triboelectric Series of Polymers Chemistry of Materials 2019 31 (5), 1473-1478 doi: https://doi.org/10.1021/acs.chemmater.8b04526

[41] A.F. Diaz, R.M. Felix-Navarro, A semi-quantitative tribo-electric series for polymeric materials: the influence of chemical structure and properties, Journal of Electrostatics, Volume 62, Issue 4, 2004, Pages 277-290, ISSN 0304-3886, doi: https://doi.org/10.1016/j.elstat.2004.05.005.

[42] Sun-Woo Kim, Ji Young Park, Do-Heon Kim, Hyun-Cheol Song, Hyesung Park, Jeong Min Baik, Enhanced output voltage of thermoelectric generators driven by alternate triboelectric charges, Materials Today Energy, Volume 37, 2023, 101394, ISSN 2468-6069, https://doi.org/10.1016/j.mtener.2023.101394.

[43] Kleyman, Gleb, Kang, Tong, Twiefel, Jens and Voit, Walter. "Characterization of Triboelectric Charge Generation between PTFE and Nylon after Repeated Contacts" Energy Harvesting and Systems, vol. 4, no. 4, 2017, pp. 165-176. https://doi.org/10.1515/ehs-2018-0001

[44] Weixiang Sun, Ning Luo, Yubo Liu, Hao Li, and Daoai Wang, A New Self-Healing Triboelectric Nanogenerator Based on Polyurethane Coating and Its Application for Self-Powered Cathodic Protection, ACS Applied Materials & Interfaces 2022 14 (8), 10498-10507, doi: https://doi.org/10.1021/acsami.2c00881

[45] M. Seol, S. Kim, Y. Cho, K.-E. Byun, H. Kim, J. Kim, S. K. Kim, S.-W. Kim, H.-J. Shin, S. Park, Triboelectric Series of 2D Layered Materials, Adv. Mater. 2018, 30, 1801210. https://doi.org/10.1002/adma.201801210

[46] Choi YS, Kar-Narayan S. Nylon-11 nanowires for triboelectric energy harvesting. EcoMat. 2020, doi: https://doi.org/10.1002/eom2.12063

[47] Shin, Eui-Cheol and Ko, Jae-Hyeon and Lyeo, Ho-Ki and Kim, Yong-Hyun, Derivation of a governing rule in triboelectric charging and series from thermoelectricity, Phys. Rev. Res, 2022, 023131, doi: https://doi.org/10.1103/PhysRevResearch.4.023131

[48] G. Khandelwal, N. P. Maria JosephRaj, S.-J. Kim 2101170, Materials Beyond Conventional Triboelectric Series for Fabrication and Applications of Triboelectric Nanogenerators. Adv. Energy Mater. 2021, 11, 2101170. https://doi.org/10.1002/aenm.202101170

[49] D. G. Dassanayaka, T. M. Alves, N. D. Wanasekara, I. G. Dharmasena, J. Ventura, Recent Progresses in Wearable Triboelectric Nanogenerators. Adv. Funct. Mater. 2022, 32, 2205438. https://doi.org/10.1002/adfm.202205438

[50] Z. Liu, H. Li, B. Shi, Y. Fan, Z. L. Wang, Z. Li, Wearable and Implantable Triboelectric Nanogenerators Adv. Funct. Mater. 2019, 29, 1808820. https://doi.org/10.1002/adfm.201808820

[51] Zhihao Zhou, Xiaoshi Li, Yufen Wu, Heng Zhang, Zhiwei Lin, Keyu Meng, Zhiming Lin, Qiang He, ChenChen Sun, Jin Yang, Zhong Lin Wang, Wireless self-powered sensor networks driven by triboelectric nanogenerator for in-situ real time survey of environmental monitoring, Nano Energy, Volume 53, 2018, Pages 501-507, ISSN 2211-2855, https://doi.org/10.1016/j.nanoen.2018.08.055.

[52] Wang, J.; Ding, W.; Pan, L.; Wu, C.; Yu, H.; Yang, L.; Liao, R.; Wang, Z.L. Self-powered wind sensor system for detecting wind speed and direction based on a triboelectric nanogenerator. ACS Nano 2018, 12, 3954–3963

[53] D. Zhang, L. Zhou, Y. Wu, C. Yang, H. Zhang, Triboelectric Nanogenerator for Self-Powered Gas Sensing. Small 2024, 20, 2406964. https://doi.org/10.1002/smll.202406964

[54] Renyun Zhang, Magnus Hummelgård, Jonas Örtegren, Martin Olsen, Henrik Andersson, Ya Yang, Håkan Olin, Zhong Lin Wang, Utilising the triboelectricity of the human body for human-computer interactions, Nano Energy, Volume 100, 2022, 107503, ISSN 2211-2855, https://doi.org/10.1016/j.nanoen.2022.107503.

[55] W. Ding, A. C. Wang, C. Wu, H. Guo, Z. L. Wang, Human–Machine Interfacing Enabled by Triboelectric Nanogenerators and Tribotronics, Adv. Mater. Technol. 2019, 4, 1800487. https://doi.org/10.1002/admt.201800487

[56] Khan U, Kim TH, Ryu H, Seung W, Kim SW. Graphene Tribotronics for Electronic Skin and Touch Screen Applications. Adv Mater. 2017 Jan;29(1). doi: 10.1002/adma.201603544. Epub 2016 Oct 27. PMID: 27786382.

[57] Zou, H., Zhang, Y., Guo, L. et al. Quantifying the triboelectric series. Nat Commun 10, 1427 (2019). https://doi.org/10.1038/s41467-019-09461-x

[58] Khan, Farid Ullah, Ahmad, Iftikhar, Review of Energy Harvesters Utilizing Bridge Vibrations, Shock and Vibration, 2016, 1340402, 21 pages, 2016. https://doi.org/10.1155/2016/1340402

[59] Xiong Pu, Chi Zhang, Zhong Lin Wang, Triboelectric nanogenerators as wearable power sources and self-powered sensors, National Science Review, Volume 10, Issue 1, January 2023, nwac170, https://doi.org/10.1093/nsr/nwac170

[60] Feng-Ru Fan, Zhong-Qun Tian, Zhong Lin Wang, Flexible triboelectric generator, Nano Energy, Volume 1, Issue 2, 2012, Pages 328-334, ISSN 2211-2855 https://doi.org/10.1016/j.nanoen.2012.01.004.

[61] Hongmei Yang, Haoyu Huang, Feng Guo, Xiao Tang, Xianju Zhou, Yi Xi, Advancing wearable triboelectric nanogenerators: enhancing stability and reliability, Nano Energy, Volume 135, 2025, 110623, ISSN 2211-2855, https://doi.org/10.1016/j.nanoen.2024.110623.

[62] Rui Li, Zhenyu Xu, Long Li, Junjie Wei, Wenqin Wang, Zejun Yan, Tao Chen, Breakage-resistant hydrogel electrode enables ultrahigh mechanical reliability for triboelectric nanogenerators, Chemical Engineering Journal, Volume 454, Part 3, 2023, 140261, ISSN 1385-8947, https://doi.org/10.1016/j.cej.2022.140261.

[63] C. Wu, A. C. Wang, W. Ding, H. Guo, Z. L. Wang, Triboelectric Nanogenerator: A Foundation of the Energy for the New Era Adv. Energy Mater. 2019, 9, 1802906. https://doi.org/10.1002/aenm.201802906

[64] Wang, Y., Yang, Y. & Wang, Z.L. Triboelectric nanogenerators as flexible power sources. npj Flex Electron 1, 10 (2017). https://doi.org/10.1038/s41528-017-0007-8

[65] Te-Chien Hou, Ya Yang, Hulin Zhang, Jun Chen, Lih-Juann Chen, Zhong Lin Wang, Triboelectric nanogenerator built inside shoe insole for harvesting walking energy, Nano Energy, Volume 2, Issue 5, 2013, Pages 856-862, ISSN 2211-2855, https://doi.org/10.1016/j.nanoen.2013.03.001.

[66] Tang, Y., Fu, H. & Xu, B. Advanced design of triboelectric nanogenerators for future eco-smart cities. Adv Compos Hybrid Mater 7, 102 (2024). https://doi.org/10.1007/s42114-024-00909-3

[67] Yifan Chen, Hongjie Tang, Daning Hao, Tingsheng Zhang, Xiaofeng Xia, Mingyu Wang, Zutao Zhang, Peigang Li,A self-powered triboelectric nanosensor based on track vibration energy harvesting for smart railway, Sustainable Energy Technologies and Assessments, Volume 75, 2025, 104203, ISSN 2213-1388, https://doi.org/10.1016/j.seta.2025.104203.

[68] Vikas Narayan Thakur, Jeong In Han, Triboelectric nanogenerator for smart traffic monitoring and safety, Journal of Industrial and Engineering Chemistry, Volume 124, 2023, Pages 89-101, ISSN 1226-086X, https://doi.org/10.1016/j.jiec.2023.04.028.

[69] Jingui Qian, Dong-Su Kim, Dong-Weon Lee, On-vehicle triboelectric nanogenerator enabled self-powered sensor for tire pressure monitoring, Nano Energy, Volume 49, 2018, Pages 126-136, ISSN 2211-2855, https://doi.org/10.1016/j.nanoen.2018.04.022.

[70] Yanqiang Hu, Xiaoli Wang, Yechen Qin, Zhihao Li, Chenfei Wang, Heng Wu, A robust hybrid generator for harvesting vehicle suspension vibration energy from random road excitation, Applied Energy, Volume 309, 2022, 118506, ISSN 0306-2619, https://doi.org/10.1016/j.apenergy.2021.118506.

[71] Zhang, He, Yao, Linjie, Quan, Liwei and Zheng, Xianglong. "Theories for triboelectric nanogenerators: A comprehensive review" Nanotechnology Reviews, vol. 9, no. 1, 2020, pp. 610-625. https://doi.org/10.1515/ntrev-2020-0049

[72] Lin, Zhiming, Chen, Jun, Yang, Jin, Recent Progress in Triboelectric Nanogenerators as a Renewable and Sustainable Power Source, Journal of Nanomaterials, 2016, 5651613, 24 pages, 2016. https://doi.org/10.1155/2016/5651613

[73] J. Zhao, Y. Shi, Boosting the Durability of Triboelectric Nanogenerators: A Critical Review and Prospect. Adv. Funct. Mater. 2023, 33, 2213407. https://doi.org/10.1002/adfm.202213407

[74] Zhang, X., Liu, M., Zhang, Z., Min, H., Wang, C., Hu, G., Yang, T., Luo, S., Yu, B., Huang, T., Zhu, M. and Yu, H. (2023), Highly Durable Bidirectional Rotary Triboelectric Nanogenerator with a Self-Lubricating Texture and Self-Adapting Contact Synergy for Wearable Applications. Small, 19: 2300890. https://doi.org/10.1002/smll.202300890

[75] L. Zhou, D. Liu, Z. Zhao, S. Li, Y. Liu, L. Liu, Y. Gao, Z. L. Wang, J. Wang, Simultaneously Enhancing Power Density and Durability of Sliding-Mode Triboelectric Nanogenerator via Interface Liquid Lubrication. Adv. Energy Mater. 2020, 10, 2002920. https://doi.org/10.1002/aenm.202002920

[76] S.-H. Chung, J. Chung, M. Song, S. Kim, D. Shin, Z.-H. Lin, B. Koo, D. Kim, J. Hong, S. Lee, Nonpolar Liquid Lubricant Submerged Triboelectric Nanogenerator for Current Amplification via Direct Electron Flow. Adv. Energy Mater. 2021, 11, 2100936. https://doi.org/10.1002/aenm.202100936

[77] Jiang, T., Chen, X., Yang, K. et al. Theoretical study on rotary-sliding disk triboelectric nanogenerators in contact and non-contact modes. Nano Res. 9, 1057–1070 (2016). https://doi.org/10.1007/s12274-016-0997-x

[78] M. Wang, N. Zhang, Y. Tang, Single-electrode triboelectric nanogenerators based on sponge-like porous PTFE thin films for mechanical energy harvesting and self-powered electronics, Journal of Materials Chemistry, 2017, 2050-7488, https://doi.org/10.1039/C7TA02680C

[79] Niu, S., Liu, Y., Wang, S., Lin, L., Zhou, Y.S., Hu, Y. and Wang, Z.L. (2014), Theoretical Investigation and Structural Optimization of Single-Electrode Triboelectric Nanogenerators. Adv. Funct. Mater., 24: 3332-3340. https://doi.org/10.1002/adfm.201303799

[80] Wasim Akram, Qian Chen, Guangbo Xia, Jian Fang, A review of single electrode triboelectric nanogenerators, Nano Energy, Volume 106, 2023, 108043, ISSN 2211-2855, https://doi.org/10.1016/j.nanoen.2022.108043.

[81] Simiao Niu, Ying Liu, Xiangyu Chen, Sihong Wang, Yu Sheng Zhou, Long Lin, Yannan Xie, Zhong Lin Wang, Theory of freestanding triboelectric-layer-based nanogenerators, Nano Energy, Volume 12, 2015, Pages 760-774, ISSN 2211-2855, https://doi.org/10.1016/j.nanoen.2015.01.013.

[82] Wang, S., Xie, Y., Niu, S., Lin, L. and Wang, Z.L. (2014), Freestanding Triboelectric-Layer-Based Nanogenerators for Harvesting Energy from a Moving Object or Human Motion in Contact and Non-contact Modes. Adv. Mater., 26: 2818-2824. https://doi.org/10.1002/adma.201305303

[83] Sihong Wang, Simiao Niu, Jin Yang, Long Lin, and Zhong Lin Wang, Quantitative Measurements of Vibration Amplitude Using a Contact-Mode Freestanding Triboelectric Nanogenerator, ACS Nano 2014 8 (12), 12004-12013 doi: https://doi.org/10.1021/nn5054365

[84] D. Godwinraj, Soney C. George, Recent advancement in TENG polymer structures and energy efficient charge control circuits, Advanced Industrial and Engineering Polymer Research, Volume 4, Issue 1, 2021, Pages 1-8, ISSN 2542-5048, https://doi.org/10.1016/j.aiepr.2020.12.003.

[85] Huijuan Guo, Xueting Jia, Lue Liu, Xia Cao, Ning Wang, and Zhong Lin Wang, Freestanding Triboelectric Nanogenerator Enables Noncontact Motion-Tracking and Positioning, ACS Nano 2018 12 (4), 3461-3467 doi: https://doi.org/10.1021/acsnano.8b00140

[86] Zhang R, Olin H. Material choices for triboelectric nanogenerators: A critical review. EcoMat. 2020; 2:e12062. https://doi.org/10.1002/eom2.12062

[87] Zhao, Z., Zhou, L., Li, S. et al. Selection rules of triboelectric materials for direct-current triboelectric nanogenerator. Nat Commun 12, 4686 (2021). https://doi.org/10.1038/s41467-021-25046-z

[88] Bhaskar Dudem, Dong Hyun Kim, Anki Reddy Mule, and Jae Su Yu Enhanced Performance of Microarchitectured PTFE-Based Triboelectric Nanogenerator via Simple Thermal Imprinting Lithography for Self-Powered Electronics ACS Applied Materials & Interfaces 2018 10 (28), 24181-24192 https://doi.org/10.1021/acsami.8b06295

[89] G.-Z. Li, G.-G. Wang, D.-M. Ye, X.-W. Zhang, Z.-Q. Lin, H.-L. Zhou, F. Li, B.-L. Wang, J.-C. Han, High-Performance Transparent and Flexible Triboelectric Nanogenerators Based on PDMS-PTFE Composite Films, Adv. Electron. Mater. 2019, 5, 1800846. https://doi.org/10.1002/aelm.201800846

[90] Lee, J.P.; Lee, J.W.; Baik, J.M. The Progress of PVDF as a Functional Material for Triboelectric Nanogenerators and Self-Powered Sensors. Micromachines 2018, 9, 532. https://doi.org/10.3390/mi9100532

[91] Tofel, P.; Částková, K.; Říha, D.; Sobola, D.; Papež, N.; Kaštyl, J.; Ţălu, Ş.; Hadaš, Z. Triboelectric Response of Electrospun Stratified PVDF and PA Structures. Nanomaterials 2022, 12, 349. https://doi.org/10.3390/nano12030349

[92] Ferreira, M.P.S.; Ferreira, I.; Pais, V.; Leite, L.; Bessa, J.; Cunha, F.; Fangueiro, R. Towards Perfluoroalkyl and Polyfluoroalkyl Substance (PFAS)-Free Energy Harvesting: Recent Advances in Triboelectric Nanogenerators for Sports Applications. Micromachines 2025, 16, 313. https://doi.org/10.3390/mi16030313

[93] Ra, Yoonsang, Lee, Jong Hyun, Toward Commercialization of Mechanical Energy Harvester: Reusable Triboelectric Nanogenerator Based on Closed-Loop Mass Production of Recyclable Thermoplastic Fluoropolymer with Microstructures, International Journal of Energy Research, 2023, 6919663, 18 pages, 2023. https://doi.org/10.1155/2023/6919663

[94] Chengmei Jiang, Cui Wu, Xunjia Li, Yao Yao, Lingyi Lan, Fengnian Zhao, Zunzhong Ye, Yibin Ying, Jianfeng Ping, All-electrospun flexible triboelectric nanogenerator based on metallic MXene nanosheets, Nano Energy, Volume 59, 2019, Pages 268-276, ISSN 2211-2855, https://doi.org/10.1016/j.nanoen.2019.02.052.

[95] Tene, T., Gulahmadov, O., Gahramanli, L., Muradov, M., Gilev, J. B., Hamzayeva, T., Bayramova, S., Bellucci, S., & Vacacela Gomez, C. (2025). Influence of MWCNT Concentration on Performance of Nylon/MWCNT Nanocomposite-Based Triboelectric Nanogenerators Fabricated via Spin Coating Method. Nanoenergy Advances, 5(3), 9. https://doi.org/10.3390/nanoenergyadv5030009

[96] Daewon Kim, Seung-Bae Jeon, Ju Young Kim, Myeong-Lok Seol, Sang Ouk Kim, Yang-Kyu Choi, High-performance nanopattern triboelectric generator by block copolymer lithography, Nano Energy, Volume 12, 2015, Pages 331-338, ISSN 2211-2855, https://doi.org/10.1016/j.nanoen.2015.01.008.

[97] Ken C. Pradel, Naoki Fukata, Systematic optimization of triboelectric nanogenerator performance through surface micropatterning, Nano Energy, Volume 83, 2021, 105856, ISSN 2211-2855, https://doi.org/10.1016/j.nanoen.2021.105856.

[98] Prada, T., Harnchana, V., Lakhonchai, A. et al. Enhancement of output power density in a modified polytetrafluoroethylene surface using a sequential O2/Ar plasma etching for triboelectric nanogenerator applications. Nano Res. 15, 272–279 (2022). https://doi.org/10.1007/s12274-021-3470-4

[99] Teng, Y.; Li, J.; Yao, J.; Kang, L.; Li, Q. Filled carbon-nanotube heterostructures: from synthesis to application. Microstructures 2023, 3, 2023019. http://dx.doi.org/10.20517/microstructures.2023.07

[100] Wang, Huan, et al. "High performance triboelectric nanogenerators with aligned carbon nanotubes." Nanoscale 8.43 (2016): 18489-18494. http://dx.doi.org/10.1039/C6NR06319E

[101] Sungjun Cho, Yoseop Shin, Janghoon Choi, Jonghyun Eom, Byung Soo Oh, Jeongsoo Lee, Gun Young Jung, Triboelectric nanogenerator based on intercalated Al layer within fluttering dielectric film, Nano Energy, Volume 77, 2020, 105184, ISSN 2211-2855, https://doi.org/10.1016/j.nanoen.2020.105184.

[102] Yuxing Lin, Honglie Shen, Xiangyu Chen, Yufang Li, Yajun Xu, Binbin Xu, Triboelectric nanogenerator-based anodic bonding of silicon to glass with an intermediate aluminum layer, Sensors and Actuators A: Physical, Volume 331, 2021, 112950, ISSN 0924-4247, https://doi.org/10.1016/j.sna.2021.112950.

[103] Xiaonan Wen, Yuanjie Su, Ya Yang, Hulin Zhang, Zhong Lin Wang, Applicability of triboelectric generator over a wide range of temperature, Nano Energy, Volume 4, 2014, Pages 150-156, ISSN 2211-2855, https://doi.org/10.1016/j.nanoen.2014.01.001.

[104] Zhe Wang, Li Cheng, Youbin Zheng, Yong Qin, Zhong Lin Wang, Enhancing the performance of triboelectric nanogenerator through prior-charge injection and its application on self-powered anticorrosion, Nano Energy, Volume 10, 2014, Pages 37-43, ISSN 2211-2855, https://doi.org/10.1016/j.nanoen.2014.08.017.

[105] Sihong Wang, Long Lin, Yannan Xie, Qingshen Jing, Simiao Niu, and Zhong Lin Wang, Sliding-Triboelectric Nanogenerators Based on In-Plane Charge-Separation Mechanism Nano Letters 2013 13 (5), 2226-2233 https://doi.org/10.1021/nl400738p

[106] J. Qian, J. He, S. Qian, J. Zhang, X. Niu, X. Fan, C. Wang, X. Hou, J. Mu, W. Geng, X. Chou, A Nonmetallic Stretchable Nylon-Modified High Performance Triboelectric Nanogenerator for Energy Harvesting. Adv. Funct. Mater. 2020, 30, 1907414. https://doi.org/10.1002/adfm.201907414

[107] Satyaranjan Bairagi, Gaurav Khandelwal, Xenofon Karagiorgis, Shravan Gokhool, Charchit Kumar, Guanbo Min, and Daniel M. Mulvihill High-Performance Triboelectric Nanogenerators Based on Commercial Textiles: Electrospun Nylon 66 Nanofibers on Silk

and PVDF on Polyester ACS Applied Materials & Interfaces 2022 14 (39), 44591-44603 https://doi.org/10.1021/acsami.2c13092

[108] Zhi Zhang, Yiyang Xu, Dongfang Wang, Huaguang Yang, Jiansheng Guo, Lih-Sheng Turng, Enhanced performance of an expanded polytetrafluoroethylene-based triboelectric nanogenerator for energy harvesting, Nano Energy, Volume 60, 2019, Pages 903-911 ISSN 2211-2855, https://doi.org/10.1016/j.nanoen.2019.04.034.

[109] C. A. Bernard, H. Takana, O. Lame, K. Ogawa, and J. Y. Cavaillé, "Influence of the Nozzle Inner Geometry on the Particle History During Cold Spray Process," J. Therm. Spray Technol., 2022, doi: 10.1007/s11666-022-01407-y.

[110] Ang, A.S.M., Sanpo, N., Sesso, M.L. et al. Thermal Spray Maps: Material Genomics of Processing Technologies. J Therm Spray Tech 22, 1170–1183 (2013). https://doi.org/10.1007/s11666-013-9970-3

[111] Kwok, C. T. & Wong, P.K.. (2010). Laser Surface Alloying of Various Engineering Alloys for Sliding Wear and Corrosion Resistance. Journal of Laser Micro / Nanoengineering. 5. 96. 10.2961/jlmn.2010.01.0019.

[112] Blackmore, C. E. (1987). Nylon Powders and their Application as Surface Coatings Using Flame Spraying. Surface Engineering, 3(1), 29–34. https://doi.org/10.1179/sur.1987.3.1.29

[113] Saed Safai, Herbert Herman, Microstructural investigation of plasma-sprayed aluminum coatings, Thin Solid Films, Volume 45, Issue 2, 1977, Pages 295-307, ISSN 0040-6090, https://doi.org/10.1016/0040-6090(77)90263-2.

[114] M. Wang, Composite coatings for implants and tissue engineering scaffolds. Woodhead Publishing Limited, 2004.

[115] Emerson, "PTFE and PFA Similarities and Differences,"

[116] Hall, A.C., Cook, D.J., Neiser, R.A. et al. The effect of a simple annealing heat treatment on the mechanical properties of cold-sprayed aluminum. J Therm Spray Tech 15, 233–238 (2006). https://doi.org/10.1361/105996306X108138

[117] Ibnaj Anamika Anni, Madison Kaminskyj, Kazi Zahir Uddin, Tristan W. Bacha, Nand K. Singh, Joseph F. Stanzione III, Francis M. Haas, and Behrad Koohbor, Cold Spray Deposition of Nylon-6 on Glass Fiber-Reinforced Composites ACS Applied Engineering Materials 2023 1 (8), 2324-2335 https://doi.org/10.1021/acsaenm.3c00367

[118] Leclerc, Z., McMunn, L.E., Nastic, A. et al. Manufacturing and Icephobic Performance Evaluation of Cold-Sprayed Adhesive Perfluoroalkoxy Alkane Coatings. J Therm Spray Tech 32, 851–876 (2023). https://doi.org/10.1007/s11666-023-01551-z

[119] Fei Xing, Yang Jie, Xia Cao, Tao Li, Ning Wang, Natural triboelectric nanogenerator based on soles for harvesting low-frequency walking energy, Nano Energy, Volume 42, 2017, Pages 138-142, ISSN 2211-2855, https://doi.org/10.1016/j.nanoen.2017.10.029.

[120] Te-Chien Hou, Ya Yang, Hulin Zhang, Jun Chen, Lih-Juann Chen, Zhong Lin Wang, Triboelectric nanogenerator built inside shoe insole for harvesting walking energy, Nano Energy, Volume 2, Issue 5, 2013, Pages 856-862, ISSN 2211-2855, https://doi.org/10.1016/j.nanoen.2013.03.001.

[121] Yuxiang Wu, Yusheng Li, Yang Zou, Wei Rao, Yansong Gai, Jiangtao Xue, Li Wu, Xuecheng Qu, Ying Liu, Guodong Xu, Lingling Xu, Zhuo Liu, Zhou Li, A multi-mode triboelectric nanogenerator for energy harvesting and biomedical monitoring, Nano Energy, Volume 92, 2022, 106715, ISSN 2211-2855, https://doi.org/10.1016/j.nanoen.2021.106715.

[122] Wenkai Xu, Jiangtao Guo, Haiyang Wen, Xianghe Meng, Hongxin Hong, Jingbo Yuan, Jiaan Gao, Dingyu Liu, Qing Ran, Yudi Wang, Jialong Duan, Qunwei Tang, Xiya Yang, Laminated triboelectric acoustic energy harvester based on electrospun nanofiber towards real-time noise decibel monitoring, Nano Energy, Volume 99, 2022, 107348, ISSN 2211-2855, https://doi.org/10.1016/j.nanoen.2022.107348.

[123] Li, Y., Liu, C., Hu, S. et al. Self-Powered Acoustic Sensor Based on Triboelectric Nanogenerator for Smart Monitoring. Acoust Aust 50, 383–391 (2022). https://doi.org/10.1007/s40857-022-00275-4

[124] Zhang He, Su Xinjie, Quan Liwei, Wei Gang Sponge-Supported Triboelectric Nanogenerator for Energy Harvesting from Rail Vibration American Society of Civil Engineers https://doi.org/10.1061/(ASCE)EY.1943-7897.0000751

[125] L. Jin, S. L. Zhang, S. Xu, H. Guo, W. Yang, Z. L. Wang, Free-Fixed Rotational Triboelectric Nanogenerator for Self-Powered Real-Time Wheel Monitoring. Adv. Mater. Technol. 2021, 6, 2000918. https://doi.org/10.1002/admt.202000918

[126] Begum, Shaik Ruksana, and Arunkumar Chandrasekhar. "Biomimicking hydrophobic leaf structure using soft lithography for fog harvesting, triboelectric nanogenerators as a self-powered rain sensor." *Iscience* 27.2 (2024).

[127] Daewon Kim, Seung-Bae Jeon, Ju Young Kim, Myeong-Lok Seol, Sang Ouk Kim, Yang-Kyu Choi, High-performance nanopattern triboelectric generator by block copolymer lithography, Nano Energy, Volume 12, 2015, 331-338, https://doi.org/10.1016/j.nanoen.2015.01.008.

[128] Lee JY, Sung TH, Yeo JS. Cost Effective Fabrication of a Triboelectric Energy Harvester Using Soft Lithography. Applied Science and Convergence Technology 2013;22:198-203.

[129] Cao, R., Wang, J., Zhao, S. et al. Self-powered nanofiber-based screen-print triboelectric sensors for respiratory monitoring. Nano Res. 11, 3771–3779 (2018). https://doi.org/10.1007/s12274-017-1951-2

[130] H C Wan, Y Q Cao, L W Lo, Z H Xu, N Sepúlveda, and C Wang, Screen-printed soft triboelectric nanogenerator with porous PDMS and stretchable PEDOT:PSS

electrode[J]. J. Semicond., 2019, 40(7), 000000. http://doi.org/10.1088/1674-4926/40/6/000000

[131] Zhang, Chi, et al. “Customizing Triboelectric Nanogenerator on Everyday Clothes by Screen-Printing Technology for Biomechanical Energy Harvesting and Human-Interactive Applications.” Advanced Materials Technologies, vol. 8, no. 4, February 2023, https://doi.org/10.1002/admt.202201138.

[132] Gao, Yuanyuan, et al. “Scalable Core–Spun Coating Yarn-Based Triboelectric Nanogenerators with Hierarchical Structure for Wearable Energy Harvesting and Sensing via Continuous Manufacturing.” Nano Energy, vol. 91, no. 106672, January 2022, https://doi.org/10.1016/j.nanoen.2021.106672.

[133] Tene, T.; Gulahmadov, O.; Gahramanli, L.; Muradov, M.; Gilev, J.B.; Hamzayeva, T.; Bayramova, S.; Bellucci, S.; Vacacela Gomez, C. Influence of MWCNT Concentration on Performance of Nylon/MWCNT Nanocomposite-Based Triboelectric Nanogenerators Fabricated via Spin Coating Method. Nanoenergy Adv. 2025, 5, 9. https://doi.org/10.3390/nanoenergyadv5030009

[134] Laurell Technologies**.** "Spin Coating Process Diagram." *Spincoater.com*, spincoater.com.

[135] Sulen, W. L., Ravi, K., Bernard, C., Mary, N., Ichikawa, Y., & Ogawa, K. (2019). Effects of Nano-Ceramic Particle Addition for Cold Sprayed Fluoropolymer Coatings. Key EngineeringMaterials,813,141–146.
https://doi.org/10.4028/www.scientific.net/kem.813.141

[136] Anni, Ibnaj Anamika, et al. “Cold Spray Deposition of Nylon-6 on Glass Fiber-Reinforced Composites.” *ACS Applied Engineering Materials*, vol. 1, no. 8, August 2023, pp. 2324–35, https://doi.org/10.1021/acsaenm.3c00367.

[137] Yao Chu, Ruixing Han, Fanyu Meng, Zeyuan Cao, Shiwen Wang, Kangkang Dong, Shuangshuang Yang, Huiliang Liu, Xiongying Ye, Fei Tang, Theoretical study on the output of contact-separation triboelectric nanogenerators with arbitrary charging and grounding conditions, Nano Energy, Volume 89, Part A, 2021, 106383, ISSN 2211-2855, https://doi.org/10.1016/j.nanoen.2021.106383.

[138] Yao Chu, Ruixing Han, Fanyu Meng, Zeyuan Cao, Shiwen Wang, Kangkang Dong, Shuangshuang Yang, Huiliang Liu, Xiongying Ye, Fei Tang, Theoretical study on the output of contact-separation triboelectric nanogenerators with arbitrary charging and grounding conditions, Nano Energy, Volume 89, Part A, 2021, 106383, ISSN 2211-2855, https://doi.org/10.1016/j.nanoen.2021.106383.

[139] Zi, Y., Niu, S., Wang, J. et al. Standards and figure-of-merits for quantifying the performance of triboelectric nanogenerators. Nat Commun 6, 8376 (2015). https://doi.org/10.1038/ncomms9376

[140] Shao, Jiajia, Morten Willatzen, and Zhong Lin Wang. "Theoretical modeling of triboelectric nanogenerators (TENGs)." Journal of Applied Physics 128.11 2020 https://doi.org/10.1063/5.0020961

Appendix – A

For the case of two conducting plates with opposite charge and a dielectric separating the two, an electric field E_0 is generated on the positively charged plate. This can be described using Gauss' law. Figure 98 shows the oppositely charged plates and generated electric field E_0.

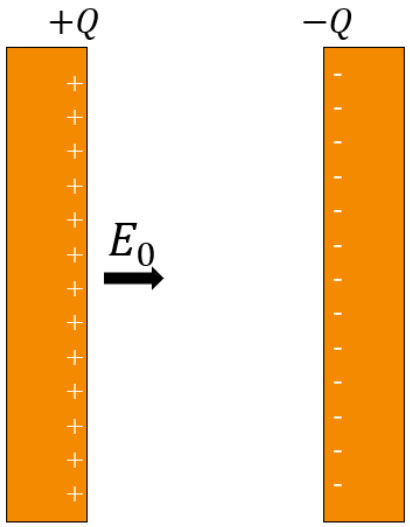

Figure 98: Two oppositely charged plates in between a dielectric

$$\oint E_0 \cdot dA = \frac{Q}{\varepsilon_0}$$

Assuming a Gaussian surface, such that E_0 is constant everywhere, and assuming the area element is a flat square surface means that the above equation simplifies to,

$$E_0 = \frac{Q}{A\varepsilon_0} \tag{1}$$

Because of the electric field E_0, a resultant electric field E will appear on the dielectric, opposing the direction of the external electric field E_0, and inducing charges $-Q_i$ and $+Q_i$, as shown in Figure 99.

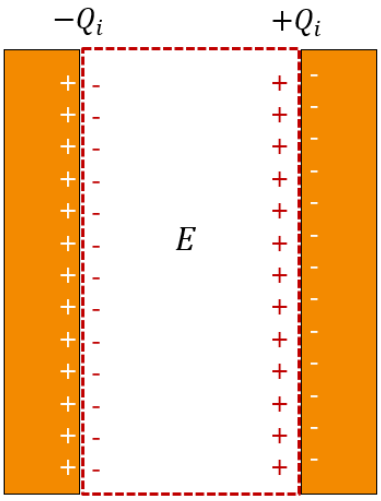

Figure 99: Induced electric field on dielectric

If E is the resultant electric field, the net charge on the interface of the conducting plate and dielectric will be the difference of the charges $Q - Q_i$, seen in Figure 100.

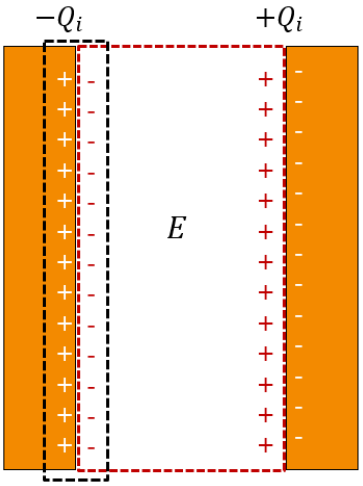

Figure 100: Surface of interest

Rearranging Gauss' law for the resultant electric field E means Equation 1 becomes,

$$E = \frac{Q - Q_i}{A\varepsilon_0} \tag{2}$$

The dielectric constant of a material is defined as the ratio of the charge stored in an insulating material placed between two metallic plates to the charge that can be stored when the insulating material is replaced by vacuum or air. It is known as relative permittivity and is mathematically defined as the ratio of the electric field of the dielectric and the electric field of the conductor.

$$\varepsilon_r \equiv \frac{E_0}{E} \tag{3}$$

Substituting equation 3 into equation 2,

$$\frac{E_0}{\varepsilon_r} = \frac{Q - Q_i}{A\varepsilon_0} = \frac{Q}{A\varepsilon_0} - \frac{Q_i}{A\varepsilon_0}$$

$$\frac{Q}{\varepsilon_r} = Q - Q_i$$

This simplifies to,

$$Q_i = Q\left(1 - \frac{1}{\varepsilon_r}\right) \tag{4}$$

Now that there is a relationship between Q_i and Q, equation 4 be substituted into the expression for E.

$$EA = \frac{Q}{\varepsilon_0} - \frac{Q}{\varepsilon_0}\left(1 - \frac{1}{\varepsilon_r}\right)$$

$$EA = \frac{Q}{\varepsilon_0} - \frac{Q}{\varepsilon_0} + \frac{Q}{\varepsilon_0\varepsilon_r}$$

Isolating for the resultant electric field E gives,

$$E = \frac{Q}{A\varepsilon_0\varepsilon_r} \tag{5}$$

Which is the final equation for an electric field of a dielectric.